



## INVESTIGATION OF THE USE OF ADSORPTION, CERAMIC MEMBRANE, HYBRID SYSTEMS IN Cr(VI) REMOVAL

Neşe Öztürk<sup>a</sup>, İlknur Tatar<sup>b</sup>, Huriye Batmaz<sup>c</sup>, Dilhe Nur Çim<sup>d</sup>, Kevser Günduğar<sup>e</sup>, Melis Bakkalçı<sup>f</sup>

<sup>a</sup>Eskisehir Osmangazi University, Faculty of Engineering and Architecture, Chemical Engineering Department, 26480 Eskisehir, Turkey.

<sup>b</sup>İLKSEM Engineering Incorporated Company, 26190, Eskişehir, Turkey.

<sup>c</sup>DRC Rubber Industry and Trade Incorporated Company. Serdivan, 54200, Sakarya,

<sup>d</sup>Trakya University, 22000, Edirne, Turkey.

<sup>e</sup>RAGS alcoholic beverages Industry and Trade Incorporated Company, 39100, Kırklareli,

<sup>f</sup>Deva Holding Company, 59510, Çerkezköy, Tekirdağ, Turkey.

**Abstract:** In this study, Cr(VI) removal from aqueous solutions by adsorption-ceramic membrane hybrid system was investigated. For this aim batch adsorption, batch ceramic membrane and adsorption-ceramic membrane hybrid systems experiments were conducted. *Platanus orientalis* (sycamore fruit) treated with 1 M H<sub>2</sub>SO<sub>4</sub> was used as adsorbent in adsorption experiments. Ceramic membranes produced by İLKSEM Engineering Incorporated Company were used in the experiments. Membranes produced from different materials have different pore sizes. Cr(VI) removal yield was obtained as 90.1% by adsorption (contact time 3 hours)- ceramic membrane hybrid system.

**Keywords:** Cr(VI), adsorption, Platanus Orientalis, ceramic membranes, hybrid system.

**Submitted:** November 09, 2018. **Accepted:** June 01, 2019.

**Cite this:** Öztürk N, Tatar İ, Batmaz H, Çim D, Günduğar K, Bakkalçı M. INVESTIGATION OF THE USE OF ADSORPTION, CERAMIC MEMBRANE, HYBRID SYSTEMS IN Cr(VI) REMOVAL. JOTCSB. 2019;2(2):51-6.

\*Corresponding author. E-mail: [nozturk@ogu.edu.tr](mailto:nozturk@ogu.edu.tr).

### INTRODUCTION

Chromium is at the top of the list of toxic pollutants in the wastewater commonly generated in the industry. The chromium is most commonly seen in chromium(VI) or chromium(III) in aqueous solutions. Chromium(VI) compounds are considered to be 100-1000 times more toxic than chromium(III) compounds (1).

The main methods used to remove chromium(VI) from waters and wastewater; chemical precipitation, ion exchange and adsorption processes. Ceramic membranes are used to remove suspended solids, microorganisms, heavy metals, radioactive materials, pesticides, and pre-treatment water and wastewater treatment prior to reverse osmosis. Ceramic membranes are also preferred in the treatment of wastewater treatment plant drainage water. The term hybrid

membrane processes can be explained as applying one or more membrane processes together with conventional treatment systems to improve feed and product quality (2, 3). The main purpose of these systems is to increase the purification as much as possible.

Cr(VI) removal by adsorption was investigated onto different material such as *Ocimum americanum* L. seed pods, biomass of microalgae *Scenedesmus* sp., chestnut shells by different investigators (1, 4-6).

Ceramic membrane preparation, characterization and performance evaluation studies were conducted at different studies (7-11).

In this study, Cr(VI) removal from aqueous solution by adsorption on to *Platanus orientalis* treated with 1M H<sub>2</sub>SO<sub>4</sub>, ceramic membrane filtration and adsorption - ceramic membrane

filtration hybrid systems were investigated. *Platanus orientalis* was used as adsorbent in the study for the first time. Ceramic membranes produced by İLKSEM Engineering Incorporated Company were used in experiments. The results are presented and discussed.

## EXPERIMENTAL

Cr(VI) solutions were prepared from 1000 mg/L  $K_2Cr_2O_7$  stock solution. Cr(VI) concentrations were determined by diphenyl carbazide method using standard methods with a UV/Vis spectrophotometer (Shimadzu UV-120-01) (12).

### Adsorption experiments

*Platanus orientalis* was used as the adsorbent. It was broken (all of the part was used) and dried at 100 °C for 24 hours and treated by 1M  $H_2SO_4$ . For this aim, 3 g of the adsorbent was mixed with 50 mL of the acid solution at about 80–90 °C for 2 hours on a hotplate/magnetic stirrer and then filtered from filter paper. Adsorbent particles on filter paper were washed with 50 mL of distilled water and then dried at 105 °C in an oven.

In the study, batch adsorption experiments were conducted. Shaker water bath (Memmert) was used for constant temperature for batch adsorption experiments. After adsorption mixture was filtered and Cr(VI) concentration was analyzed in the filtrate, equilibrium concentrations were determined.

To determine the effect of initial concentration, 50 mL solutions at the initial concentrations of 75,

100, 150, 200, 250, and 300 mg/L, were prepared using 1000 mg/L stock  $K_2Cr_2O_7$  solution. For each initial concentration, 25 mL of solution was placed on 0.5 g of *Platanus orientalis*. The mixture was shaken for 24 hours at 25 °C and 140 rpm in a shaker water bath and filtered through filter paper. Cr(VI) was analyzed in filtrates by a UV/Vis spectrophotometer.

In order to determine the effect of contact time on Cr(VI) adsorption, 10 g of acid-treated *Platanus orientalis* was weighed into the beaker and placed into a 500 mL of a 100 mg Cr(VI) / L solution. It was kept on the magnetic stirrer for 24 hours at a stirring rate of 700 rpm. Samples (5 mL) were taken at certain time intervals and Cr(VI) concentrations were analyzed.

### Ceramic Membrane Experiments

Different ceramic membranes coded as K1, K4, and K7, produced by İLKSEM Engineering Incorporated Company, were used in ceramic membrane filtration experiments. Properties of ceramic membranes which effect on chromium(VI) were determined. Strength was tested Gabriella CRS1650, density, water absorption percent were tested by Archimedes scales. Porosity was determined Quantochrome Nova Win 2 BET equipment. According to the membrane codes properties of ceramic membranes were given in Table 1.

Ceramic membrane filtration experimental set up was given in Figure 1.

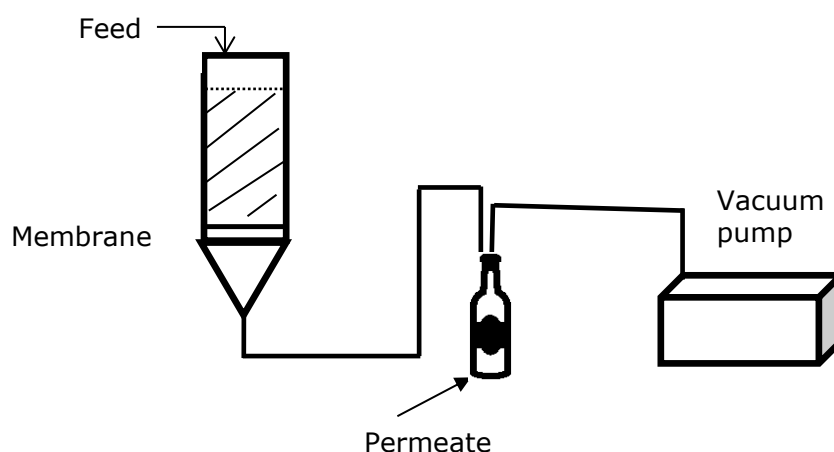


**Figure 1.** Ceramic membrane filtration experimental set-up.

The filtration times for 100 mL solution (100 mg / L Cr(VI)) were determined to calculate permeate fluxes.

**Table 1.** Properties of the ceramic membranes used in experiments (Vacuum pressure: 0.06 MPa, Membrane diameter 5.2 cm, Membrane Thickness: 0.3).

Membrane	Sintering Temperature (°C)	Strength (MPa)	Water absorption (%)	Porosity (%)	Density (g/cm <sup>3</sup> )
K1	1200	6.3	28	44	1.58
K4	1250	3,3	24	40	1.64
K7	1100	7.7	37	46	1.26

**Adsorption – Ceramic Membrane Hybrid System Experiments**

In hybrid system experiments, firstly, batch adsorption experiments were carried out at 25 °C using 0.5 g of the adsorbent and 100 mg/L initial concentration of Cr(VI) solution. Adsorption was terminated at the end of the contact time for 3 hours, and then the filtrate was passed through the ceramic membrane.

**RESULTS AND DISCUSSIONS**

Adsorption continuing until equilibrium is formed between the amount of adsorbed matter (mg / g) and the concentration of the substance remaining in the solution. This equilibrium can be mathematically explained by the adsorption isotherms. The adsorption isotherms define the relationship between solute concentration at the constant temperature and the amount adsorbed by the adsorbent. These values are the values at equilibrium. The equilibrium adsorption isotherm is of fundamental importance in the design of adsorption system. In order to determine adsorption isotherm for Cr(VI) adsorption onto *Platanus orientalis* treated with acid, 25 mL solution at the initial concentrations of 75, 100, 150, 200, 250, 300 mg/L K<sub>2</sub>Cr<sub>2</sub>O<sub>7</sub> solution and 0.5 g of the adsorbent were used in batch adsorption experiment. Cr(VI) removals (%) were calculated from the equation below.

$$Cr(VI) \text{ Removal } (\%) = \frac{C_o - C_e}{C_o} \cdot 100 \quad (\text{Eq. 1})$$

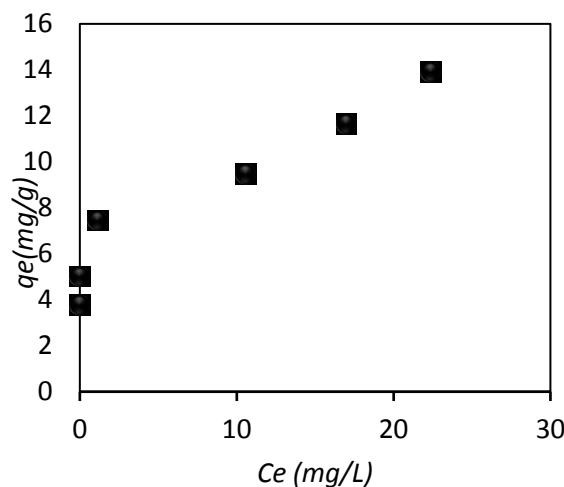


**Figure 2.** Adsorption isotherm for Cr(VI) removal from aqueous solutions onto *Platanus orientalis* treated with 1 M H<sub>2</sub>SO<sub>4</sub>.

$C_e$  = Equilibrium Cr(VI) concentration in solution (mg/L)

$C_o$  = Initial Cr(VI) concentration in solution (mg/L)

Adsorption isotherm is given in Figure 2.

According to the Figure 2 Langmuir and Freundlich isotherms may be applicable to the adsorption data. So in this study, the suitability of the data to Langmuir and Freundlich isotherms was investigated. Linearized form of the the Langmuir isotherm can be expressed as given equation (1).

$$\frac{C_e}{q_e} = \frac{1}{bq_{max}} + \frac{C_e}{q_{max}} \quad (\text{Eq. 2})$$

Where  $q_{max}$  (mg/g) and  $b$  (L/mg) are the Langmuir constants related to the adsorption capacity and energy of adsorption, respectively. The amount of Cr(VI) adsorbed by the *Platanus orientalis*,  $q_e$ (mg/g), calculated given below equation:

$$q_e = (C_o - C_e)V/w \quad (\text{Eq. 3})$$

Where  $V$  : initial volume of Cr(VI) solution (L)  $w$ : weight of the adsorbent (g). In order to find Langmuir isotherm constants  $C_e/q_e$  vs  $C_e$  is plotted. Values of  $q_{max}$  and  $b$  were calculated from the slope and intercept of the linear plots. Calculated isotherm constants were given in Table 2.

Freundlich isotherm is appropriate for the adsorption on to heterogeneous surfaces. This isotherm defines the surface heterogeneity. Freundlich isotherm given in the equation below is based on the assumption that the concentration of adsorbed on the adsorbent surface increases with the increase in the adsorbed concentration (1). According to the Figure 2 it can be said that this assumption is valid.

$$q_e = K_f \cdot C_e^{\frac{1}{n}} \quad (\text{Eq. 4})$$

where  $K_f$  and  $n$  are Freundlich adsorption isotherm constants, affecting the adsorption capacity and intensity of adsorption. Linearized form of Freundlich isotherm is given below:

$$\log q_e = \log K_f + \frac{1}{n} \log C_e \quad (\text{Eq. 5})$$

Values of  $n$  and  $K_f$  were calculated from the slope and intercept of the plots of  $\log q_e$  versus  $\log C_e$ . The calculated isotherm constants are given in Table 2.

**Table 2.** Langmuir and Freundlich models isotherm constants for Cr(VI) adsorption onto *Platanus orientalis* treated with 1 M H<sub>2</sub>SO<sub>4</sub>.

Langmuir Isotherm			Freundlich Isotherm		
b(L/mg)	q <sub>max</sub> (mg/g)	R <sup>2</sup>	n	k <sub>f</sub> (L/g)	R <sup>2</sup>
1.09	13.04	0.965	3.32	5.068	0.822

When the regression coefficients (R<sup>2</sup>) obtained for the isotherms were taken into consideration, Langmuir isotherm was found to be more suitable and the capacity of the adsorbent was determined as 13.04 mg/g. If Freundlich constant  $n$  is greater than unity, this indicates a desired adsorption. Langmuir constant  $q_{max}$ , the adsorption capacity, is maximum amount of Cr(VI) adsorption with complete monolayer coverage on the adsorbent surface. Langmuir constant  $b$  indicates the strength of the link between Cr(VI) ions and the adsorbent.

It was observed that these concentrations were fixed after a certain period of time. This period was determined as the equilibrium time (18 hours) for the used adsorbent. At the beginning, it was seen that removal percent increased rapidly. This situation can be explained by the saturation of the active regions after the equilibrium is reached.

100% removal was obtained for 24 hours contact time, by adsorption at the concentration of 100 mg/L Cr(VI).

BET and SEM analysis were performed for raw and treated *Platanus orientalis*. BET surface areas, pore volumes and pore size distribution were determined by using Quantachrome, Autosorb 1C an automatic adsorption instrument at 77 K. The adsorbate was N<sub>2</sub>. Prior to gas adsorption measurement, the carbon was degassed at 300 °C in the vacuum for 3 h. BET method was applied to calculate the pore volume and surface area. Results for BET analysis were given in Table 3. Surface morphology was investigated by (SEM) (JEOL JSM-5600LV Scanning Electron microscopy). Samples were taken different part of adsorbent and coated Au/Pd. SEM images of *Platanus orientalis* were given in Figure 3.

**Table 3.** BET analysis results

Property	Raw <i>Platanus orientalis</i>	<i>Platanus orientalis</i> treated by acid
SBET(m <sup>2</sup> /g)	10.06	24.35
V <sub>Tot</sub> (cc/g)	0.0194	0.056
Average pore size(A)	60.82	217
V <sub>mic</sub> (cc/g)	0	0

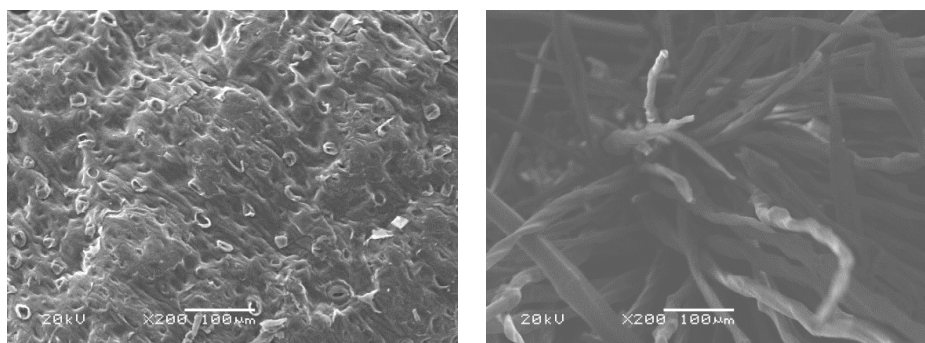


**Figure 3.** Left: SEM image for Raw *Platanus orientalis*. Right: SEM image for *Platanus orientalis* treated by acid.

Pore size increased for acid-treated *Platanus orientalis* (Table 3) compare to the raw sample. Two of the adsorbents did not have micropores. Total pore volume for acid-treated *Platanus orientalis* was greater than the raw sample. Surface area was increased with increasing pore size and total volume of pores. According to the Figure 3a it can be said Raw *Platanus Orientalis* have cellulosic nature. According to the Figure 3b pore size growth was observed for acid treated *Platanus Orientalis*. It can be said that The BET and SEM analysis were found to support each other (Table 3 and Figure 3). This porous structure is thought to contribute to adsorption.

Ceramic Membrane filtration experiment Cr(VI) rejection percent was calculated from below equation:

$$Cr(VI) \text{ rejection } (\%) = \frac{C_f - C_p}{C_f} \times 100 \quad (\text{Eq. 6})$$

where  $C_p$ : Permeate Cr(VI) concentration (mg/L)  
 $C_f$ : Cr(VI) concentration in the feed (mg/L)

Permeate fluxes were calculated from Equation (7).  
 $J = m/A.t$  (Eq. 7)

Where J: Permeate flux ( $\frac{g}{cm^2.s}$ )  
 m: Amount of filtered solution (g)  
 t: Filtration time(s)  
 A: Membrane area ( $cm^2$ ).

For the ceramic membrane filtration experiment, the rejection percent of Cr(VI) and permeate flux values are given in Table 4.

**Table 4.** Results of ceramic membrane experiments

Membrane	Cr(VI) Rejection (%)	Permeate Flux, q ( $\frac{g}{cm^2.s}$ )
K1	6.92	0.0077
K4	16.46	0.0108
K7	3.34	0.0035

A maximum of 16.46% Cr(VI) rejection from a 100 mg / L solution was obtained with K4 coded ceramic membrane. Compared with the properties of the other membranes, it was determined that the membrane used had the highest removal of the membrane with the lowest water absorption capacity and porosity.

In the hybrid system experiments, firstly, batch adsorption experiments were carried out at 25 °C using 0.5 g of adsorbent and 100 mg/L initial concentration of Cr(VI) solution. In the adsorption method, the equilibrium time was 18 hours which was considered to be long for industrial application. So adsorption was terminated at the end of the contact time for 3 hours (removal 76 %), and then the filtrate was passed through the ceramic membrane and 90.1% total removal was achieved.

The purpose of the use of the adsorption ceramic membrane hybrid system as the method is that the concentration of Cr(VI) in wastewaters is lowered to the discharge standards of Turkish Water Pollution Control Act (generally 0.5 mg/L in a 2 hour composite sample). In the hybrid system, the contact time was maintained for 3 hours and 90.1% removal was achieved. So it can be suggested that method is appropriate for this purpose.

## ACKNOWLEDGMENTS

This study was supported as an extension of 2241-A Industry Oriented Undergraduate Thesis Support Program at 2015/3 by TÜBİTAK, Türkiye. The authors express their thanks for financial support to TUBITAK.

## REFERENCES

1. Taşer R. Lead and Chromium (VI) removal from aqueous solutions and metal industry wastewater

[PhD Thesis]. [Eskişehir]: Eskişehir Osmangazi University; 2013.

2. Drioli E, Romano M. Progress and New Perspectives on Integrated Membrane Operations for Sustainable Industrial Growth. *Ind Eng Chem Res.* 2001 Mar;40(5):1277–300.

3. Strathmann H. Membrane separation processes: Current relevance and future opportunities. *AIChE J.* 2001 May;47(5):1077–87.

4. Levankumar L, Muthukumaran V, Gobinath MB. Batch adsorption and kinetics of chromium (VI) removal from aqueous solutions by *Ocimum americanum* L. seed pods. *Journal of Hazardous Materials.* 2009 Jan;161(2–3):709–13.

5. Pradhan D, Sukla LB, Mishra BB, Devi N. Biosorption for removal of hexavalent chromium using microalgae *Scenedesmus* sp. *Journal of Cleaner Production.* 2019 Feb;209:617–29.

6. Niazi L, Lashanizadegan A, Sharififard H. Chestnut oak shells activated carbon: Preparation, characterization and application for Cr (VI) removal from dilute aqueous solutions. *Journal of Cleaner Production.* 2018 Jun;185:554–61.

7. Arzani M, Mahdavi HR, Sheikhi M, Mohammadi T, Bakhtiari O. Ceramic monolith as microfiltration membrane: Preparation, characterization and performance evaluation. *Applied Clay Science.* 2018 Sep;161:456–63.

8. Song X, Jian B, Jin J. Preparation of porous ceramic membrane for gas-solid separation. *Ceramics International.* 2018 Nov;44(16):20361–6.

9. Adam MR, Salleh NM, Othman MHD, Matsuura T, Ali MH, Puteh MH, et al. The adsorptive removal of chromium (VI) in aqueous solution by novel natural zeolite based hollow fibre ceramic membrane. *Journal of Environmental Management*. 2018 Oct;224:252–62.

10. Choudhury P, Mondal P, Majumdar S, Saha S, Sahoo GC. Preparation of ceramic ultrafiltration membrane using green synthesized CuO nanoparticles for chromium (VI) removal and optimization by response surface methodology. *Journal of Cleaner Production*. 2018 Dec;203:511–20.

11. RoyChoudhury P, Majumdar S, Sarkar S, Kundu B, Sahoo GC. Performance investigation of Pb(II) removal by synthesized hydroxyapatite based ceramic ultrafiltration membrane: Bench scale study. *Chemical Engineering Journal*. 2019 Jan;355:510–9.

12. Greenberg AE, Trussell RR, Clesceri LS, American Public Health Association, American Water Works Association, Water Pollution Control Federation, editors. *Standard methods for the examination of water and wastewater*. 16. ed. Washington, D.C: American Public Health Association; 1985. 1268 p.



## MODELLING AND OPTIMISATION OF OIL EXTRACTION FROM LOOFAH (*Luffa cylindrica*) SEEDS USING BINARY SOLVENT MIXTURE

O.A.A ELETTA<sup>1\*</sup> , L.T. ADEWOYE<sup>1</sup> , S. I. MUSTAPHA<sup>1</sup> , A. G. ADENIYI<sup>1</sup> ,  
O.O. OGUNLEYE<sup>2</sup> , O.E. ALADEROKUN<sup>1</sup> , I. A. TIJANI<sup>1</sup> 

<sup>1</sup>Department of Chemical Engineering, University of Ilorin. Ilorin. Nigeria.

<sup>2</sup>Department of Chemical Engineering, Ladoke Akintola University of Technology, Ogbomosho, Nigeria.

**Abstract:** Toxicity and safety concern coupled with the recent increase in its price has necessitated the need for finding alternative solvents to n-hexane. In this study, the effect of binary solvent (ethanol/n-hexane) composition at various extraction temperatures and times on the oil yield was investigated using response surface methodology (RSM). Artificial neural network (ANN) was used as a modelling tool for predicting the oil yield and the performance of both ANN and RSM models was compared. The optimum oil yield (27.67%) was obtained at extraction temperature (40 °C), extraction time (151.9 min) and binary solvent composition (98% ethanol /2% n-hexane). The predicted oil yield values from ANN model was more accurate than that of RSM when compared with experimental values. The fatty acid profile revealed that the refining process promoted saturation of the extracted oil with 67.75% of palmitic acid present in refined loofah seed oil (RLSO). This study demonstrated the feasibility of using a binary mixture of ethanol and n-hexane as a suitable replacement to the commonly used toxic n-hexane solvent for the extraction of oil from loofah seeds.

**Keywords:** Waste management, *Luffa cylindrica*, artificial neural network, optimisation, oil extraction.

**Submitted:** May 02, 2018. **Accepted:** June 07, 2019.

**Cite this:** Eletta O, Adewoye L, Mustapha S, Adeniyi A, Ogunleye O, Aladerokun O, et al. MODELLING AND OPTIMISATION OF OIL EXTRACTION FROM LOOFAH (*Luffa cylindrica*) SEEDS USING BINARY SOLVENT MIXTURE. JOTCSB. 2019;2(2):57-68.

**\*Corresponding author.** E-mail: [modeletta@unilorin.edu.ng](mailto:modeletta@unilorin.edu.ng); [modeletta@hotmail.com](mailto:modeletta@hotmail.com).

### INTRODUCTION

The World is becoming more conscious of the environment with increasing replacement of synthetic products with naturally derived products (1). As a result, an increase in the demand for seed oils as raw materials for chemical industries is observed. Loofah oil-based derivatives could find wider markets worldwide with the recent industrial attention to its renewability and global friendliness, thereby increasing the number of research aimed at harnessing its seed oils for various applications (2-4).

Over the years, solvent extraction has been an efficient and reliable means of extracting oil from seeds or oil-bearing materials. Currently, n-hexane solvent usually obtained from petrochemical sources is used extensively for oil extraction. However, this solvent is identified as an air pollutant which has been known to react with other pollutants to produce ozone and some photochemical oxidants (5). Consequently, environmental and health concerns have increased interest in the search for alternative solvents that would lead to a decrease in the emissions of volatile organic compounds to the environment. The interest is also aimed at, avoiding the

challenge of potential traces of hexane in the oil after refining.

The most feasible alternative to hexane extraction appears to be the complete or partial replacement of this solvent by other organic solvents recognized as being more environmentally safe. A review of past studies carried out at both laboratory and pilot scales show the use of an alcohol such as ethanol and isopropanol for oil extraction to be very promising (5-7). Ethanol is being investigated for considering its suitability to serve as a substitute to n-hexane because of the economic advantage and the fact that, it could be produced from a large variety of biological items (including biological wastes) by employing simple technology. Moreover, natural alcohol can be gotten by fermentation and is recognized as non-toxic and has less handling risks than that of n-hexane. Replacement of n-hexane with ethanol as a solvent for extraction will also avoid potential toxicity of the residual cake which could be used as meals for animal feedstock (5). Some previous studies had been reported on the extraction of oil from loofah seed using hexane as a solvent (8-11). However, the use of ethanol or its binary mixture as a possible replacement to n-hexane solvent for the extraction of oil from loofah seeds has not been reported elsewhere.

Hence, this study was undertaken to investigate the feasibility of using ethanol solvent and its binary mixture with hexane as a suitable solvent for a complete or partial replacement to the commonly used, toxic hexane solvent for the extraction of oil from loofah seeds. The effect of process parameters such as binary solvent (n-hexane/ethanol) composition at various extraction temperature

and extraction time on the oil yield was investigated and optimisation was performed in order to propose a feasible binary solvent composition with better oil yield and low toxicity. Predictive models for oil yield as a function of the studied parameters were developed using RSM and ANN and the fatty acid constituent of the extracted oil was analysed.

**MATERIAL AND METHODS**

**Sample Collection and Preparations**

Dried and matured loofah fruits were collected and prepared by opening the dried fruits and removing the seeds from the spongy fruits. The seeds were air dried for easy removal of the shell after which the seeds were oven – dried at 60 °C to constant weight before grinding to increase the surface area for oil extraction. All the reagents used were analytical grade (BDH Chemical, England and Merck Chemical, Germany).

**Design of experiments**

Central composite face-centered design (CCFCD) under the response surface methodology (RSM) was used to study the individual and inter-relationships among the three studied factors (temperature, extraction time, and solvent composition) towards the response (oil yield). CCFCD is characterised by 2n axial runs, 2n factorial runs and six central runs. For a three-factor scenario where n is equal to three (3), it translates to 6 axial points, 8 factorial points and 6 replicates at the centre which gives a total of 20 experimental runs. The coded levels and ranges for the three studied factors are presented in Table 1. The solvent compositions are presented in terms of percentage composition of the binary solvent mixture with respect to n-hexane.

**Table 1.** Independent variables (factors) and their coded levels for CCFCD.

Independent Variable (Factors)	Coded Symbol	Units	Range and Levels		
			-1	0	+1
Temperature	x1	°C	40	50	60
Time	x2	min	150	210	270
% Binary solvent composition with respect to hexane*	x3	%	0	50	100

The optimum conditions for the response (oil yield) were determined using the optimal model predictor quadratic equation (12) given as:

$$Y = b_0 + \sum_{i=1}^n b_{ii}x_i + (\sum_{i=1}^n b_{ii}x_i)^2 + \sum_{i=1}^{n-1} \sum_{j=i+1}^n b_{ij}x_i x_j \tag{1}$$

Where Y is the predicted response (oil yield), bo is the constant coefficients, bii is the quadratic coefficients, bij is the interaction coefficients and xi, xj are the coded values of the variables considered. Design Expert software (version 6.0.8) was employed to test

the significance of the quadratic model generated and, analysis of variance (ANOVA) was used to determine the lack of fit and the effect of linear, quadratic and interaction terms on oil extraction (13). The characteristics of the reliability of the analysis carried out was measured by the variability in the observed response value expressed by the coefficient of determination R<sup>2</sup>, the probability P – value (95% confidence level) and, Fisher’s test.

### ANN modelling for loofah oil extraction

Levenberg-Marquardt Back Propagation Algorithm is widely used as the learning algorithm for artificial neural networks (ANN) in the multi-layered feed forward networks (14). This method verifies the predicted output using the learning result and continuously adjusts the difference between the target result and the result calculated by the model so as to minimize the error value. All neurons in the neural network model are divided into an input layer, a hidden layer, and an output layer depending on the function, and each layer is functionally connected. In this work, the hyperbolic tangent sigmoid (tansig) was used as the transfer function for both the input layer to hidden layer mapping and hidden layer to output layer mapping. The ANN architecture assembled contain an input layer with three neurons (extraction temperature, extraction time, and solvent composition) and an output layer with one neuron (oil yield). The number of neurons in the hidden layer of the MLP was determined experimentally by identifying the number of neurons with minimum error value from a range of neuron numbers tested. The experimental data set obtained from the design of experiments was divided into three subsets in order to obtain the desired ANN model. For this study, 70% of the data set was used for training, 15% was applied for validation, while the reliability of the model was tested with the remaining 15% of the data set.

### Performance evaluation of RSM and ANN

The performance of RSM and ANN was compared using statistical parameters such as mean square error (MSE), average absolute deviation (AAD), correlation coefficient (R), and coefficient of determination ( $R^2$ ).

### Oil extraction

Extraction of loofah seed oil was carried out using a Soxhlet apparatus. 4 g of pulverized seed sample and 50 mL of solvent was used for each combination of the process variables based on the design of experiment for the CCFCD (Table 2). The extracted oil yield was expressed in percentage, which was evaluated as the ratio of the weight of oil extracted to the weight of the loofah seed powder sample used (Equation 2). Each test was repeated three times and the average value was determined and reported.

$$\text{Oil Yield (\%)} = \frac{\text{Weight of Extracted Oil}}{\text{Weight of the Seed}} * 100 \quad (2)$$

Prior to the physicochemical analyses, purification of the extracted crude loofah seed oil was carried out by degumming and de-

acidification according to the procedure reported by Audu et al. (11).

### Physicochemical properties of the oil extract

The physicochemical properties such as viscosity, acid value, free fatty acid, saponification value, iodine value and peroxide value of the crude (CLSO) and refined (RLSO) extracted loofah seed oil were determined by standard methods (11, 15).

### Fatty acid analysis of the extracted oil

The CLSO and RLSO were further characterised using Agilent 7890A Gas Chromatography (GC) coupled to Mass spectrometer (5975C) with triple axis detector and also equipped with an auto-injector (10  $\mu$ L syringe) for the analysis of the fatty acids in the extracted oil sample. Helium gas was used as the carrier gas. The chromatographic separation was performed on a capillary column having a specification (length 30 m, internal diameter 0.2  $\mu$ m, and thickness 250  $\mu$ m) and treated with phenyl methyl silox. The column temperature was set up from 35  $^{\circ}$ C to 250  $^{\circ}$ C for the total run time of 47.5 min. The injection volume was 1  $\mu$ L and, injection temperature was 300  $^{\circ}$ C for the GC. For the mass spectroscopy, the solution software provided by the supplier was used to control the system and acquired the data. Identification of the compounds was carried out by comparing the mass spectra obtained with standard mass spectra from the NIST library (NIST11).

## RESULTS AND DISCUSSION

### Design of experiments

The experimental design and results are given in Table 2. Run 15 – 20 at the center point were used to determine the experimental error and the reproducibility of the data. The highest oil yield of 30.0% was obtained at 100% ethanol solvent composition as shown in Table 2 (Run 2). The percentage oil yield obtained using 100% ethanol ranged from 19.0% to 30.0% with the mean value of 24.8%. As shown in Table 2 (Run 8), 100% n-hexane gave the highest oil yield of 18.0% and this value is slightly greater than the highest oil yield (17.0%) obtained from the mixture of hexane (50%) and ethanol (50%) under Run 10.

Several studies had shown that non – polar solvents (n-hexane) always gives high oil yield due to the absence of OH (13, 16, 17). However, this study revealed that the highest yield was obtained from polar solvent (ethanol) which may suggest that, some components in the LSO impaired the retardation of activities on the polar solvent or

other materials rather than oil was extracted thereby leading to higher yield. Some past studies also confirmed that extraction of

biocompounds such as phenolic compounds in solvent extraction process has been well favoured with polar solvents (6, 18, 19).

**Table 2.** CCFCD Experimental design matrix with coded and real values.

Run	Coded Values			Real Values			Oil Yield (%)		
	x1	x2	x3	Extraction Temp. (°C)	Time (min)	Binary solvent composition*(%)	Experimental	RSM	ANN
1	-1	-1	-1	40	150	0	28.000	28.430	27.999
2	1	-1	-1	60	150	0	30.000	29.130	29.990
3	-1	1	-1	40	270	0	22.000	21.330	21.997
4	1	1	-1	60	270	0	19.000	19.030	18.998
5	-1	-1	1	40	150	100	3.000	2.830	3.010
6	1	-1	1	60	150	100	11.000	11.530	11.424
7	-1	1	1	40	270	100	11.000	11.730	11.001
8	1	1	1	60	270	100	18.000	17.430	18.003
9	-1	0	0	40	210	50	15.000	14.670	15.624
10	1	0	0	60	210	50	17.000	17.870	17.000
11	0	-1	0	50	150	50	13.000	13.070	13.001
12	0	1	0	50	270	50	12.000	12.470	11.998
13	0	0	-1	50	210	0	24.000	25.070	25.614
14	0	0	1	50	210	100	12.000	11.470	12.004
15	0	0	0	50	210	50	15.000	14.820	14.999
16	0	0	0	50	210	50	15.000	14.820	14.999
17	0	0	0	50	210	50	15.000	14.820	14.999
18	0	0	0	50	210	50	15.000	14.820	14.999
19	0	0	0	50	210	50	15.000	14.820	14.999
20	0	0	0	50	210	50	15.000	14.820	14.999

\* Composition of the binary (n-hexane/ethanol) solvent with respect to n-hexane.

### Development of regression model equation using RSM

The development of the regression equation was performed using CCFCD under the RSM to describe the correlation between oil yield (%) and the studied factors (temperature, extraction time, and solvent composition). The quadratic model was developed using the Design Expert software version 6.0.8 (STAT-EASE Inc., Minneapolis, USA). The final empirical model in terms of coded factors for the oil yield (Y<sub>oil yield</sub>) is given in Equation 3:

$$Y_{oil\ yield} = +14.82 + 1.60x_1 - 0.30x_2 - 6.80x_3 + 1.45x_1^2 - 2.05x_2^2 + 3.45x_3^2 - 0.75x_1x_2 + 2.00x_1x_3 + 4.00x_2x_3 \quad (3)$$

where x<sub>1</sub> = Extraction temperature, x<sub>2</sub> = Extraction time, x<sub>3</sub> = Solvent composition

The regression equation (Equation 3) indicates that the oil yield was negatively correlated with extraction time and solvent composition and positively correlated with the extraction temperature within the experimental range (Table 1) considered for the three studied variable. Thus, an increase in extraction time decreased the oil yield. Likewise, an increase

in percentage composition of hexane in the binary mixture decreased the oil yield and this is in agreement with oil yield range of 19.0% - 30.0% and 3.0% - 18.0% (Table 2) obtained experimentally for 0% hexane (100% ethanol) and 100% hexane (0% ethanol) respectively. It was also observed from Equation 3 that the magnitude of coefficients of solvent composition was larger than the coefficients for extraction temperature and extraction time, which indicated the solvent composition, had much significant effect on the oil yield than the individual or combined effect of extraction temperature and time.

The analysis of variance (ANOVA) for the non-linear regression equation (Equation 3) was used to also highlight the adequacy of the models and their significance. The Fisher's variance ratio F-value and Prob > F for the oil yield were 150.30 and < 0.0001, respectively (Table 3) which implied that the quadratic model suggested for the response (oil yield) is significant. In addition, Table 3 showed that x<sub>1</sub>, x<sub>3</sub>, x<sub>12</sub>, x<sub>22</sub>, x<sub>32</sub>, x<sub>1x2</sub>, x<sub>1x3</sub>, and x<sub>2x3</sub> were the significant terms while the x<sub>2</sub> (extraction time) was the only insignificant term in the oil yield model with "Prob > F"

greater than 0.05. In the same vein, the model term x3 (solvent composition) with F-value of 875.46 and Prob > F less than 0.0001 imposed the most significant effect on the oil yield. The relative predictive power of the quality of the model R2 was found to be 0.993 which is in

reasonable agreement with the adjusted R2 (0.986) and predicted R2 of (0.903). More so, a desirable ratio of 51.18 was obtained for the adequate precision which indicated an adequate signal, thus the model can be used to navigate the design space (12, 20-22).

**Table 3.** ANOVA for response surface quadratic model for loofah seed oil yield.

Source	Sum of Squares	Degree of Freedom	Mean Square	F - Value	Prob > F
Model	714.47	9	79.39	150.30	< 0.0001 <sup>a</sup>
x1	25.60	1	25.60	48.47	< 0.0001 <sup>a</sup>
x2	0.90	1	0.90	1.70	0.2210 <sup>b</sup>
x3	462.40	1	462.40	875.46	< 0.0001 <sup>a</sup>
x12	5.82	1	5.82	11.02	0.0078 <sup>a</sup>
x22	11.51	1	11.51	21.78	0.0009 <sup>a</sup>
x32	32.82	1	32.82	62.13	< 0.0001 <sup>a</sup>
x1x2	4.50	1	4.50	8.52	0.0153 <sup>a</sup>
x1x3	32.00	1	32.00	60.59	< 0.0001 <sup>a</sup>
x2x3	128.00	1	128.00	242.34	< 0.0001 <sup>a</sup>
Residual	5.28	10	0.53		

<sup>a</sup>significant at 95% confidence level, <sup>b</sup> not significant at 95% confidence level.

### Process optimisation

Although the highest oil yield of 30.0% was obtained at 100% ethanol solvent composition as shown in Table 2 (Run 2), this study tends to accommodate the product separation challenges that might arise from the use of ethanol alone as a solvent and hence optimization study was carried out to propose a feasible binary solvent of ethanol and n-hexane. The California division of occupational safety and health reported the permissible exposure limit (PEL) as an eight-hour time-weighted average (TWA) for ethanol and n-hexane as 1000 ppm and 500 ppm, respectively (23). The PEL values confirm ethanol as far less toxic compared to hexane making ethanol to be a suitable replacement or a solvent that could serve to reduce the concentration of the much toxic hexane solvent from their binary mixtures. The Process optimization was carried out using design expert software to find the optimum

process parameters to maximize the percentage of oil extracted from loofah seed. The best solution for optimization within the experimental range of the studied independent variables is usually selected based on the highest desirability or its closeness to unity (6, 24). The maximum oil yield of 27.67% was obtained with the desirability of 1.0. The optimum conditions for the variables studied were obtained at extraction temperature (40 oC), extraction time (151.9 min) and solvent composition (2% n-hexane / 98% ethanol). This is an indication that, this new proposed binary solvent mixture could serve as a more efficient alternative solvent mixture with less toxic effect to achieve a better oil yield when compared with the widely used highly toxic n-hexane solvent. The model validation was carried out and the experimental oil yield (28.5%) was found to agree satisfactorily with the predicted oil yield (27.67%), with an error of 2.91% (Table 4).

**Table 4 .** Model validation.

Extraction Temperature, x <sub>1</sub> (°C)	Extraction Time, x <sub>2</sub> (min)	Binary solvent composition with respect to n-hexane, x <sub>3</sub> (%)	Oil Yield, Yoil yield (%)		
			Predicted	Experimental	Error
40.00	151.90	2.00	27.67	28.50	2.91

The combined interaction effects of the three studied variables on the yield of loofah seed oil are shown on the three-dimensional surface response plots (Figure 1a – d). Figure 1a and 1b show the response surface plot for the combined effect of extraction temperature and time on oil yield at the fixed solvent composition of 100% ethanol and optimum

solvent composition of 2% n-hexane and 98% ethanol. The response surface plot in Figure 1c shows the combined effect of solvent composition and extraction temperature on oil yield at the fixed extraction time of 151.9 min while Figure 1d shows the response surface plot for the combined effect of solvent composition and extraction time on oil yield at

a fixed extraction temperature of 40 °C. The curvatures obtained from Figure 1c - d clearly indicates that solvent composition imposed the most significant effect on the oil yield.

Although the level of contributions may differ, all the studied variables contributed either individually or by way of interaction to the yield of loofah seed oil.

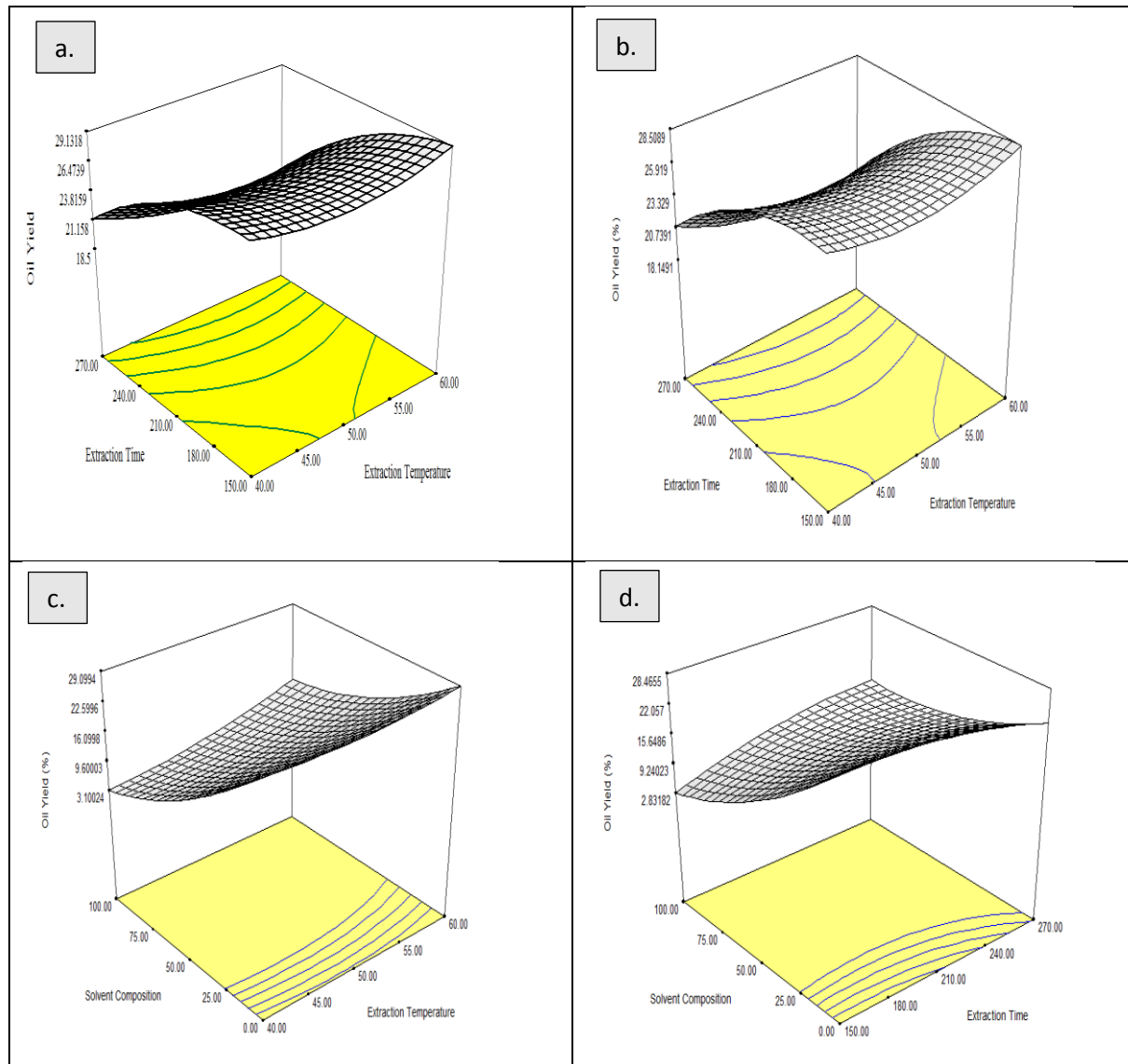


**Figure 1.** Response surface plot for the combined effect of (a) temperature and time on oil yield at fixed solvent composition of 100% Ethanol (b) temperature and time on oil yield at optimum conditions (c) solvent composition and temperature on oil yield at optimum conditions (d) solvent composition and time on oil yield at optimum conditions.

**ANN modelling**

The ANN model was developed using the MATLAB R2015a neural network toolbox (Math Works, Inc., Natick, MA, USA). The optimal number of neurons in the hidden layer of the MLP-ANN determined by trial and error was found to be neuron 12 and the best topology chosen for the ANN model was 3 - 12 - 1.

Hence, the ANN optimum architecture assembled contain an input layer with three neurons (extraction temperature, extraction time, and solvent composition), a hidden layer with 12 neurons and an output layer with one neuron (oil yield) as shown in Figure 2.

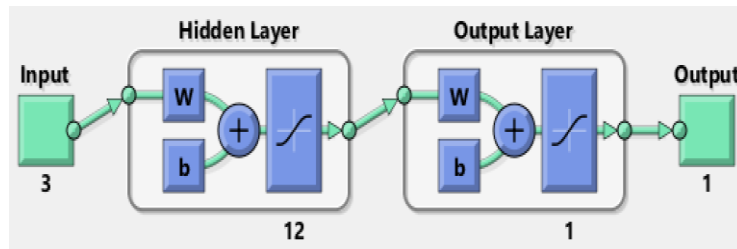


Figure 2. ANN architecture for prediction of oil yield.

The regression plots showing the coefficient of correlation for training, testing, validation and whole data sets are depicted in Figure 3. The predicted values obtained for oil yield from the

ANN model is presented in Table 2. The predicted oil yield from the ANN model was in the range of 3.01% to 29.99%.

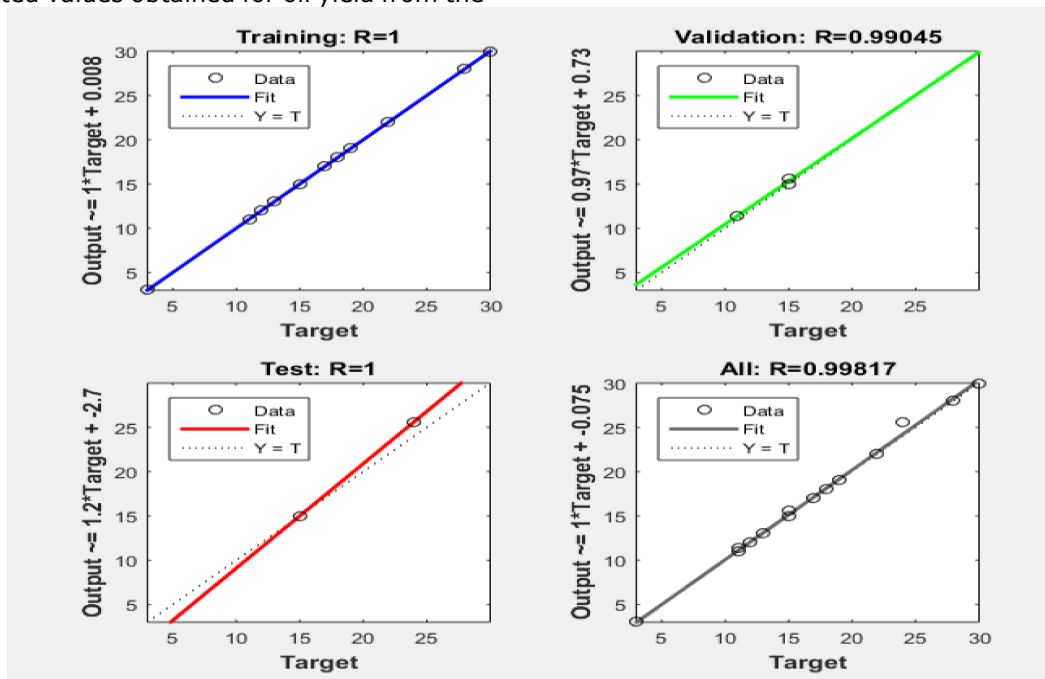
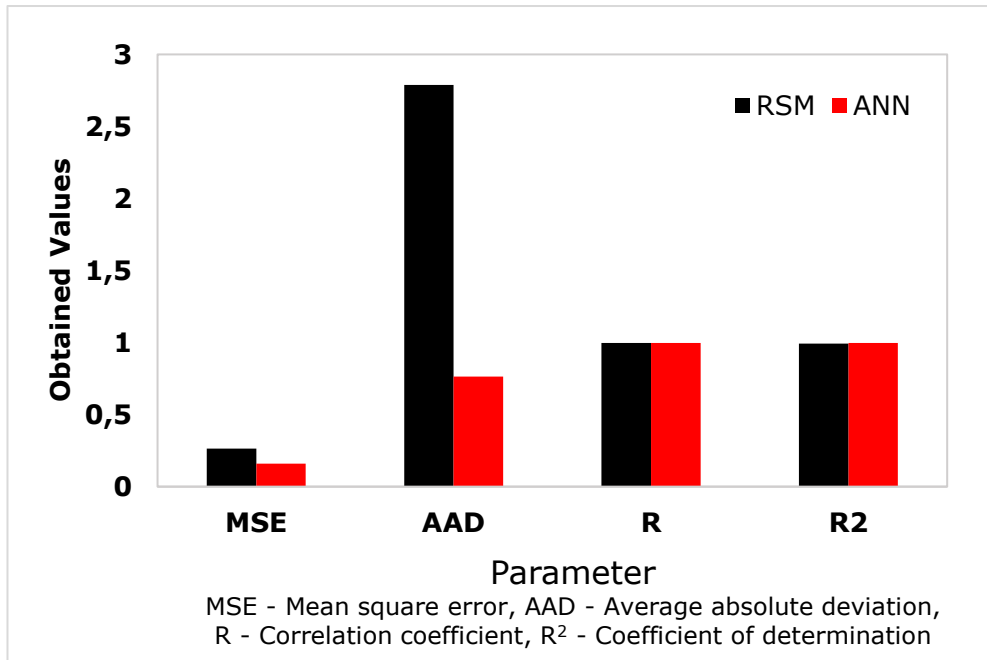


Figure 3. Regression plots for the ANN model.

**Performance evaluation of RSM and ANN**

The evaluation of the predictive capabilities of RSM and ANN for the oil yield was carried out and the results were compared. Statistical parameters such as MSE, AAD, R and R<sup>2</sup> were used to compare the performance of the two developed models. The results obtained (Figure 4) shows that the ANN model performed better than the RSM model, although the performance was satisfactory for both models. The mean square error (MSE)

values indicated that lower errors were obtained with the ANN model (0.1587) compared to the RSM model (0.2636). The average absolute deviation (AAD) of the ANN model (0.7632) was also found to be lower compared to the RSM model (2.7887). More so, the ANN model had higher precision and accuracy as shown with the values of R (0.9982) and R<sup>2</sup> (0.9964) compared with R (0.9963) and R<sup>2</sup> (0.9927) obtained from the RSM model.



**Figure 4.** Comparison of statistical evaluation of the RSM and ANN models.

The plot of experimental and predicted oil yield values against the experimental run is shown in Figure 5. The figure confirms that the predicted values for the ANN model were much more closely aligned with the experimental values than the predicted values of the RSM model. The results from this study are in agreement with previous studies on the superiority of ANN over response surface methodology (25-27). Avramović et al. (26) in their study on predicting the biodiesel yield from ethanolsis of sunflower oil using calcium

oxide as catalyst showed that ANN is more superior to RSM. Betiku et al. (25) compared the performance of RSM, ANFIS and ANN for the predictive modelling of acid pre-treatment of palm kernel oil and their result showed that ANN was the best of the three modelling tools. Soji-Adekunle et al. (27) modelled the synthesis of waste cooking oil methyl esters using ANN and RSM and their findings also confirmed ANN as a better predicting tool than the RSM.

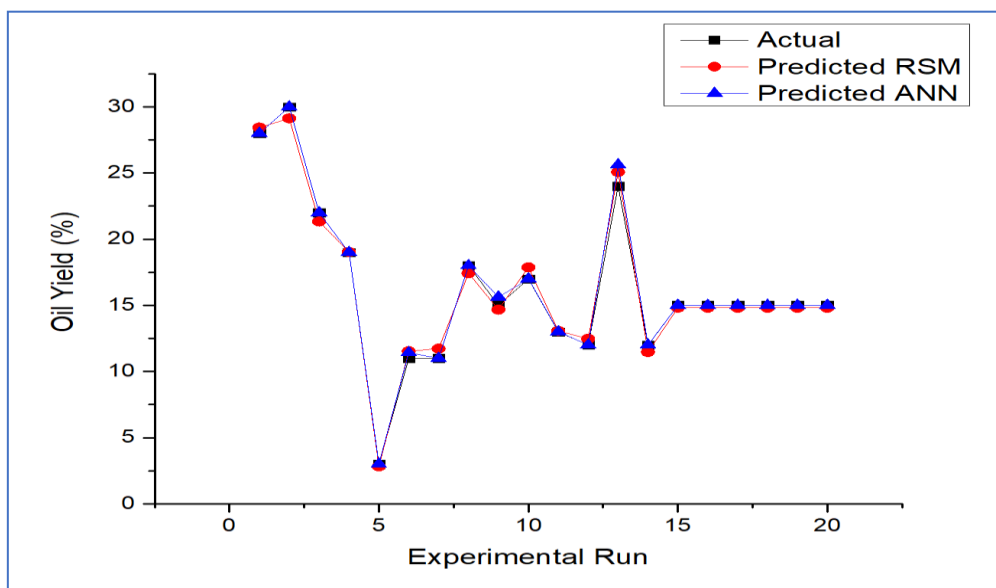


**Figure 5.** Actual and predicted oil yield from ANN and RSM against the experimental run.

### Physicochemical properties of loofah seed oil

The physicochemical properties of the crude loofah seed oil (CLSO) and refined loofah seed oil (RLSO) were analysed and the results presented in Table 5. The result showed that the percentage oil yield (27.67%) obtained in this study using the proposed optimum binary solvent was found to be much higher compared to the oil yield of 14.08% reported by Audu et al. (11) for loofah seed oil extraction using only n-hexane solvent. Specific gravity and viscosity are important physical characteristics which indicate the handling, storage and operational conditions of oils and fuels (28). The specific gravity of both the crude and refined loofah seed oil was 0.86 and 0.84 respectively. These values are close to the standard range of 0.87 – 0.90 for biodiesel production (29). Moreover, the viscosity of crude oil extract was found to reduce from 0.109 N.s/m<sup>2</sup> to 0.078 N.s/m<sup>2</sup> which could be as a result of a degumming step in the refining process. These observed properties suggest that the refined oil could find good application in the manufacture of lubricants and biofuel industries (30). A similar trend was also observed from the viscosity results reported by Audu et al. (11).

From Table 5, the acid values for CLSO (3.67 mgKOH/g) and RLSO (3.33 mgKOH/g) obtained in this study were less than 10 mgKOH/g which is the recommended standard value for non-virgin edible oils (31). This is an indicator of the edibility of the extracted oil and its suitability for industrial purposes. In addition, the reduction in the acid value of the refined oil (RLSO) suggests that oil refining assisted in improving the quality of the oil and can easily be transesterified to biodiesel by acid catalysed system. The low acid values from this study also agree with values reported by Audu et al. (11) (3.72 mgKOH/g)

and Gafar et al. (8) (2.34 mgKOH/g). However, this observation is in contrast to the acid value of 34.15 mgKOH/g reported by Ozulu (9) for loofah seed oil extraction using only n-hexane solvent. The result of saponification values obtained from this study (Table 5) shows that the RLSO has a higher molecular weight than CLSO since saponification value is inversely proportional to the molecular weight of the oil. This is an indication that the refining process might have promoted saturation of the oil (32).

The iodine value measures the degree of unsaturation of fats and oils and can be used in predicting the drying property of oils. Usually, non-drying oils have iodine values between 80 – 120, while semi-drying oils have between 120 – 150 and drying oils have iodine values greater than 150 (10). Thus, the iodine values of 86.53 mgI<sub>2</sub>/g and 80.15 mgI<sub>2</sub>/g obtained for CLSO and RLSO, respectively can be classified as a non-drying oil. This iodine values obtained compare well with the iodine value of 82.29 mgI<sub>2</sub>/g and 82.56 mgI<sub>2</sub>/g reported by Ozulu (9) and Audu et al. (11), respectively for LSO. Oils with values less than 120 mgI<sub>2</sub>/g according to EN 14214 (European committee for standardisation) may find use in surface coating applications like paints, resins, printing inks and also suitable as feedstock for biodiesel production. The peroxide value of the RLSO (5.3 meq/kg) was low when compared to that of the CLSO (8.01 meq/kg) which represented 34.5% reduction in the CLSO value. The low value of the refined oil could be as a result of gummy deposits removed during the refining process which indicates the stability of the refined oil over the crude oil. The value also suggests that the refined oil would have a longer shelf life than that of the crude loofah seed oil.

**Table 5.** Physicochemical properties of loofah seed oil (LSO).

Properties	Present Study		Audu et al. (11)	
	CLSO	RLSO	CLSO	RLSO
Oil yield (%)	-	27.67	-	14.08
Specific gravity	0.86	0.84	0.93	0.90
Viscosity @ 32 °C x10 <sup>-1</sup> , (N.s/m <sup>2</sup> )	1.09	0.78	1.045	1.045
Acid value (mgKOH/g)	3.67	3.33	3.82	3.72
Saponification value (mgKOH/g)	128	127.70	149	148.50
Iodine value (mgI <sub>2</sub> /g)	86.53	80.15	-	82.56
Peroxide value (meq/kg)	8.10	5.30	-	5.43
Free fatty acid (%)	1.85	1.68	2.52	2.18

NB: CLSO – Crude loofah seed oil, RLSO – Refined loofah seed oil.

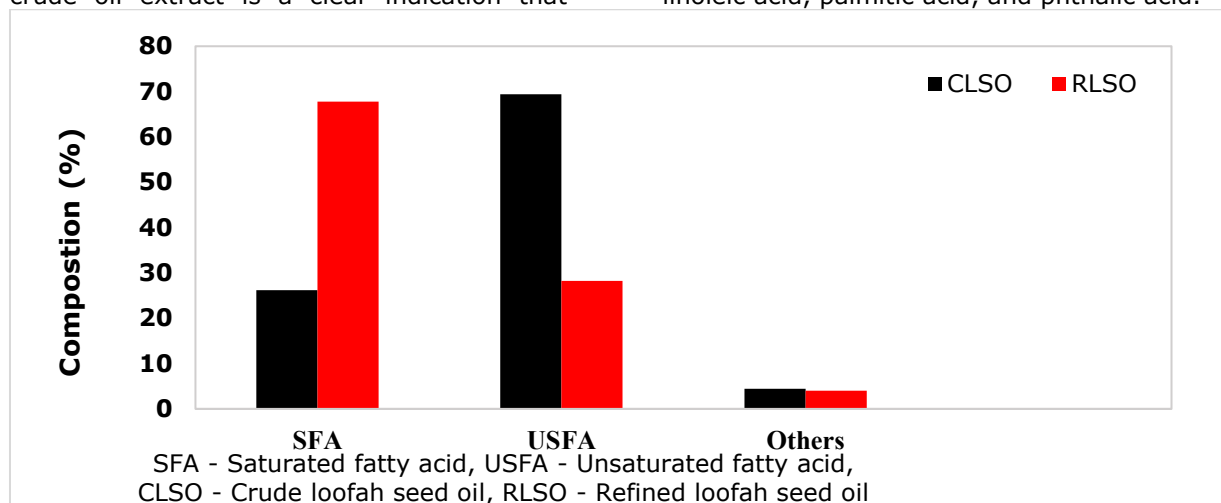
### Fatty acid analysis of the extracted oil

A GC-MS analysis was conducted to investigate the fatty acids present in the

extracted oil. The summary of the fatty acid profile for crude loofah seed oil and refined loofah seed oil are presented in Figure 6. The

composition of saturated fatty acid predominantly palmitic acid was found to be 67.75% in the refined oil sample. This high value of saturated fatty acid obtained in the refined oil when compared with the 26.15% composition of saturated fatty acid in the crude oil extract is a clear indication that

refining of the loofah oil promoted saturation. More so, it could be inferred that the refined extracted oil is saturated oil which is in line with results of previous researches on loofah seed oil extraction (8, 9, 28). The fatty acid present in the refined loofah seed oil includes linoleic acid, palmitic acid, and phthalic acid.



## CONCLUSIONS

This study has proposed a new binary mixture of ethanol/n-hexane as a suitable replacement to the commonly used, toxic n-hexane solvent for the extraction of oil from loofah seeds. The optimal condition was obtained at extraction temperature (40 °C), extraction time (151.9 min), and solvent composition (98% ethanol /2% n-hexane). Results of the statistical analysis showed that the solvent composition imposed the most significant effect while extraction time contributed the least effect on the yield of loofah seed oil (LSO). The performance evaluation of the developed predictive models shows that the ANN model performed better than the RSM model, although the performance of both models was satisfactory. Comparing the result of the properties of CLSO with RLSO, it is observed that, the refining process promotes saturation of the extracted oil with a high percentage of 67.75% palmitic acid found in RLSO.

## ACKNOWLEDGEMENT

The authors are grateful to the technologists in the Department of Chemical Engineering in both, University of Ilorin, and Ladoke Akintola University of Technology, Ogbomoso, Nigeria for the various roles played in facilitating the laboratory analysis carried out in this study.

## REFERENCES

1. Amoo I, Eleyinmi A, Ilelaboye N, Akoja S. Characterisation of oil extracted from gourd (*Cucurbita maxima*) seed. *Journal of Food Agriculture and Environment*. 2004;2(2):38-39.

2. Abayeh O, Garba I, Adamu H, Abayeh O. Quality characteristics of *Luffa aegyptiaca* seed oil. *International Journal of Scientific & Engineering Research*. 2013;4(4):11-15.

3. Sujatha D, Chithakari R, Raghuvardhan L, Prasad B, Khan G. In vitro plantlet regeneration and genetic transformation of sponge gourd (*Luffa cylindrica*). *African Journal of Plant Science*. 2013;7(6):244 - 252.

4. Ndukwe G, Amupitan J, Badmus N. Preliminary investigation on the antibiotic and fungicidal activities of the extracts from the seeds of *Luffa cylindrica*. *Journal of Engineering Technology*. 2001;8(2):3202 - 3207.

5. Ozulu O. Production and characterization of biodiesel from *Luffa Cylindrica* seed oil: Nsukka, University of Nigeria; 2015.

6. Bal K, Bal Y, Lallam A. Gross morphology and absorption capacity of cell-fibers from the fibrous vascular system of loofah (*Luffa cylindrica*). *Textile research journal*. 2004;73(4):241 - 247.

7. Gafar M, Itodo A, Warra A, Wyasu G, Usman J. Physico-chemical, cold saponification and GC-MS analysis of sponge gourd (*Luffa cylindrica* Linn.) seed oil. *International J Modern Chem*. 2012;3(2):98 - 107.

8. Oboh I, Aluyor E. *Luffa cylindrica*-an emerging cash crop. *African Journal of Agricultural Research*, 2009;4(8):684 -688.

9. Ajiwe V, Ndukwe G, Anyadiegwu I. Vegetable diesel fuels from *Luffa cylindrica* oil, its methyl ester and ester-diesel blends. *Chemistry Class Journal*. 2005;2(2):1-4.

10. Ferreira-Dias S, Valente D, Abreu J. Comparison between ethanol and hexane for oil extraction from *Quercus suber* L. fruits. *Grasas Aceites*. 2003;54(4):378 - 383.
11. Araromi D, Alade A, Bello M, Bakare T, Akinwande B, Jameel A, et al. Optimization of oil extraction from pitanga (*Eugenia Uniflora* L) leaves using simplex centroid design (SCD). *Separation Science and Technology*. 2017;52(8):1341-1349.
12. Sineiro J, Domínguez H, Núñez M, Lema J. Ethanol extraction of sunflower oil in a pulsing extractor. *Journal of the American Oil Chemists' Society*. 1998;75(6):753-754.
13. Auta M, Hameed B. Optimized waste tea activated carbon for adsorption of Methylene Blue and Acid Blue 29 dyes using response surface methodology. *Chemical Engineering Journal*. 2001;175(1):233 - 243.
14. Mani S, Jaya S, Vadivambal R. Optimization of solvent extraction of Moringa (*Moringa oleifera*) seed kernel oil using response surface methodology. *Food and Bioproducts Processing*. 2007;85(4):328 - 335.
15. Audu T, Aluyor E, Egualeona S, Momoh S. Extraction and characterization of *Chrysophyllum albidum* and *Luffa cylindrica* seed oils. *Food Chemistry*. 2013;8(3):201 - 208.
16. Horwitz W. Official methods of analysis of the AOAC International 2000.
17. Barchan A, Bakkali M, Arakrak A, Pagán R, Laglaoui A. The effects of sol-vents polarity on the phenolic contents and antioxidant activity of three *Mentha* species extracts. *Int J Curr Microbiol App Sci*. 2014;3(11):399 - 412.
18. Jayaprakasha G, Singh R, Sakariah K. Antioxidant activity of grape seed (*Vitis vinifera*) extracts on peroxidation models in vitro. *Food Chemistry*. 2001;73(3):285 - 290.
19. Lee Y, Huang G, Liang Z, Mau J. Antioxidant properties of three extracts from *Pleurotus citrinopileatus*. *LWT-Food Science and Technology*. 2007;40(5):823 - 833.
20. Ozsoy N, Can A, Yanardag R, Akev N. Antioxidant activity of *Smilax excelsa* L. leaf extracts. *Food Chemistry*. 2008;110(3):571 - 583.
21. Adewoye L, Mustapha S, Adeniyi A, Tijani J, Amoloye M, Ayinde L. Optimization of nickel (ii) and chromium (iii) removal from contaminated water using sorghum bicolor. *Nigerian Journal of Technology*. 2017;36(3):960-972.
22. Khuri A, Mukhopadhyay S. Response surface methodology. *Wiley Interdisciplinary Reviews: Computational Statistics*. 2010;2(2):128 - 149.
23. Rashid U, Anwar F, Ashraf M, Saleem M, Yusup S. Application of response surface methodology for optimizing transesterification of *Moringa oleifera* oil: Biodiesel production. *Energy Conversion and Management*. 2011;52(8):3034 - 3042.
24. Ibeto C, Okoye C, Ofoefule A. Comparative study of the physicochemical characterization of some oils as potential feedstock for biodiesel production. *ISRN Renewable Energy*. 2012:1- 5.
25. Jerković I, Rajić M, Marijanović Z, Bilić M, Jokić S. Optimization of supercritical CO<sub>2</sub> extraction of dried *Helichrysum italicum* flowers by response surface methodology: GC-MS profiles of the extracts and essential oil. *Separation Science and Technology*. 2016;51(18):2925 - 2931.
26. Ejikeme P, Egbounu C, Anyaogu I, Eze V. Fatty acid methyl esters of melon seed oil: Characterisation for potential diesel fuel application. *Leonardo Journal of Sciences*. 2011;18:75 - 84.
27. Audu TOK, Aluyor EO, Egualeona S, Momoh SS. Extraction and Characterization of *Chrysophyllum albidum* and *Luffa cylindrica* Seed Oils. *Petroleum Technology Development Journal*. 2013;3(1):1-7.
28. Onyeike E, Acheru G. Chemical composition of selected Nigerian oil seeds and physicochemical properties of the oil extracts. *Food Chemistry*. 2002;77(4):431 - 437.
29. Sayeed M, Ali M, Sohel F, Khan G, Yeasmin M. Physico-chemical characteristics of *Mesua ferrea* seed oil and nutritional composition of its seed and leaves. *Bulletin of the Chemical Society of Ethiopia*. 2004;18(2):157 - 166.
30. Kittiphoom S, Sutasinee S. Mango seed kernel oil and its physicochemical properties. *International Food Research Journal*. 2013;20(3):1145-1149.





## EFFECT OF THE ACID TYPE ON THE NATURAL ZEOLITE STRUCTURE

Fehime Çakıcıoğlu-Özkan<sup>1\*</sup>  , Metin Becer<sup>1</sup>  

İzmir Institute of Technology, Chemical Engineering Department, Gülbahçe Köyü, Urla 35430, İzmir-Turkey.

**Abstract:** In this study, Clinoptilolite-rich zeolitic tuff was treated with acids such as HCl, HNO<sub>3</sub>, H<sub>2</sub>SO<sub>4</sub>, and H<sub>3</sub>PO<sub>4</sub>. The effect of periods of time (3 hours and 6 hours), concentration (1 M, 2 M, 3 M, 5 M, and 10 M) and the type of acid were taken as parameters. In the characterization of the zeolites, XRD, ICP-AES, and FTIR techniques were used. As the acid concentration and the treatment time were increased, the aluminum and cation removal from the structure was increased. HCl and HNO<sub>3</sub> were more effective acids for the dealumination than H<sub>2</sub>SO<sub>4</sub> and H<sub>3</sub>PO<sub>4</sub>. It was found out that considerable change in the texture of the zeolitic tuff did not take place during the H<sub>3</sub>PO<sub>4</sub> treatment. On the other hand, acid treatment resulted in an increase in the micropore surface area and volume of the zeolite. The specific surface area of the zeolitic tuff (19 m<sup>2</sup>/g) was increased up to 213 m<sup>2</sup>/g, 236 m<sup>2</sup>/g, 202 m<sup>2</sup>/g, 118 m<sup>2</sup>/g with HCl, HNO<sub>3</sub>, H<sub>2</sub>SO<sub>4</sub>, and H<sub>3</sub>PO<sub>4</sub> treatments, respectively. In the cases of HCl and HNO<sub>3</sub>, an increase in their concentration furthermore than 5 M caused to the collapse of the structure.

**Keywords:** Acid treatment, texture, clinoptilolite, modification.

**Submitted:** November 12, 2018. **Accepted:** June 05, 2019.

**Cite this:** Çakıcıoğlu-Özkan F, Becer M. EFFECT OF THE ACID TYPE ON THE NATURAL ZEOLITE STRUCTURE. JOTCSB. 2019;2(2):69-74.

\*Corresponding author. e-mail: [fehimeozkan@iyte.edu.tr](mailto:fehimeozkan@iyte.edu.tr).

### INTRODUCTION

Zeolites are porous, crystalline, hydrated aluminum silicates of alkali and alkaline earth cations that possess a three-dimensional structure. The zeolite framework consists of an assemblage of SiO<sub>4</sub> and AlO<sub>4</sub> tetrahedra joined together in various regular arrangements through shared oxygen atoms to form an open crystal structure containing pores of molecular dimensions into which guest molecules can penetrate. The negative charge created by the substitution of an AlO<sub>4</sub> tetrahedron for a SiO<sub>4</sub> tetrahedron is balanced by exchangeable cations (e.g., Na<sup>+</sup>, K<sup>+</sup>, Ca<sup>2+</sup>, Mg<sup>2+</sup>), which are located in the structural channels and cavities throughout the structure (1).

Clinoptilolite, which is a member of the heulandite group, is the most abundant natural zeolite minerals (2). Compositions and purity vary widely among the deposits throughout the world. There is always the

problem of impurities, which block the channel system. The cations, which occupy the considerable space in the micropores of zeolites, are removed with acid treatment. Besides, to the cations, the framework aluminum may be removed. This is called as dealumination and may result with the destruction of the texture of zeolite mineral. Therefore, the advantage of the acid treatment is to remove the impurities and so develop the new pores. The disadvantage, which encountered at high acid concentration, is the dealumination that can cause the partial or total destruction of the zeolite framework. In acid treatment, besides to acid treatment conditions (acid concentration, treatment temperature and time), and the nature of acid the resistant properties of natural zeolite against to acid are all important parameters. Many of these parameters have been extensively studied for Y-zeolite (3), mordenite (4) and faujasite (5), phillipsite (6). For clinoptilolite, HCl is the widely used acid

and its effect on the texture was studied by means of N<sub>2</sub> (7, 8), H<sub>2</sub>O (9) and CO<sub>2</sub> (10) adsorption.

In this study, it aimed to present the effect of the acid (HCl, HNO<sub>3</sub>, H<sub>2</sub>SO<sub>4</sub>, H<sub>3</sub>PO<sub>4</sub>) treatment on the textural properties of natural zeolite mineral, clinoptilolite. The treated zeolite can be used as support for photocatalysis application for future study.

## MATERIALS AND METHODS

### Materials

All chemicals were of analytical grade and were used without further purification. Deionized water was used for preparation of the solutions.

### Methods

The zeolitic tuff, obtained from Gördes, (Turkey) was crushed and sieved to the particle size in the range of 850– 2000 µm. Then it was washed with distilled water for 2 hours at 60 °C to remove the soluble salts. The zeolite obtained (NCW) was dried in a vacuum (10<sup>-3</sup> mbar) oven at 160 °C for 24 hours and stored for acid treatment.

In the acid treatment, five grams of zeolite NCW and 100 mL of acid (HCl, HNO<sub>3</sub>, H<sub>2</sub>SO<sub>4</sub>, H<sub>3</sub>PO<sub>4</sub>) solutions were mixed in a water bath (GFL 1092) with a mixing rate of 200 min<sup>-1</sup> at 60 °C for 6 or 3 hours. Then zeolites are washed with double distilled water until no chloride was detected into the solution. The zeolites obtained were stored for characterization. The chemical composition of the zeolites was obtained by measuring the cation content of the solutions by means of Inductively Coupled Plasma Atomic Emission spectroscopy (ICP-AES 96, Varian). The mineralogical and crystallographic determination was made by using X-ray diffraction (X-Pert Pro Diffractometer) using CuKα radiation (λ =1.54051 Å) at 45 kV and 40 mA with a step size of 0.02° 2θ in the 5-40° 2θ range. The nitrogen adsorption isotherms of the zeolites were obtained at liquid nitrogen temperature (77 K) by using a

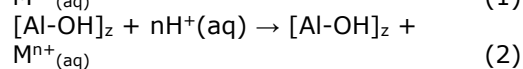
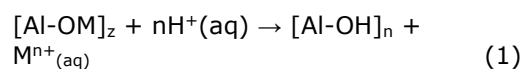
volumetric adsorption system (ASAP 2010, Micromeritics). Prior to the determination of the adsorption isotherms, the zeolites were degassed for 4 h at 350 °C. The infrared spectra (FTIR) of the zeolites in the range of 400-4500 cm<sup>-1</sup> were recorded with a Fourier transformed infrared spectrometer (FTIR-8601-Shimadzu) at room temperature by using KBr (1/50) pellet technique.

In the code of the treated zeolites obtained, the first letter shows the acid used; C for HCl, S for H<sub>2</sub>SO<sub>4</sub>, N for HNO<sub>3</sub> and P for H<sub>3</sub>PO<sub>4</sub>. The following number is the acid concentration (M). With HCl, the effect of the treatment time was also studied and coded as 6h or 3h (treatment period for 6 hours or 3 hours respectively). Treatment period with other acids is 6 hours.

## RESULTS AND DISCUSSION

The chemical composition of the washed natural zeolite (NCW) was found as (wt. %): 14.1 Al<sub>2</sub>O<sub>3</sub>, 64.2 SiO<sub>2</sub>, 1.8 MgO, 1.7 Na<sub>2</sub>O, 5.3 K<sub>2</sub>O, 1.0 CaO, 1.8 Fe<sub>2</sub>O<sub>3</sub>, and 10.3 H<sub>2</sub>O. As seen from the XRD pattern of the NCW (Figure 1), the natural zeolite is rich in clinoptilolite (2θ=9.92°, 22.49°, 30.15°) with the presence of low-cristoballite and quartz (2θ= 26.64°) as impurities. Considering the chemical composition the natural zeolite used in this study was classified as Ca-clinoptilolite (1).

In the acid treatment studies, both acid concentration and treatment time were effective; the higher the acid concentration and the longer the treatment time, the more cation and aluminum were removed from the zeolite structures, causing the increase in Si/Al ratios (Table 1). This is due to the attack of a proton to cationic [Al-OM]<sub>z</sub> and / or aluminum sites [Al-OH]<sub>z</sub> and is represented by the following reactions (11).



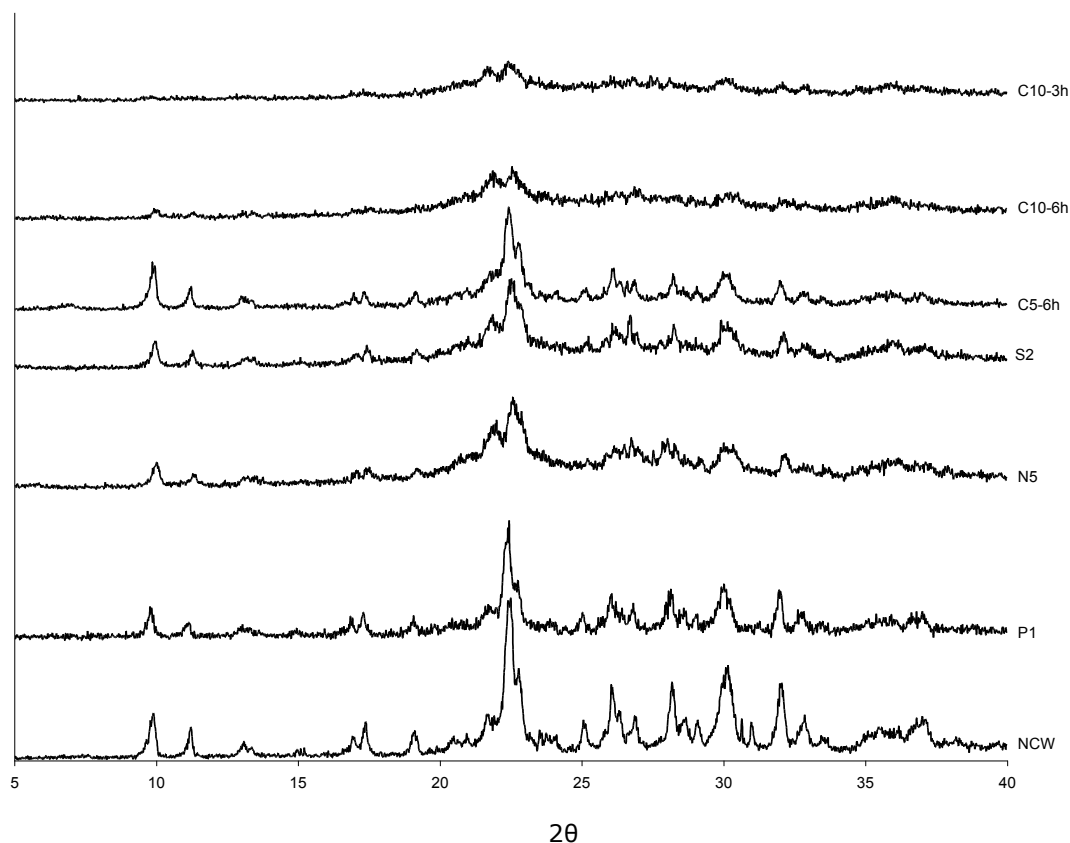


**Figure 1.** X-ray diffraction patterns of the untreated (NCW) and acid treated zeolites.

Figure 1 displays the representative XRD patterns of the natural and its acid treated forms. It was seen that HCl, HNO<sub>3</sub> and H<sub>2</sub>SO<sub>4</sub> treatments are very effective on the crystal structure of the zeolites: the patterns of the HCl treated samples showed that, as the acid concentrations and treatment period increased, intensities of the characteristic peaks decreased, meaning a loss in the crystallinities of the zeolites. From the XRD data of the HCl-treated zeolites for 6 h, it is clear that, with 5 M and 10 M HCl treatments, the characteristic peaks almost disappeared which means that the crystal structures were collapsed and the amorphous phases were generated. XRD results of HCl, H<sub>2</sub>SO<sub>4</sub> and HNO<sub>3</sub> treated samples confirmed the Si/Al ratios indicating that more framework aluminum atoms were affected leading to more crystallinity loss. As expected, H<sub>3</sub>PO<sub>4</sub> treatment did not affect the crystal structure so much for being the weakest acid of all. Peak intensities decreased slightly and no other extra peaks for any phosphate compounds were detected in the pattern.

Figure 2 displays the FTIR spectra of the representative acid-treated zeolites. The strong band at 1060 cm<sup>-1</sup> is responsible for framework stretching vibration in T (Si or Al)-O-Si units. As seen from the Figure the position of the band shifted from 1065 cm<sup>-1</sup> to

1088 cm<sup>-1</sup> with increasing the Si/Al ratio from 4.04 (for NCW) to 10.8 (for C10-6h). The O-T-O pseudo-lattice vibrations of free TO<sub>4</sub> tetrahedra, O-T-O framework vibrations and the vibrations of hydroxyl in the extra framework of Si-OH and Si-OH-Al groups were estimated by calculating the area under the peaks among the frequencies 570-680 cm<sup>-1</sup>, 850-1600 cm<sup>-1</sup> and 3101-3940 cm<sup>-1</sup>, respectively.

The nitrogen adsorption isotherm data were evaluated to understand the effect of acid type on the textural properties of the zeolites by using the t-plot and Langmuir and Dubinin-Astakhov (D-A) methods and the results were presented in Table 2. From the properties given in the Table, it was understood that the acid treatment caused a noticeable increase in the specific surface area ( $A_L$ ), total ( $V_{max}$ ) and micropore volumes ( $V_{mic}$ ) with respect to the untreated one. However, the nature of the acid used has a different effect on the texture of the zeolite since the ligands cause to form the complexes on the zeolite surface. Surface central atom T (Al or Si) on the zeolite is the center to form an outer-sphere complex on the protonated zeolite surface (T-OH<sup>2+</sup>) with the ligands (L<sup>n-</sup>) (12, 13).

**Table 1.** Cations content of the zeolites, (wt %.).

Cations	NCW	S1	S2	C1-6h	C3- 6h	C5-6h	C10-6h	C3- 3h	C10-3h	N1	N2	N5	P1
Al	15.9	14	13.8	13.9	11	9.4	7.8	12.6	9.4	12.7	12.6	11.9	14
Ca	2.9	0.3	0.1	0.3	1.5	0.02	1.2	1.6	1.1	0.1	1.8	0.05	2.5
Fe	2.5	0.6	0.5	1.2	2.7	0.9	2.4	2.9	2.9	0.8	1.8	0.9	3.1
K	9.9	8.8	8.8	9.3	1.8	8.2	1.4	1.9	1.3	8.5	2.8	8.4	6.0
Mg	1.4	0.7	0.7	0.8	1.5	0.5	1.5	1.9	1.7	0.7	1.7	0.7	2.0
Na	3.2	2	2.1	1.5	1.4	1.9	1.5	1.7	1.4	2.1	1.4	1.9	1.8
Si	64.2	73.6	73.9	73	80	79	84	76.6	82	75.1	78.4	76.1	70.2
Si/Al	4.04	5.25	5.35	5.25	7.3	8.4	10.8	6.08	8.7	5.91	6.18	6.39	5.01

**Table 2.** Nitrogen adsorption characteristics of original (NCW) and acid treated zeolites

	NCW	C1-6h	C3-6h	C5-6h	C10-6h	C3-3h	C10-3h	S1	S2	N1	N2	N5	P1
Si/Al	4.04	5.25	7.3	8.4	10.8	6.08	8.7	5.25	5.35	5.91	6.18	6.39	5.01
$A_L^a$	19	93	203	213	173	182	179	171	202	202	226	180	118
$V_{mic}^b$	0.005	0.029	0.064	0.063	0.047	0.056	0.047	0.048	0.055	0.062	0.068	0.049	0.04
$V_{lim}^c$	0.01	0.036	0.072	0.078	0.059	0.064	0.073	0.060	0.079	0.082	0.077	0.072	0.043
$A_{Ext}^b$	3	6	15	29	29	17	33	25	34	20	23	29	7
$n^c$	1.00	1.60	1.76	1.61	2.38	2.26	1.02	1.61	1.03	1.12	2.63	1.00	1.88
$E^c$	11	19	28	22	22	21	23	29	27	35	25	27	25
$V_{max}^d$	0.013	0.04	0.078	0.089	0.073	0.072	0.079	0.073	0.086	0.086	0.09	0.078	0.05

a  $A_L$ : Langmuir surface area ( $m^2/g$ )

b  $V_{mic}$  and  $A_{Ext}$  are micropore volume ( $cm^3/g$ ) and external surface area ( $m^2/g$ ) respectively, from t-plot.

c  $V_{lim}$ , Limiting micropore volume ( $cm^3/g$ ),  $n$ , exponential constant, and  $E$ , Characteristic Energy ( $kJ/mol$ ), from Dubinin – Astakhov ( $P/P_0 = 0.0001-0.1$ ).

d  $V_{max}$ : Maximum amount adsorbed at a relative pressure ( $P/P_0$ ) of 0.89.

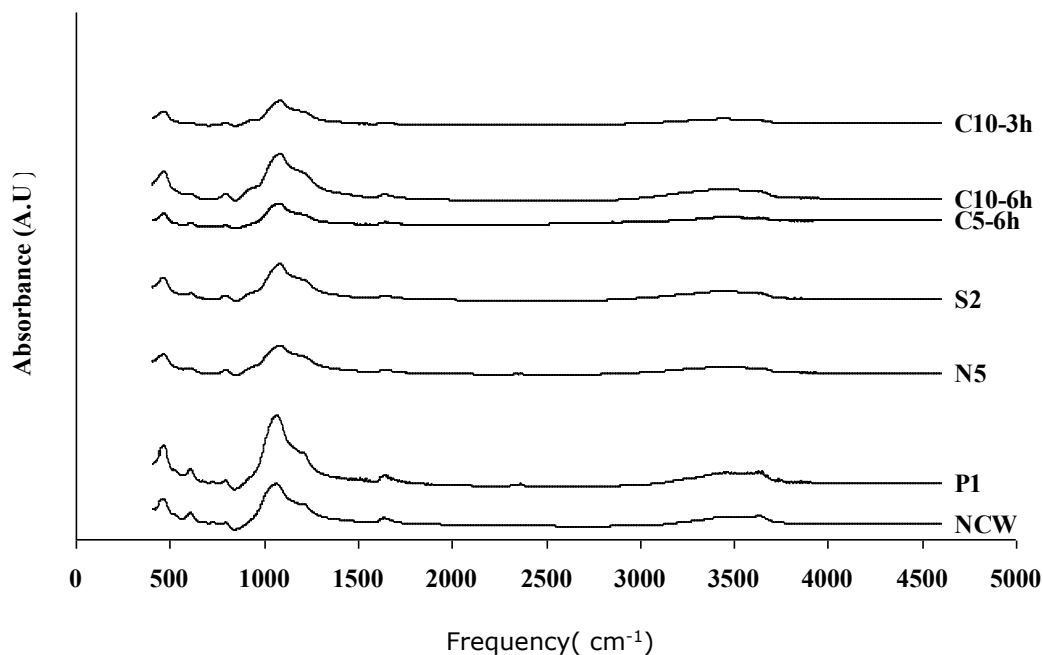
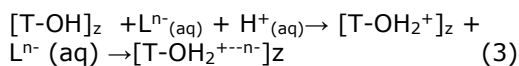
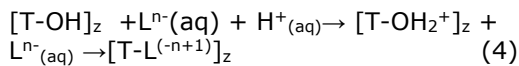


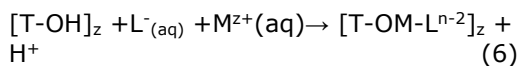
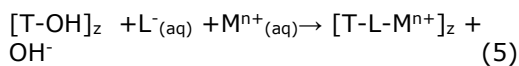
**Figure 2.** FTIR spectrum of untreated (NCW) and acid treated zeolites.



HCl and HNO<sub>3</sub> acids can cause surface precipitation by adsorbing on the external surface to form an outer-sphere complex that involves ion exchange reaction (4). The inner-sphere complexes on the protonated sites can also occur



Readsorption of the dissolved cation (M<sup>n+</sup>) in the solution covalently bonded to the surface to form an inner-sphere complex. However, this kind of complex occurred with the extensive ion-pairing ligand such as SO<sub>4</sub><sup>2-</sup> with the multivalent cation



The zeolites treated with bi- and tri-protic acids such as H<sub>2</sub>SO<sub>4</sub> and H<sub>3</sub>PO<sub>4</sub> have smaller microporous volumes when compared with the treated with mono-protic acids such as HCl and HNO<sub>3</sub>. With acid treatments, the maximum nitrogen adsorption capacity, V<sub>max</sub> of natural zeolite increases in a way similar to the pore volumes and area. The micropore volumes are obtained from the t-plot method (V<sub>mic</sub>) and the Dubinin-Astakhov method (V<sub>lim</sub>). A change in the V<sub>lim</sub> values has the same trend as in the V<sub>mic</sub> values but are higher. For

the HCl and HNO<sub>3</sub> treated zeolites both micropore volume increases markedly with increase in the Si/Al ratio and then decrease with further increase in the concentration of the acid. The reduction in micropore volume due to structural degradation of the zeolite crystals and the complexes (Eq.4 and Eq.5) formation hardly occurs but does for only HCl and HNO<sub>3</sub> acid treatment. In the case of NCW zeolite, the volume of pores accessible to nitrogen is only 0.005 cm<sup>3</sup>/g, thus indicating that most of the pores are blocked by the cations as an impurity. In HCl treatment, as the acid concentrations increased, the micropore volumes of the zeolites increased up to 0.064 cm<sup>3</sup>/g for 3 M HCl but decreased with the further increase in the acid concentrations. The external surface areas of the HCl treated zeolites increased gradually with increasing the Si/Al ratio and reached a maximum of 33 m<sup>2</sup>/g at 10 M HCl treatment. Similar behavior was observed for other protic acid HNO<sub>3</sub> treated samples. On the other hands, the most effective acid was H<sub>2</sub>SO<sub>4</sub> on the developing external surface even the extracted aluminum atoms were not so high as HNO<sub>3</sub> and HCl treatment. This can be explained with the formation of inner-sphere complexes caused to more increase in the external surface areas (Eq.6 and Eq.7). H<sub>3</sub>PO<sub>4</sub> treatment increased the Si/Al ratio as well but not so much as other acids. However, it is very effective in developing the micropore structure without destruction of the crystal structure.

The parameter E, adsorption characteristic energy, calculated from the Dubinin-Astakhov equation is very low for original NCW zeolite with respect to acid treated forms. The

formation of new pores accessible for nitrogen causes to increase the E values which is closely related to adsorbate-adsorbent interaction (14). According to Suzuki (15), the parameter  $n$  in the D-A equation may originally be considered to have integer values of 1, 2 and 3 corresponding to adsorption on the surface, in the micropores and ultra-micropores respectively. In the present study, its value is 1 for untreated natural zeolite, NCW and achieves the value up to about 2 for acid treated zeolites.

HCl, HNO<sub>3</sub>, H<sub>2</sub>SO<sub>4</sub>, and H<sub>3</sub>PO<sub>4</sub> acids were used in the acid treatment to improve the textural properties of the natural zeolite. The cations that occupy the considerable space in micropores of zeolites and structural aluminum were removed during the treatment. Nitrogen was able to diffuse more easily and adsorb more densely in the cavities of the acid treated zeolite. H<sub>3</sub>PO<sub>4</sub> treatment did not destroy the framework of the zeolite structure and improved the microporosity. In the case of the HCl and HNO<sub>3</sub> treatment, the micropore structure of the zeolites was improved. However, a decrease in microporosity was observed in HCl and HNO<sub>3</sub> concentrations higher than 3M.

#### ACKNOWLEDGMENTS

This study was orally presented in 13. National Chemical Engineering conference (UKMK2018) was supported by Izmir Institute of Technology ( project #2000 MÜH02).

#### REFERENCES

1. Tsitsishvili G. Natural zeolites. Ellis Horwood Limited; 1992.
2. Breck D. Zeolite molecular sieves. New York: John Wiley & Sons; 1974.
3. Gola A, Rebours B, Milazzo E, Lynch J, Benazzi E, Lacombe S, et al. Effect of leaching agent in the dealumination of stabilized Y zeolites. *Microporous and Mesoporous Materials*. 2000 Nov;40(1-3):73-83.
4. Giudici R, Kouwenhoven HW, Prins R. Comparison of nitric and oxalic acid in the dealumination of mordenite. *Applied Catalysis A: General*. 2000 Sep;203(1):101-10.
5. Kawai T, Tsutsumi K. [No title found].
6. Notario JS, Garcia JE, Caceres JM, Arteaga IJ, Gonzalez MM. Characterization of natural phillipsite modified with orthophosphoric acid. *Applied Clay Science*. 1995 Oct;10(3):209-17.
7. Aguilar-Armenta G, Díaz-Jiménez L. Characterization of the porous structure of two naturally occurring materials through N<sub>2</sub>-adsorption (77 K) and gas chromatographic methods. *Colloids and Surfaces A: Physicochemical and Engineering Aspects*. 2001 Jan;176(2-3):245-52.
8. Hernández MA, Rojas F, Lara VH. [No title found]. *Journal of Porous Materials*. 2000;7(4):443-54.
9. Cakicioglu-Ozkan F, Ulku S. The effect of HCl treatment on water vapor adsorption characteristics of clinoptilolite rich natural zeolite. *Microporous and Mesoporous Materials*. 2005 Jan;77(1):47-53.
10. Cakicioglu-Ozkan F, Ulku S. Adsorption Characteristics of Lead-, Barium- and Hydrogen-Rich Clinoptilolite Mineral. *Adsorption Science & Technology*. 2003 May;21(4):309-17.
11. Polatoglu I, Cakicioglu-Ozkan F. Aqueous interactions of zeolitic material in acidic and basic solutions. *Microporous and Mesoporous Materials*. 2010 Jul;132(1-2):219-25.
12. Doula MK, Ioannou A. The effect of electrolyte anion on Cu adsorption-desorption by clinoptilolite. *Microporous and Mesoporous Materials*. 2003 Mar;58(2):115-30.
13. Inglezakis VJ, Zorpas AA, Loizidou MD, Grigoropoulou HP. Simultaneous removal of metals Cu<sup>2+</sup>, Fe<sup>3+</sup> and Cr<sup>3+</sup> with anions SO<sub>4</sub><sup>2-</sup> and HPO<sub>4</sub><sup>2-</sup> using clinoptilolite. *Microporous and Mesoporous Materials*. 2003 Jul;61(1-3):167-71.
14. Becer M. Adsorption in volumetric system [Master of Science Thesis]. [İzmir]: İzmir Institute of Technology; 2003.
15. Suzuki M. Adsorption engineering. Tokyo : Amsterdam ; New York: Kodansha ; Elsevier; 1990. 295 p. (Chemical engineering monographs).



## Extractive demetallization of Iraqi crude oil by using zeolite A

Luma H. Mahmood<sup>a</sup>  , Mohammad F. Abid<sup>\*b</sup>  

<sup>a</sup>Department of Chemical Engineering, University of Technology, Baghdad

<sup>b</sup>Department of Medical Instrumentation, Al-Hikma University College, Baghdad

**Abstract:** The feasibility of the removal of vanadium(V) from Iraqi crude oil using zeolite A was investigated. Different operating parameters such as adsorbent loading, vanadium loading, and operating time were studied for their effects on metal removal efficiency. Experimental results of adsorption test show that Langmuir isotherm predicts well the experimental data and the maximum zeolite A uptake of V was 30 mg/g. XRD and EDX analyses revealed the noticeable uptake of zeolite for V. In crude oil, experimental results indicated that for zeolite loading at 1 g/100 mL oil and within approximately 5 h, the removal efficiencies of V were 60, 45, and 33% at vanadium loadings of 75, 85, and 95 ppm respectively. While at 10, 20, 40, and 50 h the removal efficiency was 68, 75, 78 and 78% for 75 ppm of V loading. The equilibrium concentration of V in crude oil was attained after 40 h of operation. Long-term tests revealed the high stability of zeolite A for vanadium removal. Results depict that zeolite A could be advantageous for removal of V in the crude oil hydrotreating units.

**Keywords:** Vanadium, crude oil, demetallization, isotherm models.

**Submitted:** September 14, 2018. **Accepted:** July 08, 2019.

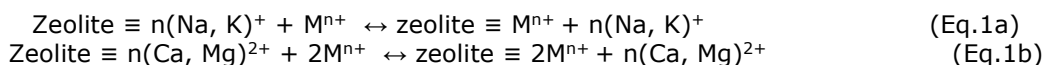
**Cite this:** Mahmood L, Abid M. Extractive demetallization of Iraqi crude oil by using zeolite A. JOTCSB. 2019;2(2):75-86.

**\*Corresponding author. E-mail:** [80005@uotechnology.edu.iq](mailto:80005@uotechnology.edu.iq).

### INTRODUCTION

In crude oil, traces of vanadium are considered the most plentiful metal (1). Serious problems can be evolved due to this metal through petroleum processing, such as catalyst poisoning which leads to reducing sulfur removal from petroleum fractions and consequently to acid rain due to increase emissions of sulfur oxides to the environment, corrosion of equipment and low quality of the product. It is well known that metals in crude oils form complexes with asphaltenes (2). Consequently, high temperature and pressure have been applied for removing metals from crude oil in conventional technologies, including deasphalting, hydrocracking, and hydrotreating (3). Other removal processes are adsorption, acid attack, and solvent extraction (4-6). Therefore an efficient and effective-cost process is required to decrease the concentration of these metals before any

subsequent processes. Zeolites have been utilized in many industrial implementations such as water softening, heterogeneous catalysis, separation, environmental remediation because zeolites possessing large surface area, remarkable catalytic and ionic exchange properties (7-8) and then it could be employed for the removal of these metal ions from crude oil. Zeolites are naturally occurring crystalline aluminosilicate minerals which are synthesized of 3-dimensional structures of tetrahedral molecules connected with the O<sub>2</sub> participated atoms (9). Zeolites are assured ion exchangers and have been effectively utilized in the elimination of heavy metals from wastewaters and a catalyst for the catalytic cracking of heavy oils (10-11). Benhammou *et al.* (12) reported that ion exchange reaction takes place between exchangeable cations (Na<sup>+</sup>, K<sup>+</sup>, Ca<sup>2+</sup>, and Mg<sup>2+</sup>) located in zeolite structure and cations (M<sup>n+</sup>) in solution and can be given by Eqns. 1a and 1b:



During the ion exchange process, metal ions have to move through the pores and channels of zeolite and they have to replace exchangeable cations ( $\text{Na}^+$ ,  $\text{K}^+$ ,  $\text{Ca}^{2+}$ , and  $\text{Mg}^{2+}$ ). Thus the cation exchange capacity of a zeolite is a result of the degree of substitution of Al for Si in the framework. Thus the greater the degree of substitution of Al for Si, the greater the number of cations required to maintain electronic neutrality in the zeolites. These charge balancing cations are capable of exchanging with external cations from solution (13). Price *et al.* (14) conducted an experimental study to investigate the adjustments in framework occurred after partly substituting the extra-framework  $\text{Na}^+$  ions with monovalent,  $\text{Li}^+$ ,  $\text{K}^+$ ,  $\text{Rb}^+$  and  $\text{NH}_4^+$  and divalent,  $\text{Ca}^{2+}$  cations. The authors concluded that solid-state Nuclear Magnetic Resonance detected alterations to the internal structure of the Linde Type A framework upon ion substitution with  $\text{NH}_4^+$  and  $\text{Ca}^{2+}$ . Substitution with  $\text{Li}^+$ ,  $\text{K}^+$  and  $\text{Rb}^+$  ions does not considerably influence the long-range crystal order. Substitution with  $\text{NH}_4^+$  ions compensates some of the long-range order of the zeolite A crystals because of the wasting of some structure Al as can be observed from X-ray data.

Substitution with divalent  $\text{Ca}^{2+}$  ions inserts some monodentate carbonate kinds into the structure, but no change to the long-range crystal order is noticed. Published data on the usage of zeolites for the elimination of metal ions from crude oil are scarce. In Iraq, crude oil of east Baghdad field contains higher amounts of vanadium ( $> 75$  ppm) than other heavy metals (15). The main objective of present work was to investigate the feasibility of Zeolite type A to remove vanadium ions from crude oil. Another objective was to study the kinetics of the adsorption process.

## MATERIALS AND METHODS

### Materials

Zeolite A ( $\text{Na}_{12}(\text{AlO}_2)_{12}(\text{SiO}_2)_{12} \times 27\text{H}_2\text{O}$ ) was purchased from GCMIL, India. Crude oil was received from Al-Daura Oil Refinery, Baghdad. Vanadium tetrachloride ( $\text{VCl}_4$ ), EDTA, HCl, and NaOH flakes were supplied from Ava Chemicals Private Limited, India. Table 1 lists the physicochemical properties of crude oil of east Baghdad field.

**Table 1:** Physicochemical properties of crude oil of eastern Baghdad field (15)

Item	Property	Value
1	Density @ 15 °C $\text{g}/\text{cm}^3$	0.932
2	Sulfur content %wt	75.970
3	Vanadium, ppm	25.340
4	Nickel, ppm	2.684
5	Asphaltenes %wt x	6.412

### Experimental method

The experimental setup is shown in Figure 1. Zeolite A particles were ground. 1 gram of the sieved zeolite A was added into 100 mL of the crude oil in a separating flask with 5 mL of EDTA solution. This mixture was mixed well by a magnetic stirrer at 100 rpm for an hour at room temperature ( $\sim 25$  °C). Zeolite A was separated from the mixture in a vacuum separator (Rocker 300A Vacuum Filtration System, New Star Environmental & Laboratory Products). The liquid mixture was then transferred to a high-speed centrifuge (Type Centrisart® D-16C, Sartorius Co.) where the demetallized crude oil (DMCO) layer was separated and analyzed for the metal ions. According to the published data (16-18), the best pH range of adsorption of heavy metals onto zeolite has been varied between 3 and 6. In the present study, the selected pH was  $\sim 4.5$ , adjusted using NaOH and HCl.

### Kinetic study of adsorption

The amount of vanadium adsorbed at equilibrium, (mg/g) was estimated using Eq. 2.

$$q_e = \frac{(C_o - C_e)V}{W} \quad (\text{Eq. 2})$$

Where  $C_o$  and  $C_e$  are concentrations of vanadium at initial and at equilibrium (mg/L), respectively,  $V$ : volume of the heavy oil used,  $q_e$ : concentration of V at equilibrium (mg  $\text{L}^{-1}$ ), and  $W$ : the mass of zeolite A used (g). The Freundlich and Langmuir equations are the most widely used models for isotherm (16), the correlation of Langmuir and Freundlich isotherms are represented by Eqns. 3 and 4, respectively.

$$q_e = \frac{q_m \cdot K_L \cdot C_e}{(1 + K_L \cdot C_e)} \quad (\text{Eq. 3})$$

$$q_e = K_F \cdot C_e^{1/n} \quad (\text{Eq. 4})$$

Where  $q_m$ : maximum quantity of metal V adsorbed per unit mass of zeolite (mg  $\text{g}^{-1}$ ),  $K_L$  is the Langmuir constant (L  $\text{mg}^{-1}$ ) and  $K_F$  is Freundlich

constant ( $\text{mg gm}^{-1}$ ) ( $\text{L mg}^{-1}$ )<sup>-n</sup>. To predict which one of these two models will well represent the experimental data of metal(V) removal, a linearization technique would be applied on equations 3 and 4, respectively. Equation 5 represents the linear form of equation 3, and equation 6 represents the linear form of equation 4.

$$\frac{1}{q_e} = \frac{1}{q_m} + \frac{1}{q_m K_L C_e} \quad (\text{Eq.5})$$

$$\ln q_e = \ln K_F + \frac{\ln C_e}{n} \quad (\text{Eq.6})$$

### Analysis techniques

XRD-6000 Shimadzu X-ray diffractometer (with an incident angle of 0.154 nm using Cu-K $\alpha$  radiation) was used to examine the phase ingredients. The topographical features were accomplished by utilizing Tescan VEGA 3SB scanning electron

microscope with accelerating voltage: 200 V to 30 kV and the magnification power from 4X to 10<sup>5</sup>X. The chemical composition of zeolite A was anatomized by utilizing energy dispersive X-ray analysis (EDX) Model; Inspect S50/FEI Company, Netherland. The concentration of vanadium in fluid before and after treatment was measured with a model AA-7000 Flame atomic absorption spectrometer (FAAS) with graphite technique, Shimadzu with flame of N<sub>2</sub>O-C<sub>2</sub>H<sub>2</sub> and the instrument settings were according to the manufacturer's recommendations (Lighting conditions: Current; 10 mA/0 mA. Wavelength; 318.4 nm. Slit width; 0.5 nm. Lighting mode; BGC-D2). Measurements of vanadium's concentration were conducted at the Petroleum Research and Development Center, Iraqi Ministry of Oil, Baghdad. pH measurements were performed using an on-line pH meter Model Excel 25PH/mV/ISL.

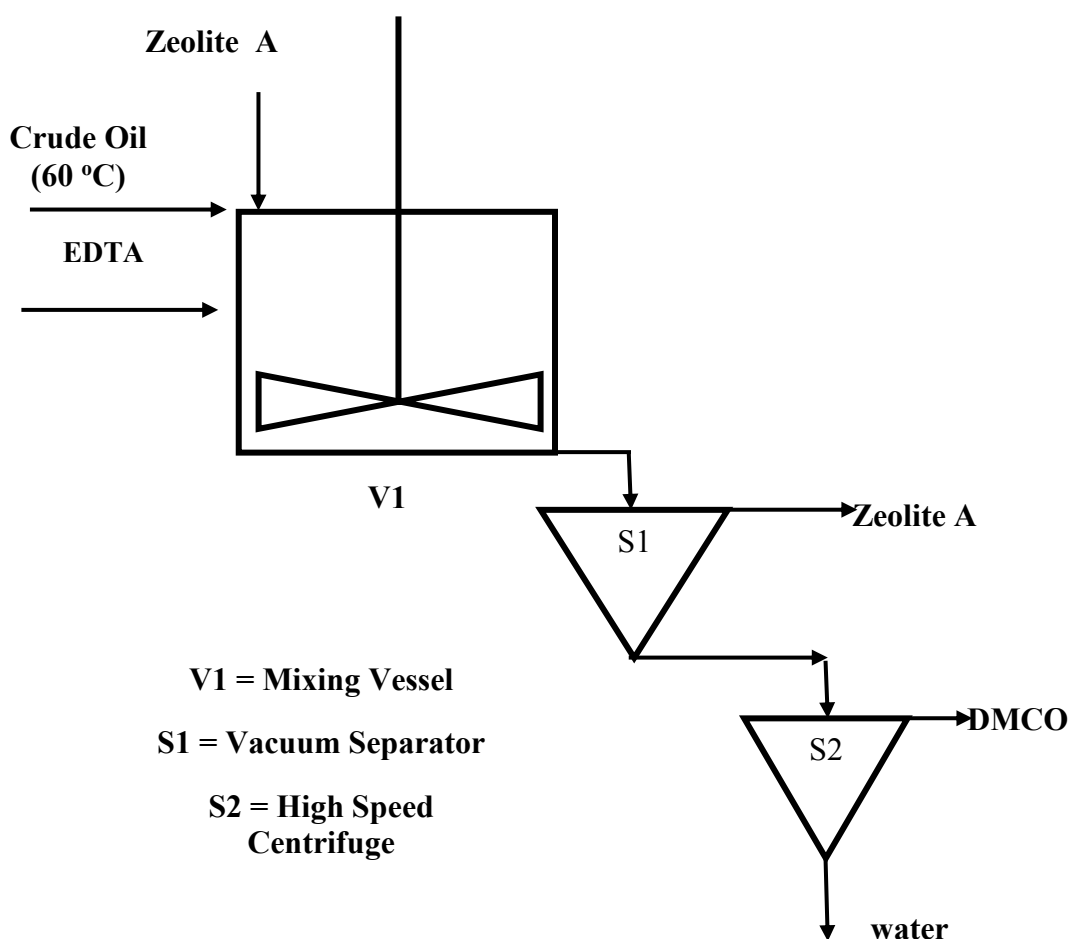


**Figure 1:** Schematic of the experimental setup.

RESULTS AND DISCUSSION

Results for Kinetic study

The maximum adsorption capacity of zeolite A was estimated by conducting adsorption experiments. Different concentrations (5, 10, 20, 30, and 50 mg/L) of  $VCl_4$  in distilled water were prepared. Then 100 mL of each concentration is placed in a 250 mL

flask separately with 1 g of zeolite A. Figure 2 plots the experimental results of vanadium adsorption at equilibrium on zeolite A. Figure 2 depicts that the maximum uptake of V metal was  $\approx 30 \text{ mg g}^{-1}$ , this may be attributed to the capability of the zeolite framework which having a high percentage of pores.

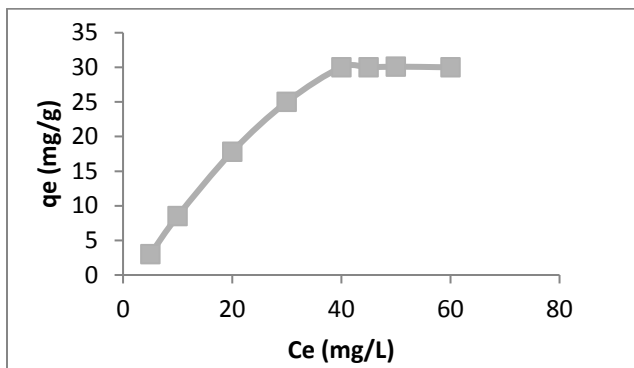


Figure 2: Experimental results of vanadium adsorption at equilibrium over Zeolite A.

Figure (3a) represents a plot of  $\frac{1}{q_e}$  versus  $\frac{1}{C_e}$  with a correlation coefficient ( $R^2$ ) = 0.9738. Meanwhile, Fig. (3b) represents a plot of  $\ln q_e$  versus  $\ln C_e$  with a correlation coefficient ( $R^2$ ) = 0.9711. The linear equations are

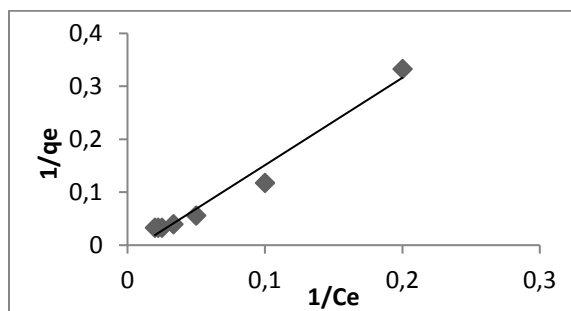
$$\frac{1}{q_e} = 1.6505 \frac{1}{C_e} - 0.0139 \quad (6)$$

for Langmuir isotherm, and

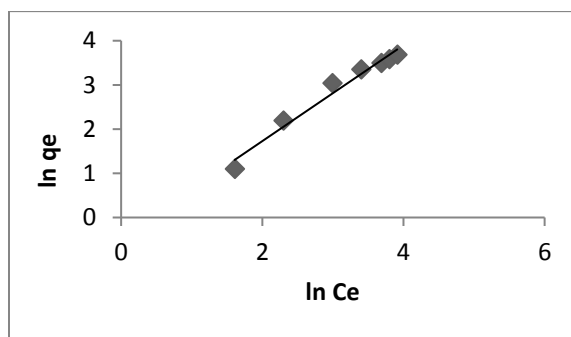
$$\ln q_e = 1.0848 \ln C_e - 0.4412 \quad (7)$$

for Freundlich isotherm.

These results assure the applicability of Langmuir isotherm in our study.



(3a)



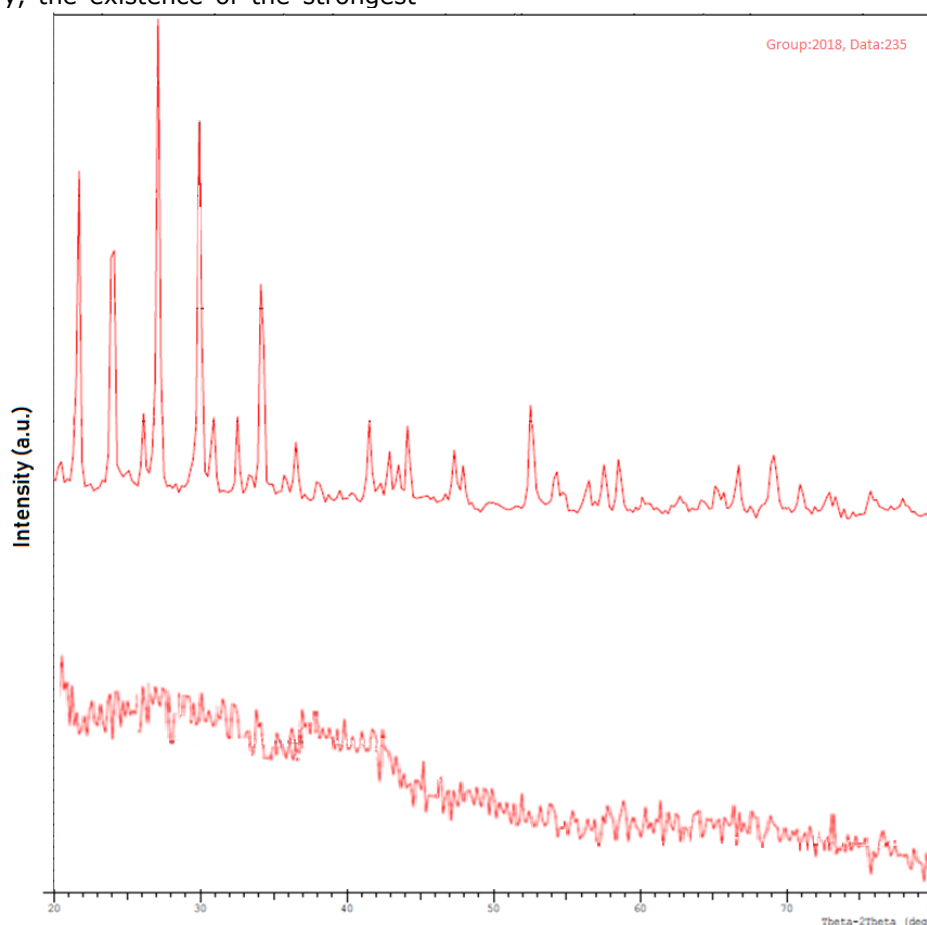
(3b)

Figure 3: Linearization plots of Langmuir isotherm model (3a) and Freundlich isotherm model (3b) for vanadium adsorption on Zeolite A.

**Influence of metal adsorption on zeolite characteristics**

*XRD analysis:* Figure 5 shows XRD images of zeolite A before and after vanadium adsorption. According to (19), the upper XRD pattern in Figure 5 shows an excellent match with typical zeolite A. As can be seen in Figure 5 (upper image), there are 3 strongest peaks, followed by another 2 weaker peaks. The position of the five peaks can be summarized in Figure 5 (upper), and its details can be seen in Table 2. In Table 2, the strongest 3 peaks were found at  $2\theta$  of  $29.550^\circ$ ,  $27.9583^\circ$ , and  $21.385^\circ$ , where the ratio of  $I/I_0$  were 95, 49, and 38 respectively. The other 2 peaks were shown at  $2\theta$  of  $24.211^\circ$  and  $34.440^\circ$ . The ratio of  $I/I_0$  were 38 and 27, respectively. According to ICDD 47-1870 data library, the existence of the strongest

peaks may indicate that the mineral was appropriate with sodium aluminum silicate hydrate of clinoptilolite-Na. Meanwhile, the lower XRD image of Figure 5 shows a breakdown of structure which indicates an effective exchanger (zeolite A). This collapsing in peaks may be attributed to the replacement of Si ions by larger vanadium ions which could induce an extension in the unit cell. This attitude is compatible with the existence of vanadium in the structure of zeolite which caused by the difference between V-O and Si-O ligament tallness (20). Gallezot and Leclerc (21) found that vanadium promotes the collapse of the zeolite framework because it joins with other ions which stabilize the framework of the zeolite.



**Figure 4:** XRD images of zeolite A before vanadium uptake (upper) and after vanadium uptake (lower).

**Table 2:** Details of peaks in XRD of zeolite A (before vanadium adsorption).

Peaks	$2\theta^\circ$	Intensity (counts)
1	21.385	1600
2	24.211	1250
3	27.493	2550
4	29.554	1750
5	34.440	1100

*SEM analysis:* Figure 5a and Figure 5b show the SEM image of zeolite A at 200 nm before and after vanadium ions uptake respectively. As can be seen in Fig. 6b that the particles be dissimilar in

dimensions after the exchange, which revealed that the vanadium ion uptake had a significant effect on the structural framework of zeolite A.

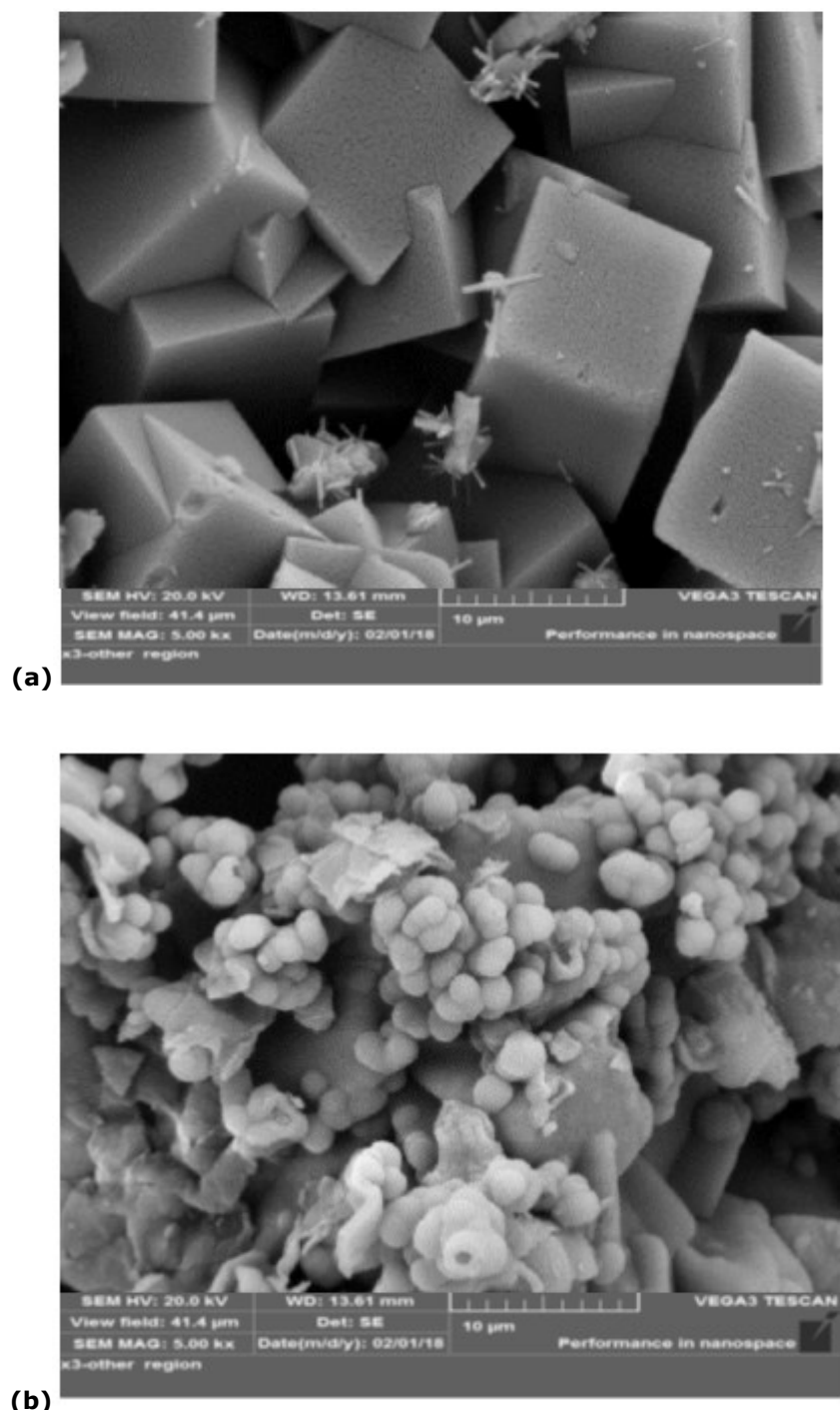


**Fig.5** SEM images before vanadium adsorption (a) and after adsorption (b).

*EDX analysis:* EDX analysis of the zeolites was carried out, before and after vanadium uptake, to estimate the percentage weight of elements existed. Moreover, the proportion of Si/Al in the zeolites can be determined. Table 3 presents the

percentage weight of elements as measured by the SEM-EDX (XRD-6000 Shimadzu) and the proportion of Si/Al in the zeolites. Figure 6(a-b) shows EDX images of zeolite A before and after vanadium uptake. As can be seen from images, that all Na

and some of Al and Si are ion exchanged with vanadium on the zeolite surface. The percentage weight of elements displays that the whole  $\text{Na}^+$  inside the zeolite were substituted and furthermore, about 76% of ions of silicon which formed the structure were also replaced by the ions of vanadium while only 26% of Al ions were exchanged. (Gomes et al. (22) stated that ion radius plays an important effect on the ionic exchange. Shannon (23) published a revised

crystallographic data on ionic radii. He estimated the effective ionic radii of  $\text{Na}^+$ ,  $\text{Al}^{3+}$ ,  $\text{Si}^{4+}$ , and  $\text{V}^{4+}$  as equal to 102, 48, 40, and 35.5 picometers, respectively (see also [www.abulafia.mt.ic.ac.uk/shannon](http://www.abulafia.mt.ic.ac.uk/shannon)). These values suggest that vanadium ions could exchange any ions of equal or larger of its size which clearly explains the drastic effect of Na and Si ions exchanged with the framework and breakdown of zeolite structure noticed after vanadium uptake.

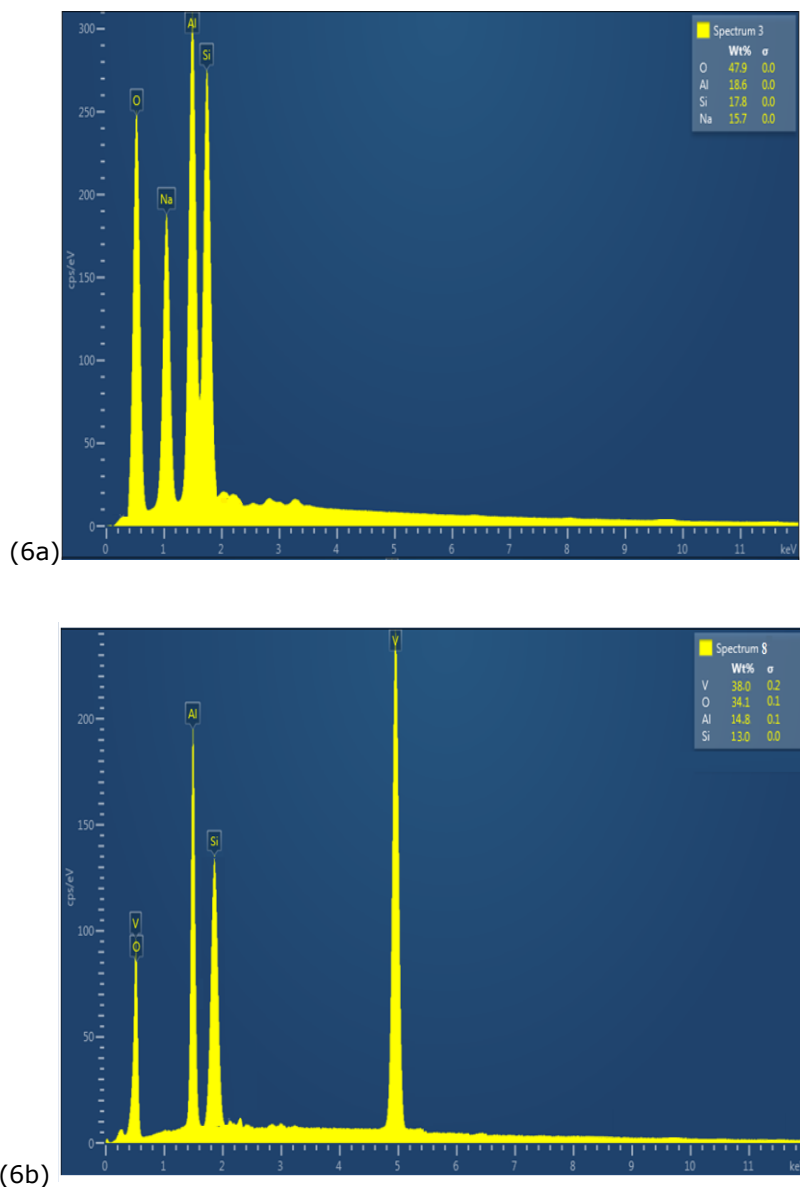


**Fig. 6:** EDX images of zeolite A before vanadium uptake (6a) and after vanadium uptake (6b).

**Table 2.** Percentage weight of elements before and after vanadium uptake.

	O	Na	Al	Si	Si/Al	V
%weight	Before/after	Before/after	Before/after	Before/after	Before/after	Before/after
	47.9 / 38.2	15.7 / 0.0	18.6 / 14.8	17.8 / 13.0	1.045 / 1.138	0.0 / 38.2

**Removal of vanadium from crude oil**

A series of experiments was conducted to test the capability of zeolite to remove vanadium ions from crude oil. Figure 7 illustrates vanadium removal efficiency as a function of operating time at different loading of vanadium. As can be seen in Figure 7, a remarkable increase in vanadium removal within a short time was observed for all loadings of vanadium after then a slight increase with operating time was shown. Within approximately 5 h, the vanadium removal efficiencies were 33, 45, and 60% at vanadium loadings of 75, 85, and 95 ppm respectively. Further processing of crude oil with 75 ppm vanadium shows a continuous slight increase in metal removal with operating time. At 10, 20, 40, and 50 h the removal efficiency was 68, 75, 78 and 78%. As can be seen, an equilibrium concentration of the vanadium was attained after 40 h. For other vanadium loadings (i.e., 85 and 95 ppm), the equilibrium concentration of vanadium was attained at approximately 20 h. Salman et al. (16)

reported that the differences in zeolite adsorption capacities for heavy metal ions can be attributed to different factors i.e. physicochemical factors, hydration energy, and diameter. In general, zeolites and ion exchanges prefer high valent ions (24). Thus high selectivity of zeolite for vanadium was due to electrostatic attraction between high valent vanadium cations and cations of the solid adsorbent. Figure 8 plots the effect of zeolite loading (g /100 mL oil) on vanadium removal (%). As can be seen in this Figure, zeolite loading has a positive impact on removal efficiency. The increase in vanadium removal with the zeolite A loading is due to the higher number of active sites available over the adsorbent (25). It is interesting to note that at higher loading of zeolite a constant value of vanadium removal was attained. This may be attributed to that equilibrium is established between the adsorbed ions of vanadium onto zeolite and that which still existed into the treated crude oil.

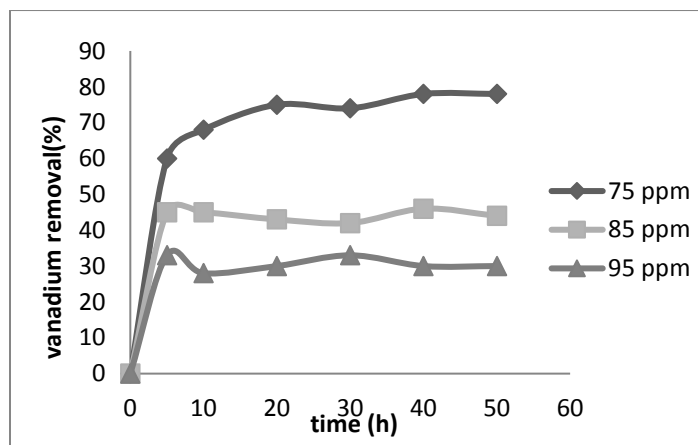


**Figure 7:** Vanadium removal efficiency from crude oil as a function of operating time at zeolite loading 1 g/100 mL oil.

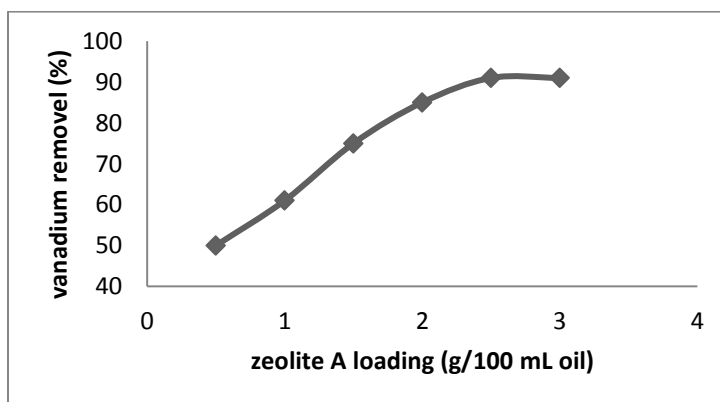


**Figure 8:** Vanadium removal (%) as a function of zeolite A loading (g/100ml oil) at vanadium loading = 75 ppm and operating time=5 h

**CONCLUSION**

In the present work, different operating parameters such as vanadium loading, zeolite type A loading, and operating time were investigated for their effects on vanadium removal efficiency from crude oil. Results revealed that zeolite loading and operating time have a positive impact on removal efficiency while vanadium loading showed a different trend. Experimental results of adsorption test show that Langmuir isotherm predicts well the experimental data. RDX and EDX analyses confirm the high tendency of zeolite A to remove vanadium ions from crude oil. Long- term tests revealed the high stability of zeolite A for vanadium removal.

**ACKNOWLEDGEMENTS**

Authors are grateful to the Department of Chemical Engineering, the University of Technology for providing space and facilities. Thanks are also due to the Petroleum Research Center, Iraqi Ministry of Oil for their assistance.

**NOMENCLATURE**

$C_o$  : concentrations of vanadium at initial, (mg/ L)  
 $C_e$ : concentrations of vanadium at equilibrium, (mg/ L)  
 $V$ : volume of the heavy oil used, (mL)  
 $W$ : mass of zeolite A used, (g)  
 $q_m$ : maximum quantity of metal V adsorbed per unit mass of zeolite, (mg/ g)  
 $q_e$ : concentration of V at equilibrium, (mg/ L)  
 $K_L$ : Langmuir constant, (L/ mg)  
 $K_F$ : Freundlich constant (mg/ gm) (L/ mg)<sup>-n</sup>

**REFERENCES**

1. Ali, M. F., Abbas, S. A review of methods for the demetallization of residual fuel oils. *Fuel Processing Technology*. 2006; 87(7): 573-84.
2. Gawel, I., Bociaska, D., Biskupski, P. Effects of asphaltenes on hydroprocessing of heavy oils and residua. *Applied catalysis* 2005; 295: 89-94
3. Rana, M. S., Sámano, V., Ancheyta, J., Diaz, J. A. I. A review of recent advances on process technologies for upgrading of heavy oils and residua. *Fuel* 2007; 86(9): 1216-31.
4. Fergusson, J.E. *The Heavy Elements: Chemistry, Environmental Impact and Health Effects*, Pergamon, Oxford (1990).
5. Flores, V., Cabassud, C. A hybrid membrane process for Cu(II) removal from industrial wastewater, comparison with a conventional process system. *Desalination* 1999;126: 101-8.

6. Smith, K.J., Lai, W.C. Heavy oil microfiltration using ceramic monolith membranes. *Fuel* 2001; 80: 1121- 30.
7. Thompson, R. W. *Molecular Sieves, Science and Technology*, Weitkamp, I. J. (Ed). Springer, Berlin (1998).
8. Auerbach, S.M., Carrado, K.A., Dutta, P.K. *Handbook of Zeolite Science and Technology*, Marcel Dekker, New York (2003).
9. Keane, M.A. The removal of copper and nickel from aqueous solution using Y zeolite ion exchangers. *Colloids Surface A: Physicochem. Eng. Aspects* 1998; 138: 11-20.
10. Ding, L., Zheng, Y., Zhang, Z., Ring, Z. and Chen, J. Hydrotreating of light cycled oil using WNi/Al<sub>2</sub>O<sub>3</sub> catalysts containing zeolite beta and/or chemically treated zeolite Y. *Journal of Catalysis* 2006; 241(2): 435-45.
11. Kuzmcki, S. M., McCaffrey, W. C., Brian, J., Wangen, E., Koenig, A., Lin, C. C. H. Natural zeolite bitumen cracking and upgrading. *Microporous and Mesoporous materials* 2007; 105: 268-72.
12. Benhammou A., Yaacoubi A., Nibou L., Tanouti B. Adsorption of metal ions onto Moroccan stevensite: kinetic and isotherm studies. *Journal of Colloid and Interface Science* 2005; 282: 320 - 6.
13. Curkovic L., Cerjan - Stefanovic Š., Filipan T. Metal ion exchange by natural and modified zeolites. *Water Research* 1997; 31(6): 1379 - 82.
14. Price, L., Leung, K.M., Asel, S. Local and Average Structural Changes in Zeolite A upon Ion Exchange. *Magnetochemistry* 2017; 3(4): 42-57.
15. Al-Daura Oil Refinery. Laboratory analyses daily log-sheet, Midland Refineries Company, Baghdad (2017).
16. Salman, H., Shaheen, H., Ghaiath, A., Khalouf, N. Use of Syrian natural zeolite for heavy metals removal from industrial waste water: Factors and mechanism. *Journal of Entomology and Zoology Studies* 2017; 5(4): 452-61.
17. Cozmuta, L.M., Mihaly, A., Peter, A., Nicula, C., Nsimba, E.B., H Tutu, H. The influence of pH on the adsorption of lead by Na-clinoptilolite: Kinetic and equilibrium studies, *Water SA* 2012; 38(2): 269-78.
18. Surinder, S., Lokesh, K. V., Sambhi, S.S., Sharma, S.K. Adsorption Behavior of Ni (II) from Water onto Zeolite X: Kinetics and Equilibrium Studies, *Proceedings of the World Congress on*

Engineering and Computer Science 2008 WCECS 2008, October 22 - 24, 2008, San Francisco, USA.

19. Treacy, M.M.J., Higgins, J.B. Collection of Simulated XRD Powder Patterns for Zeolites. Fourth Revised Edition (2001), Elsevier, Amsterdam.

20. Kim, G. J. Hydrothermal crystallization and secondary synthesis of vanadium containing zeolites, Journal of Korean Association of Crystal Growth 1997; 7(3): 437-48.

21. Gallezot, P., Leclercq, C. Conventional and analytical electron microscopy. In Catalyst Characterization: Physical Techniques for Solid Materials. Edited by Boris Imelik, Jacques C. Vedrine (1994).

22. Gomes, V.A.M., Coelho, J.A., Peixoto, H.R.,

Lucena, S.M.P.: Easily tunable parameterization of a force field for gas adsorption on FAU zeolites. Adsorption 2015; 21: 25-35.

23. Shannon, R.D. Revised effective ionic radii and systematic studies of interatomic distances in halides and chalcogenides. Acta Crystallographica. (1976). A32, 751-67. doi:10.1107/S0567739476001551.

24. Motsi, T., Rowson, N.A., Simmons, M.J. Adsorption of heavy metals from acid mine drainage by natural zeolite. International Journal of Minerals Processing 2001; 92:42-8.

25. Abid, M.F., Hamiedi, S.T., Ibrahim, S.I, Al-Nasri, S.K. Removal of toxic organic compounds from synthetic wastewater by a solar photocatalysis system. Desalination and Water Treatment 2018; 105: 119-25.





## Development of a Low Density (Light) Colorful Gas Ceramic Floor Tile for Outdoor Floor Applications Using Recovered Ceramic Wastes Treatment

Nihan Ercioglu<sup>\*,a</sup>  , Ayşe Gülhan Koyuncu<sup>a</sup>  , Elif Ubay<sup>a</sup>  

\* Department of Chemical Engineering, Faculty of Engineering, Eskisehir Technical University, 26000, Eskisehir, Turkey

<sup>a</sup> Research and Development Center, Seranit Ceramic Factory, 26670, Eskisehir, Turkey

**Submitted:** December 04, 2018. **Accepted:** July 03, 2019.

**Cite this:** Ercioğlu N, Koyuncu A, Ubay E. Development of a Low Density (Light) Colorful Gas Ceramic Floor Tile for Outdoor Floor Applications Using Recovered Ceramic Wastes Treatment. JOTCSB. 2019;2(2):87–96.

\*Corresponding author. E-mail: [nihanercioglu@gmail.com](mailto:nihanercioglu@gmail.com).

**Abstract:** Nowadays, gas ceramics have become an important role part of making lighter and more durable tiles which are used for outdoor floor applications. In addition to this, its commercial potentials are quite high due to the long life of the gas ceramics. In line with this purpose, it is aimed to develop gas ceramic floor tiles for outdoor floor applications which have the advantages such as lightweight, low density, high strength and also being differently colorful. By adding 30-40% of production wastes into the recipes, it is supposed to get into market with new gas ceramic products which have both innovative properties and also to provide wastes recycling. Within the scope of this project, in order to have the desired structural and mechanical properties of the final products, the materials to be used in the recipes have been selected so that the furnace process be optimized. Raw materials such as clay, calcite, pegmatite and silicon carbide were obtained from different mines. Due to the fact that the tiles have been planned to be colorful, so that color pigments to be used were obtained from suppliers. In pretreatment stage the ceramic sludge was prepared then viscosity and density were controlled and prototype samples from furnace were tested and analyzed. In this context, engineering studies were made for pore size distributions /homogeneities, sieve analysis and firing process. This study is unique owing to the fact that new recipes will be tried in the factory. Moreover, this study is a research and development (R&D) project because with the addition of the production wastes in recipes not only will the production wastes be eliminated but also the consumption amount of supplied raw materials will be reduced. In the light of foregoing information about gas ceramic technology, final products will be more economical, have homogeneous structure and high compressive strength compared with other feasible alternatives. Furthermore, presented innovative final products have been planned to be colorful in accordance with raw materials and developed manufacturing methods. These products would be the first example in the ceramic/porcelain floor tiles industry which have been developed on a global scale with the use of wastes as raw materials.

**Keywords:** Waste management, gas ceramic, construction materials, filter press cake.

### INTRODUCTION

Ceramic materials have some properties like fragile, low tensile stresses and impact loads, plastic deformation not like metals and low resistance to sudden mechanical and thermal changes and because of these properties the usage of monolithic ceramics in structural applications are

prevented. The most important disadvantages of ceramics were low fracture toughness (1). Various methods have been developed to increase fracture toughness of ceramic materials. All these methods are based on the creation of mechanisms that allow the dissolution of energy during the fracture by uniformly distributing a second phase in the fragile ceramic matrix. The used secondary phases are as

follows: Ductile materials, materials that provide phase transformation, the development of rhodonite grains in these structures by using in situ methods and to improve reinforcing materials in different forms (continuous fiber, etc.) was provided (2-3).

Silicon carbide (SiC) is a crystalline material that has a very high hardness, high chemical resistivity and thermal conductivity, also is an important semiconductor which has been widely used in extensive range of applications (4). Silicon carbide appears in two different crystalline forms, namely hexagonal  $\alpha$ -silicon carbide, cubic  $\beta$ -silicon carbide and also occurs in several forms as non-fibrous and polycrystalline fibers (5).

There are several studies based on production of gas ceramics. Those studies focused mainly on the effects of compression strength and density of gas ceramic manufacturing. In the study of Suleyman Akpınar et al (6), cordierite-based silicon carbide doped ceramic foam materials production and characterization has been studied. In this study, the measured compression strength values vary in the range of 0,27 - 0,52 MPa. This compression strength values are well below the target value.

When the density values were compared, it was seen that data were obtained between 0.41 and 0.48 g/cm<sup>3</sup>. It is seen that our product, which is planned to be low density, is higher than desired when compared with the values in the range of 0.21-0.41 g / cm<sup>3</sup>. F.A. Costa Oliveira et al (7) calculated the bulk density of the materials obtained from similar studies in the related literature as 0.29 g / cm<sup>3</sup> and the compressive strength was 0.24 MPa. When these data are compared with the data obtained in the studies in the article, obtained values of compressive strength

is 4.5 times and density values are 2 times lower than the literature.

In the literature, it is understood from the research that the amount of solid matter in ceramic slurry has great importance in the studies related to the production of ceramic foam filters. This causes an increase in the cost of the prescription and the energy consumption. Considering these disadvantages, we have worked on the development of a product which is homogenous with the use of 55-60% production waste and with a higher compressive strength and a more economical product compared to the existing alternatives. The colored gas ceramic technology developed in the project is the first example developed on a global scale for the use in outdoor floor applications with the advantage of its lightness and obtaining the desired colors. According to other commercial insulation materials, non-flammability property is one of the important parameters.

## EXPERIMENTAL PROCEDURE

### Materials and Method

This investigation was performed with an industrial spray-dried powder normally used for the production of gas ceramics. Within the scope of this project, the pore forming agent (SiC) was supplied from ESAN Magnesium Company in Turkey. The materials used in recipes albite, clay and calcite were obtained from quarries in Eskisehir. Pegmatite was purchased from Has Ozcelik Mining Company in Bilecik. All composition of raw materials are given in Table 1. Na-Silicate was used as a fluidizer. Since gas ceramic have been planned to be colorful, green, blue and pink pigments which have been selected from the suppliers, were purchased from Torrecid Company in Eskişehir.

**Table 1:** Raw Material Percentages in Colorful Gas Ceramic Recipes.

Component	Content (wt. %)
Production Waste	36
Clay Blend	32
Pegmatite Blend	18
Calcite	2
Albite	12
SiC(Foaming Agent)	0.3
Pigment	5

### Filter Press Production

The total capacity of the wastewater treatment plant in our factory was 1350 m<sup>3</sup>/day. 20 tons of filter press cake was obtained per day. Process waste water comes from the sludge preparation, glaze preparation, filter cake preparation, dimensioning and finishing, decor lines, decor

cutting and glazing process were brought to the equalization tank where they were collected and mixed homogeneously. The collected wastewater was first passed through a coarse screen with a gap of 5 mm and then taken to the sand trap unit. With this grill and sand catcher, materials that are physically hold able in the wastewater and

materials that may damage the equipment in the treatment plant were kept. From here, the wastewater would pass to the balancing pool.

Wastewater from this tank was sent to the coagulation pool which was the first unit of chemical treatment with waste water pumps at a constant flow rate. In this unit, PAC (Poly Aluminum Chloride) inorganic material derivatives were used as a coagulant. After that the waste water was sent to the flocculation tank. The chemical flocculants formed in this unit could easily be turned into large flocculants by using anionic polyelectrolyte as flocculant. Flocculants and coagulants were fed in dosages determined as a result of tests conducted according to the content of incoming waste water. After this stage, the waste water reached the precipitation tank and was separated by gravity precipitation process.

Wastewater in the balancing pool was taken to the coagulation pool by a pump. The coagulant was dosed to the appropriate coagulant (we used PACs). Wastewater passed into the flocculation pool after coagulation pool. The polyelectrolyte was dosed and mixed with the dosing pump in order to enlarge the resulting flocks. Wastewater passed to the sedimentation pool. In here, the flocks formed in the flocculation pool were allowed to settle. The

wastewater was then taken to the neutralization pool. In this pool, acid was added to keep the pH neutral. Sludge particles from the sedimentation tank were collected in the sludge condensation tank. An industrial filter press was a tool used in separation processes, specifically to separate solids and liquids. The sludge at the bottom of the sedimentation pool is transferred to the sludge tank with the sludge pump. Filter presses were utilized in order to separate water from mud to reuse the water. In this unit, the sludge was reduced by compressing the water content and could be removed as solid waste or used as raw material in the plant. The filtrate from the filter press was given to the treatment plant entrance for purification.

The cakes began to form with high flow rate of the filtrate. Cakes were totally formed at the maximum pressure. After that, cakes discharged from filter press. As a result of the filter press system, humidity values of cakes were calculated between 28-32%. The sludge cake formed at the end of the filtration process was loaded from the system to the trailer and the dried sludge was conveyed to the storage area. The water treated in this system was recycled by re-using in the plant. In Figure.1, the waste water treatment is shown the process in our company.

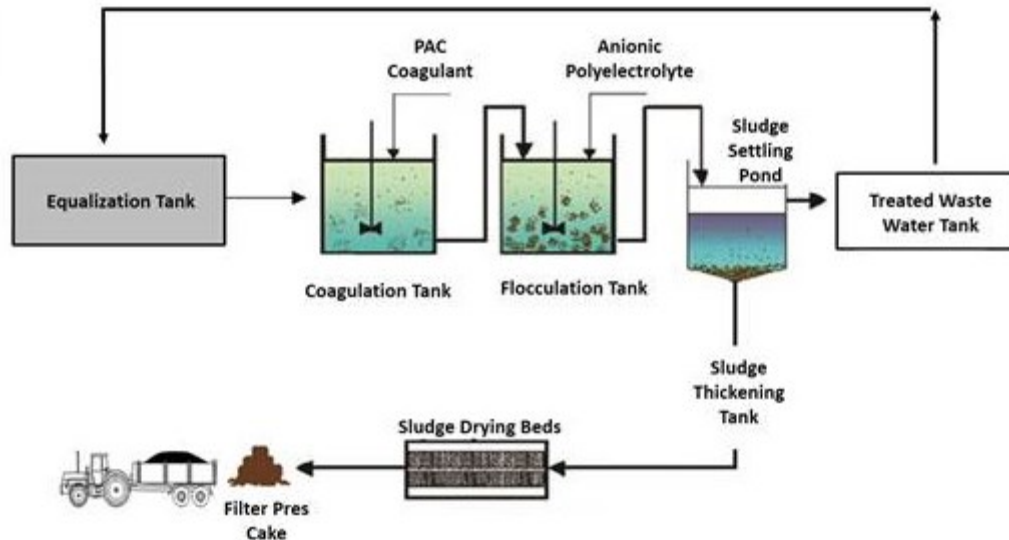


**Figure 1:** Waste Water Treatment Process Overview.

### Gas Ceramic Preparation

In the present study, raw materials and pigments were weighed at 500 g and mixed with 45-46% water. Prepared recipes were milled using ball mills with a capacity of 800 mL. The slurry (ceramic powder and pore-forming agent) was mechanically mixed for 4 hours until uniform distribution was observed. The slurries normally contain 30 to 40 weight percent of production waste solids.

To optimize milling time, engineering studies were carried out to investigate the effect of grain sizes on pore distributions/homogeneity and density of the final products to find the optimal size with its corresponding milling time. The slurries characteristic parameters were summarized in Table.2. Also to evaluate milling efficiency, the slurry was passed through a 63- mesh sieve and its residue was weighted to see how much of the slurry was sufficiently milled. The slurries were dried on

metal trays in the drying oven at 100 °C. Thus, the water in the slurries was evaporated.

**Table 2:** Slurry characteristic parameters.

Sieve Analysis	1.07±0.1
Viscosity (s)	45-50
Slurry Densities (g/L)	1650 ±30

After drying, dried sludge was reduced to fine particles with iron roll and the particles size distribution were determined by means of sieves. Granular particles were simultaneously weighted at

700 g each of gypsum cassettes shown in Figure 2. Dimensions of gypsum cassettes were manufactured as 15 x 20 cm in our laboratory.



**Figure 2:** Gypsum Cassettes.

### Gas Ceramic Firing Process

Granules particle in cassettes were baked at 1200 °C for 4 hours using an electric ceramic kiln. The initial furnace temperature was measured as 45 °C and then gradually increased to 1200 °C until the end of the furnace firing time reached. The required heat for the pre-drying was provided by the fan in the furnace at various points. Thus, the final moisture content of the formed products had been reduced to less than 1% at the end of the pre-drying process. Furthermore, in cases where the products were very humid and the drying temperature was not enough, the temperature was raised up to 160 °C. Subsequently at the end of firing, the furnace temperature was gradually reduced to 100 °C by means of the heat through the kiln shaft to the cooling zone. Afterward, the width, length and height of the gas ceramics were measured to calculate the density.

### Material characterization

Semi quantitative analysis method is a unique and powerful method for elemental screening of materials. Besides, semi quantitative analysis in modern XRF method is performed without any reference materials used for the unknown sample analysis. In addition to this, optical analysis (Leica EZ4HD microscope) was applied used to investigate the porous morphology. Samples were cut from the final products using a cutting machine. At least three samples were prepared for each analysis. The

images of samples were acquired with a digital camera combined with a microscope. The total and average pore area of samples were measured from images. The Archimedes' method (using ethylene glycol as immersion fluid) was employed to evaluate the open porosity, bulk density, and water absorption of the samples.

Determination of bending strength by the three point method was used for measuring the mechanical strength of samples. To measure the mechanical strength of the samples, bending strength was determined using three point method on five specimen while their porous layers were faced down.

## RESULTS AND DISCUSSION

### Microstructures of Gas Ceramics

Dry casting method is used for the production of gas ceramics. In this method, ceramic masse was obtained by pouring ceramic powder into a gypsum cordierite-based mold. No compression was applied. As a result of the optimizations for the standard foam recipe, the firing temperature was determined to be 1205 °C. Prepared foams were tested to determine the material properties. Density and viscosity values were measured. The obtained density, viscosity, and sieve residue values are given in Table 3.

**Table 3:** Density and sieve analysis values.

Test No	R-169	R-170	R-171	R-172	R-173
Density (g/cm <sup>3</sup> )	0.209	0.269	0.177	0.172	0.143
Sieve Analysis	1.09	1.11	1.07	1.17	1.17
Viscosity (s)			45-50		
Density (g/L)			1650 ±30		

It was observed that the density value of the sample with the R-173 prescription code reached the desired low density. Experiments have been made on the temperature of the furnace for cost optimization via this recipe. It is foreseen that it will be sintered again by lowering the furnace regime. In the studies, the kiln regime temperature was

decreased to 14 °C and the sintering was determined as 1186 °C for 4 hours. The sample code was recorded as R-174. The density value of the R-174 sample is calculated 0.204 g/cm<sup>3</sup> and the sieve balance is 1.1. The image of the gas ceramic tile with the final product is shown in Figure 3.

**Figure 3:** Standard (colorless) gas ceramic tile with foam structure.

The very fine structure of the powder dimensions increases the reaction surface and facilitates sintering. Therefore, it will be possible to carry out the reaction at shorter periods or at lower temperatures. Besides the differences in powder sizes, powder particle size distributions are also of great importance. Particular attention was paid to this parameter for masse density.

Experiments were made with appropriate molding parameters and kiln regime calculations in order to minimize the differences in color tones which may occur in the colors to be used in production. After the colorless optimization, the samples were sintered at 1186 °C for 4 hours with the same procedures as various color alternatives. The visual comparison of the products obtained is given in Table 4.

### Characterization of Gas Ceramic

In light of the past experience of our company and the information obtained from the literature, one of the biggest difficulties that we may encounter in our project will be the fact that the cake is not stable. The cake is not homogeneous because it is obtained from waste from all parts of the factory. In order to prevent this situation, the cake will be blended and dried in the summer months. The moisture content of the waste after drying is expected to be a maximum of 16%. Chemical analysis results are of great importance in terms of their use in prescription due to the lack of homogeneity of the cake samples obtained. Semi quantitative analyses demonstrates determination of the chemical composition in ceramic masse samples by using the semi-quantitative analysis method. Table 5 shows the results of the chemical analysis of production waste taken from our waste water treatment plant in the summer months.

**Table 4:** Gas Ceramic Surfaces with pigment Composition.

Pigment Composition (g)	Gas Ceramic Surface
100 g of Masse Composition	
100 g of Masse Composition +5 g of AL-3304	
100 g of Masse Composition +5 g of AL-73017	
100 g of Masse Composition +5 g of AL-1304	

**Table 5:** Semi-quantitative (SQX) Analysis Results for Production Waste.

No	Component	Result (Mass %)	Detn. limit	El. Line	Intensity	w/o normal
1	MgO	1.0542	0.0583	Mg-KA	0.5940	1.0489
2	Al <sub>2</sub> O <sub>3</sub>	14.1483	0.1104	Al-KA	25.4299	14.0772
3	SiO <sub>2</sub>	63.8091	0.0653	Si-KA	107.3239	63.4887
4	P <sub>2</sub> O <sub>5</sub>	0.1244	0.0091	P-KA	0.6230	0.1238
5	K <sub>2</sub> O	2.8160	0.0110	K-KA	28.6577	2.8018
6	CaO	6.5865	0.0138	Ca-KA	53.4828	6.5535
7	TiO <sub>2</sub>	0.3575	0.0246	Ti-KA	1.4084	0.3557
8	Fe <sub>2</sub> O <sub>3</sub>	1.1323	0.0083	Fe-KA	32.1648	1.1266
9	ZnO	2.4076	0.0042	Zn-KA	255.0013	2.3955
10	ZrO <sub>2</sub>	2.1202	0.0197	Zr-KB	167.5752	2.1095
11	A.Z	5.4440	-	-	-	5.4440

According to the results of the chemical analysis of cake waste during our pre-feasibility study, the fact that the fire loss is not very high, showing that there will be no loss of raw material and gas output will be minimum. There are criteria to be considered in determining the ratio of filter press waste during use in the recipe. These can be called storage problems and pollution. Due to the contamination of the cake, there is a high probability of surface defects such as perforation

and dent on the glazed surface. In addition, the use of waste in the recipe can cause rheological problems.

The filter press cake obtained from the treatment plant was dried and blended and then added to the recipes. The results of the quantitative analysis to determine the content of the materials by semi-quantitative (SQX) analysis by X-ray spectroscopy are given in Figure 4.

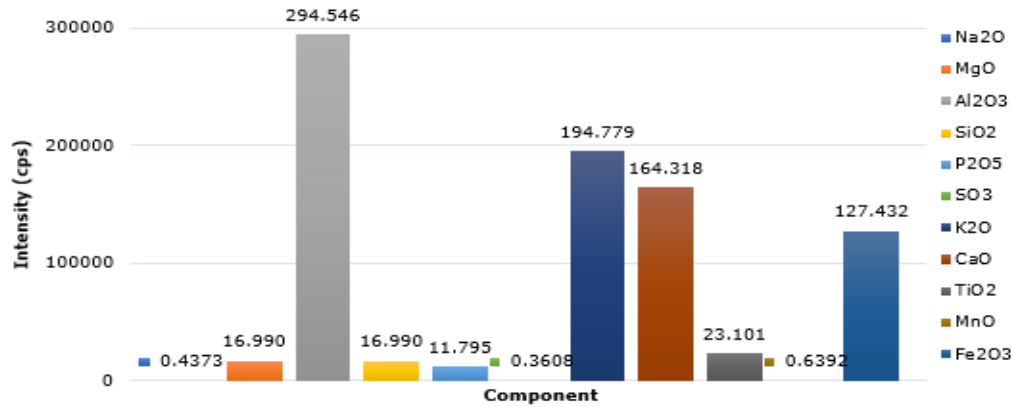


**Figure 4:** Semi-quantitative (SQX) Analysis Results for Gas Ceramic Masse.

At the end of the analysis, the components in the sample were determined. When the results were examined, it was found that the components complying with the operating standards did not contain any harmful components. It has been determined that fire loss is measured as 9,70% by mass and this value is suitable for working conditions. In addition, physical testing of the final products was performed.

#### Guidelines and Requirements of Gas Ceramics

Within the scope of the products obtained in our project, the original furnace process design, formulation and cassette designs have been done in order to create commercial potential in the properties such as color and pore homogeneity and strength. ISO creates documents that provide requirements, specifications, guidelines or characteristics that can be used consistently to ensure that materials, products, processes and services are fit for their purpose shown in Table 7.

For ceramic tiles, water absorption is used to classify products. This document outlines the procedures for the measurement of water absorption and related properties using classical Archimedean method. Impregnation of the open porosity is achieved by a vacuum method only. After the received samples had been tested according to standard ISO 10545-3, they measured is below the 0.05. In addition to this, frost resistance is a quality for tiles have when they are subjected to water at temperatures lower than 0 °C without being damaged by stress generated by their moisture content freezing. Ceramic tiles are

defined as resistance or not. As the water absorption of ceramic tiles is very low most ceramic tiles are frost resistant as in Table 7.

This ISO 40545-9 standard defines a test method for determining the resistance to thermal shock of all ceramic tiles under normal conditions of use. The variation of the characteristics of the tested tiles was visually controlled. The results was determined as resistant. This crazing resistance test method is for the determination of the resistance to the formation of crazes by subjecting whole tiles to steam at high pressure in an autoclave, then examination of the tiles for crazes after applying a stain to the glazed surface. Resistance to chemicals is the capacity of the surface at room temperature to tolerate contact with chemicals (domestic products, staining chemicals, pool additives, acids and solvents) without alteration in its appearance. Unglazed tiles are divided into categories starting with U and for glazed tiles the category starts with G. Category A means they was no visible effect and for C there is a visible effect on the sides of the tile and the surface.

Light fastness and color fastness of ceramic tiles was determined by exposure to radiation of a mercury vapor lamp according to standard DIN 51094. This test enables the light fastness of ceramic tiles was evaluated with relation to changes in color under the action of artificial light, where the sample was tested and subjected for 28 days to the action of ultraviolet rays. The results showed that there were no visual differences between the tiles.

**Table 6:** Test Analysis Results for Gas Ceramic.

Tests	Standard Limits	Experimental Results
Water absorption, apparent porosity, apparent relative density and bulk density of ceramic tiles	ISO 10545-3	≤0.05
Resistance To Thermal Shock	ISO 40545-9	Resistant
Crazing resistance	ISO 40545-11	Resistant
Frost resistance	ISO 40545-12	Resistant
Resistance to high concentrations of acids and alkalis	ISO 40545-13	GA
Resistance to household chemicals and swimming pool salts	ISO 40545-13	A
Surface hardness Mohs	EN 101	7
Testing of the light fastness and color fastness of ceramic tiles	DIN 51094	Resistant

## CONCLUSION

The effects of pore distributions / homogeneity and density on the properties of materials were investigated. It was observed that the size distribution of the colorful gas ceramic has a similar pore structure. It was determined that changes in the durability, density and heat permeability of the material to cause pore homogeneity and size distribution as well as open / closed pores. When the test results were examined, pore properties depend on the change of sieve residue and also pore sizes have been increase with the increase of sieve residue. As a result of this, volume of gas ceramic has increased and its density has decreased. Besides, the interaction of raw materials with between each other is also very important. Raw materials may increase the properties of each other positively or may reduce effect. Therefore, it seen that a difference in pore size distribution and density variation of the final products during the experiments. Most importantly, it is one of the innovative aspects of project that creates a healthy living space for the environment by holding the moisture owing to the high diffusion feature. The advantages of the final product and its superior properties from other alternative materials has high thermal insulation, high compression strength, flame retardant, low water absorption (~0) and low density. It was determined to use areas such as in heat insulation for ceramic floor tiles, in prefabricated buildings and also floor applications purpose for garden use decoratively considering that the properties of product. A competitive advantage is provided in virtue of the process design which can be changed according to the usage conditions and also the potential can be applied to the desired properties.

Within this scope, it is aimed to carry out alternative studies in line with the global demands. The final product, using by especially 30-40% of production waste, has become a new point of view

for the market in gas ceramic applications. Seranit-Serra product range has been expanded and also has been entered into the new market considering the characteristics and structure of the products.

## ACKNOWLEDGEMENTS

This research was supported by Seranit Granite Ceramic Factory. NE would like to extend her thanks and gratitude to Seranit Ceramics Factory, which provided support for the emergence of the project by providing resource within the scope of the project work.

## REFERENCES

1. Kalemtaş, Ayşe. Seramik Matrisli Kompozit Malzemeler. Bursa : Putech and Composites, 2015.
2. Dhandapani SP, Jayaram V, Surappa MK. Growth and microstructure of Al<sub>2</sub>O<sub>3</sub>/SiC/Si(Al) composites prepared by reactive infiltration of silicon carbide preforms. Acta Metallurgica et Materialia. 1994 Mar;42(3):649-56.
3. Peng LM, Han KS, Cao JW, Noda K. Fabrication and mechanical properties of high-volume-fraction Si<sub>3</sub>N<sub>4</sub>-Al-based composites by squeeze infiltration casting. Journal of Materials Science Letters. 2003;22(4):279-82.
4. Silicon carbide. In: Kirk-Othmer Encyclopedia of Chemical Technology. Wright, Nicholas T. USA (NJ) : John Wiley & Sons, 2006.
5. Førelund S, Bye E, Bakke B, Eduard F. Exposure to Fibres, Crystalline Silica, Silicon Carbide and Sulphur Dioxide in the Norwegian Silicon Carbide Industry. The Annals of Occupational Hygiene. 2008 Jun 11;52(5):317-36.

6. Akpınar, Süleyman. Kordiyerit Mullit Esaslı Karbür Katkılı Sıvı Metal Filtreleri. İzmir : Dokuz Eylül Üniversitesi Fen Bilimleri Enstitüsü, 2009.

7. Oliveira FAC, Dias S, Vaz MF, Fernandes JC. Behaviour of open-cell cordierite foams under compression. Journal of the European Ceramic Society. 2006 Jan;26(1-2):179-86.





## COMPARATIVE ANALYSIS OF CASCADE REFRIGERATION SYSTEMS' PERFORMANCE and ENVIRONMENTAL IMPACTS

Ebru Mançuhan<sup>a\*</sup>, Barış Tunç<sup>a</sup>, Kübra Yetkin<sup>a</sup>, Cem Çelik<sup>b</sup>

<sup>a</sup> Faculty of Engineering, Chemical Engineering Department, Marmara University, 34722, İstanbul Turkey

<sup>b</sup> Faculty of Engineering, Mechanical Engineering Department, Marmara University, 34722, İstanbul Turkey

**Abstract:** The aim of our study is to propose a theoretical model to analyze the energy efficient and environment friendly cascade system for various refrigerant pairs. In order to realize, the optimum cascade evaporation temperature ( $T_{OPT,CAS,E}$ ) which maximize the performance, coefficient of performance (COP) values are determined for different refrigerant pairs of the system. After the optimization, two different cases have been investigated through a thermodynamic analysis to discover the best refrigerant pair for the system. Natural refrigerant  $CO_2$  is selected instead of R404A which has high Global Warming Potential (GWP) value for the low temperature cycle (LTC). On the other hand, synthetic refrigerants (R134a, R152a) and a natural refrigerant ( $NH_3$ ) are chosen for the high temperature cycle (HTC). In order to determine, energy efficient and environmentally friendly cascade system, R134a/ $CO_2$ , R152a/ $CO_2$  and  $NH_3$ / $CO_2$  refrigerant pairs are investigated in Case 1. On the other hand, R134a/R404A, R152a/R404A and  $NH_3$ /R404A refrigerant pairs are investigated in Case 2. In calculations, the evaporation temperature ( $T_E$ ) is varied from -20 °C to -40 °C in LTC. The condensation temperature ( $T_C$ ) is considered to be between 30 °C and 45 °C in HTC. Mass flow rate requirements of systems for various refrigeration capacities ( $Q_{Evap}$ ) are calculated for different refrigerant pairs. Moreover, the  $COP_{max}$  and total equivalent warming impact (TEWI) values of the system's refrigerant pairs are evaluated and compared for various operating conditions.

**Keywords:** Cascade system, Optimization, TEWI, COP, Refrigerant pairs.

**Submitted:** November 12, 2018. **Accepted:** March 13, 2019.

**Cite this:** Mançuhan E, Tunç B, Yetkin K, Çelik C. COMPARATIVE ANALYSIS OF CASCADE REFRIGERATION SYSTEMS' PERFORMANCE and ENVIRONMENTAL IMPACTS. JOTCSB. 2019;2(2):97-108.

**\*Corresponding author. E-mail:** [emancuhan@marmara.edu.tr](mailto:emancuhan@marmara.edu.tr).

### INTRODUCTION

Cascade refrigeration systems have been widely used in commercial and industrial applications. The system incorporates two or more refrigeration cycles with relevant refrigerants. An appropriate selection of refrigerants to operate the LTC and HTC should be made in order to obtain high COP values, besides reducing the refrigerants' impact on the environment during operation, leakage and recharge. Therefore, it is important to improve the energy efficiency of

cascade systems using different refrigerant pairs and to determine their total contribution to global warming. For this purpose, the COP and TEWI values are calculated and compared for various refrigerant pairs of the cascade system (1-4).

In the previous studies, there are few theoretical and experimental studies to evaluate the alternative refrigerants with respect to performance and environmental considerations in refrigeration applications (1-7). Llopis et al. (1) presented the

experimental evaluation of refrigerants R404A and R507A in the double-stage refrigeration plant. They concluded that the performance of R404A system is considerably higher than R507A system's when the plant operates without inter-stage system at low evaporation temperatures. Kilicaslan and Hosoz, (2) determined and compared the COP and irreversibility values of the cascade system with various refrigerant pairs such as R152a/R23, R290/R23, R507/R23, R717/R23, R404a/R23. They reported that refrigerant pair R717/R23 is the best for the cascade systems among all selected pairs. If there are some limitations for the use of the natural refrigerants, the pair R152a/R23 is the best solution. Cabello et al. (3) performed an experimental comparison of a cascade refrigeration plant with the refrigerant pairs R134a/R744 and R152a/R744 under a wide range of operating conditions. They concluded that the high GWP refrigerant (R134a) can be replaced with the low GWP refrigerant (R152a) in accordance with the new environmental regulations. As a result, the replacement of R134a with R152a is technically and energetically feasible. Oruç et al. (4) investigated experimentally a refrigeration system using low GWP alternative refrigerants of R453A and R442A as drop in replacements for R404A. Using R453A and R442A as alternatives for R404A reduced the GWP by %55 and %52. In addition, the alternative refrigerants could be directly used in a system constructed to operate with R404A. Baakem et al. (5) performed energy, exergy and economic analyses of a multistage refrigeration system using Engineering Equation Solver (EES) software. In this theoretical study, they examined eight different refrigerants such as R717, R22, R134a, R1234yf, R1234ze, R410A, R404A and R407C. The maximum COP (6.17) was calculated for R717 system whereas the minimum COP value (4.95) was calculated for R407C. It was found that the best alternative was R717, compared to the other refrigerants. Vaghela (6) examined theoretically the different alternative refrigerants such as R290, R600a, R407C, R410A, R404A, R152a and R1234yf as a drop in replacement of R134a. As a result of the

thermodynamic analysis, R1234yf is determined to be the best suitable alternative refrigerant to replace R134a. It has very low GWP although it causes lower COP values compared to R134a. Karampour and Savalla (7) identified the most promising solutions of CO<sub>2</sub> trans-critical booster systems. They determined that the state-of-the-art integrated CO<sub>2</sub> systems are energy efficient, environmentally friendly and compact solutions which provide the whole thermal demands of supermarkets in cold and warm climates.

### CASCADE REFRIGERATION SYSTEM

Some industrial applications require moderately low temperatures and the temperature range between high and low temperatures may be too large for a single refrigeration cycle. Moreover, a large temperature range means that a large pressure range in the cycle and poor performance for a compressor. In these conditions, the refrigeration process is performed in stages, namely, to have two or more refrigeration cycles operate in series. These refrigeration cycles are called cascade refrigeration cycles (8). The cascade system is principally two single vapor compression cycles that are integrated by a heat exchanger. In this study, the upper cycle utilizes R134a, R152a and NH<sub>3</sub> and rejects heat to the ambient air at high temperature ( $T_H$ ). The lower cycle uses CO<sub>2</sub> or R404A and absorbs heat from the refrigerated space at low temperature ( $T_L$ ). Figure 1a displays a schematic view of the cascade system. The lower cycle rejects heat to the upper cycle in the cascade heat exchanger. The cascade heat exchanger functions as an evaporator for the HTC and a condenser for the LTC. As shown in the T-s diagram in Figure 1b, there are the evaporation and condensation temperatures. These temperatures depend on the refrigerated space and ambient conditions. Moreover, in a cascade system, there are two additional temperatures being the condensation temperature of the LTC ( $T_{CAS,C}$ ) and the evaporation temperature of the HTC ( $T_{CAS,E}$ ).

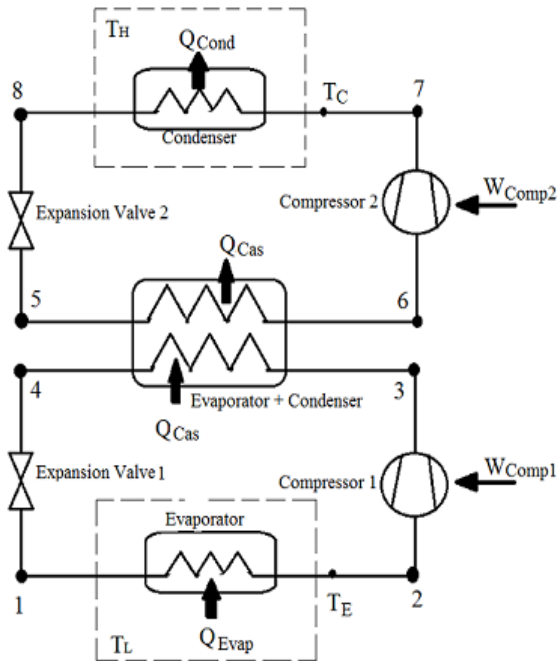


**Figure 1a:** Schematic view of the cascade system

For a given operating condition  $T_E$  and  $T_C$ , the intermediate temperatures can be determined through the use of optimization. Initially, the optimum  $T_{CAS,E}$  ( $T_{OPT,CAS,E}$ ) is computed from the  $T_E$  and  $T_C$ . With such cascade systems, the  $T_E$  range from  $-30\text{ }^\circ\text{C}$  to  $-55\text{ }^\circ\text{C}$  can be achieved. Since cascade systems are more complicated than the single-stage ones, the attention should be paid to the optimization of the operation parameters.

**UTILIZED REFRIGERANTS AND ENVIRONMENTAL ANALYSIS**

Synthetic refrigerants are utilized in most industrial refrigeration systems because of their higher cooling properties. Nowadays, as environmental issues have recently gained more importance considering GWPs and ozone depletion potentials (ODPs) natural refrigerants such as  $\text{CO}_2$  and various hydrocarbon compounds are proposed to replace synthetic refrigerants in industrial systems (9). This study investigates the effect of the low and high GWP refrigerants in the cascade system using thermodynamic analysis.

In Case 1, one fully and two partially natural refrigerant solutions have been investigated. Fully natural refrigeration solution,  $\text{CO}_2$  is the selected refrigerant of LTC and  $\text{NH}_3$  is the selected refrigerant of HTC. The partially

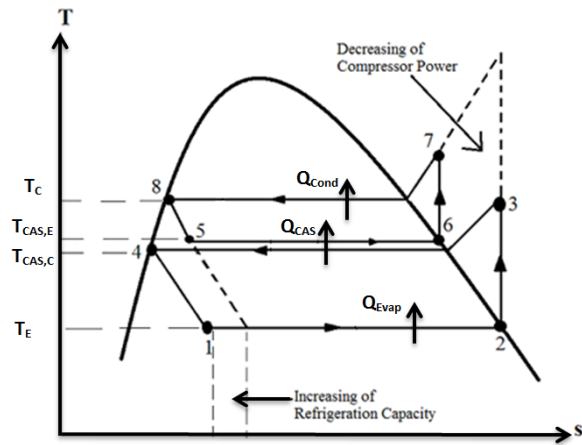


**Figure 1b:** T-s diagram of system

natural refrigerant solutions system uses the  $\text{CO}_2$  as the refrigerant of the LTC and the synthetic R152a and R134a as refrigerants of the HTC.  $\text{CO}_2$  is one of the most promising and environment-friendly refrigerant solutions due to its superior thermo-physical properties, low ODP and GWP. It is also a non-toxic, non-explosive, easily available refrigerant Pearson (9).  $\text{NH}_3$  is another natural refrigerant but it is toxic and flammable with A2 safety class. R152a has approximately same behavior like R134a for temperatures from  $-25\text{ }^\circ\text{C}$  to  $-10\text{ }^\circ\text{C}$ . Therefore, R134a can be replaced with R152a with minimum modification in the existing refrigeration system Cabello (3).

In Case 2, one partially natural refrigerant solution and two synthetic refrigerant solutions are examined. R404A, as a refrigerant with several appropriate properties, has been being widely used in industrial applications in over the world. However, due to several regulations regarding the environmental issues, the restriction of refrigerants (R404A, R134a and R152a) usage with high GWP has started. Main advantages of them are in A1 safety class and non-flammable refrigerants. However, they have high GWP. The advantage of R152a is its low GWP, whereas its disadvantage is its flammability. It is in the safety class A2.

**Table 1.** The physical, environmental and safety properties of refrigerants (10)

Refrigerants	Molecular weight (kg/kmol)	Boiling point (°C)	Critical temperature (°C)	Critical pressure (MPa)	Toxicity	Flammability	GWP
NH3	17.03	-33.3	132.3	11.28	A2	2	0
R152a	66.05	-25.0	113.5	4.52	A1	2	140
R134a	102.3	-26.1	101.1	4.06	A1	1	1370
<b>R404A</b>	<b>97.60</b>	<b>-46.5</b>	<b>72.04</b>	<b>3.72</b>	<b>A1</b>	<b>1</b>	<b>3922</b>
<b>CO<sub>2</sub></b>	<b>44.01</b>	<b>-56.6</b>	<b>31.0</b>	<b>7.38</b>	<b>A1</b>	<b>1</b>	<b>1</b>

TEWI is a GWP measure used to evaluate the direct and indirect global warming effects of the refrigeration systems. The direct effect which occurs as a result of refrigerant is released directly into the atmosphere. The indirect effect of CO<sub>2</sub> emissions released from fossil fuels consumed to produce energy to

drive the refrigeration system from beginning to the end of its lifetime. TEWI comparison provides a clear image of these effects in the service lifetime of the refrigeration system. TEWI values of different system's refrigerant pairs are calculated using the following correlation (11).

$$TEWI = GWP_{Ref} (m_{Ref} \times L_{annual} \times N + m_{Ref} \times (1-\alpha)) + (E_{annual} \times \beta \times N) \quad (1)$$

Where  $GWP_{Ref}$  is the GWP of the refrigerant,  $N$  is the system lifetime,  $m_{Ref}$  is the total refrigerant charge,  $L_{annual}$  is the refrigerant leakage rate,  $\alpha$  is the recycling factor,  $E_{annual}$  is energy consumed per year and  $\beta$  is the electricity regional conversion factor.

## THERMODYNAMIC ANALYSIS

### System Model Equations

The thermodynamic model of the cascade system is developed using the first law of thermodynamics. Considering the schematic and state points of Figures 1a and 1b, the following equations are used for the analysis. The COP and the mass flow ratio of two cycles are computed for various operating conditions (8).

Following assumptions are taken into consideration in the analysis.

- isenthalpic expansion of refrigerants in expansion valves,
- isentropic compressor efficiencies of 0.72 both low and high temperature cycles,
- potential and kinetic energy changes are neglected,
- heat and pressure losses in all components are neglected,
- the subcooling degree ( $\Delta T_{SUB}$ ) and superheat degree ( $\Delta T_{SUP}$ ) are kept constant to be 5 °C and 7 °C respectively.

Numerical calculations are performed using well-known EES software (12). The thermo-physical properties of the refrigerants (CO<sub>2</sub>, NH<sub>3</sub>, R134a, R152a and R404A) specified is obtained using EES. The mathematical model of the cascade system has been developed using the first law of thermodynamics. The derived equations are given below;

The capacity of the evaporator of LTC is defined as

$$\dot{Q}_{Evap} = \dot{m}_L (h_2 - h_1) \quad (2)$$

Compressor power consumption for HTC is given a:

$$\dot{W}_{Comp2} = \dot{m}_H (h_7 - h_6) \quad (3)$$

Similarly, compressor power consumption for LTC is

$$\dot{W}_{Comp1} = \dot{m}_L (h_3 - h_2) \quad (4)$$

The rate of heat transfer in the cascade system is calculated as

$$\dot{Q}_{CAS} = \dot{m}_H (h_6 - h_5) = \dot{m}_L (h_4 - h_3) \quad (5)$$

The mass flow rate ratio of circulating refrigerants in high and low temperature cycles is

$$\frac{\dot{m}_H}{\dot{m}_L} = \frac{(h_4 - h_3)}{(h_6 - h_5)} \quad (6)$$

The rate of heat rejection by the condenser of HTC:

$$\dot{Q}_{Cond} = \dot{m}_H (h_7 - h_8) \quad (7)$$

And finally, the overall COP of the cascade system is determined by:

$$COP = \frac{\dot{Q}_{Evap}}{\dot{W}_{Comp2} + \dot{W}_{Comp1}} = \frac{\dot{m}_L (h_2 - h_1)}{\dot{m}_H (h_7 - h_6) + \dot{m}_L (h_3 - h_2)} \quad (8)$$

## RESULTS AND DISCUSSION

### Optimization

The linear regression method is applied in two-variable optimization calculations using EES software (12). Two correlations are computed for each refrigerant pair from the two operating condition variables  $T_E$  and  $T_C$ . First, the  $T_{OPT,CAS,E}$  is calculated from the given  $T_E$  and  $T_C$ . Then, the  $COP_{max}$  is

calculated from the former  $T_{OPT,CAS,E}$  values. The computed correlations are presented in

Table 2. The unit used in the calculations is Kelvin (K).

**Table 2:** Correlations of the refrigerant pairs calculated for two case studies.

		Case 1	Case 2
R134a/CO <sub>2</sub>	$T_{OPT,CAS,E} = 73.235 + 0.34T_C + 0.365T_E$ $R^2 = 91.77\%$	$T_{OPT,CAS,E} = 15.5357 + 0.4736T_C + 0.4705T_E$ $R^2 = 97.74\%$	
	$COP_{max} = 4.540 - 0.0403T_C + 0.0404T_E$ $R^2 = 97.57\%$	$COP_{max} = 3.881 - 0.0425T_C + 0.0393T_E$ $R^2 = 99.98\%$	
R152a/CO <sub>2</sub>	$T_{OPT,CAS,E} = 51.14 + 0.3208T_C + 0.467T_E$ $R^2 = 99.91\%$	$T_{OPT,CAS,E} = 37.932 + 0.3484T_C + 0.5215T_E$ $R^2 = 97.90\%$	
	$COP_{max} = 3.9747 - 0.039T_C + 0.0418T_E$ $R^2 = 97.67\%$	$COP_{max} = 3.3795 - 0.038T_C + 0.04316T_E$ $R^2 = 95.81\%$	
NH <sub>3</sub> /CO <sub>2</sub>	$T_{OPT,CAS,E} = 85.18 + 0.2172T_C + 0.458T_E$ $R^2 = 99.95\%$	$T_{OPT,CAS,E} = 60.7717 + 0.2876T_C + 0.5045T_E$ $R^2 = 99.99\%$	
	$COP_{max} = 2.022 - 0.0330T_C + 0.0424T_E$ $R^2 = 92.84\%$	$COP_{max} = 3.006 - 0.0371T_C + 0.0436T_E$ $R^2 = 97.75\%$	

**Optimization results**

The proposed correlations are used to estimate the  $T_{OPT,CAS,E}$  and  $COP_{max}$  values from various operating parameters  $T_E$  and  $T_C$ . The estimations for Cases 1 and 2 are illustrated in Table 3.

**Table 3:** Predictions of  $T_{OPT,CAS,E}$  and  $COP_{max}$  for different refrigerant pairs.

		Case 1				Case 2							
		R134a/CO <sub>2</sub>		R152a/CO <sub>2</sub>		NH <sub>3</sub> /CO <sub>2</sub>		R134a/R404A		R152a/R404A		NH <sub>3</sub> /R404A	
T <sub>C</sub> (K)	T <sub>E</sub> (K)	T <sub>OPT</sub> (K)	COP	T <sub>OPT</sub> (K)	COP	T <sub>OPT</sub> (K)	COP	T <sub>OPT</sub> (K)	COP	T <sub>OPT</sub> (K)	COP	T <sub>OPT</sub> (K)	COP
318	253	273.7	2.03	271.3	2.15	270.1	2.26	285.2	2.14	280.6	2.20	279.9	2.24
	248	271.9	1.83	269.0	1.94	267.8	2.04	282.8	1.93	278.0	1.98	277.3	2.02
	243	270.0	1.63	266.6	1.73	265.5	1.83	280.5	1.72	275.5	1.77	274.8	1.81
	238	268.2	1.43	264.3	1.52	263.3	1.62	278.1	1.50	272.8	1.55	272.3	1.59
	233	266.4	1.22	262.0	1.31	260.9	1.41	275.8	1.29	270.2	1.34	269.8	1.37
313	253	272.0	2.23	269.7	2.34	269.0	2.42	282.8	2.34	278.9	2.39	278.4	2.43
	248	270.2	2.03	267.4	2.13	266.8	2.21	280.5	2.13	276.3	2.17	275.9	2.21
	243	268.4	1.83	265.0	1.93	264.5	2.00	278.1	1.91	273.7	1.96	273.4	1.99
	<b>238</b>	<b>266.5</b>	<b>1.63</b>	<b>262.7</b>	<b>1.72</b>	<b>262.2</b>	<b>1.78</b>	<b>275.7</b>	<b>1.70</b>	<b>271.1</b>	<b>1.74</b>	<b>270.9</b>	<b>1.77</b>
	233	264.7	1.42	260.4	1.51	259.9	1.57	273.4	1.49	268.5	1.53	268.3	1.55
308	253	270.3	2.43	268.1	2.54	268.0	2.59	280.5	2.54	277.2	2.58	277.0	2.61
	248	268.5	2.23	265.8	2.33	265.7	2.37	278.1	2.32	274.6	2.36	274.5	2.39
	243	266.6	2.03	263.4	2.12	263.4	2.16	275.7	2.11	272.0	2.15	271.9	2.18
	238	264.8	1.83	261.1	1.91	261.1	1.95	273.4	1.90	269.4	1.93	269.4	1.96
	233	263.0	1.62	258.8	1.70	258.8	1.74	271.0	1.68	266.7	1.72	266.9	1.74
303	253	268.6	2.63	266.5	2.73	266.9	2.75	278.1	2.73	275.5	2.77	275.6	2.80
	248	266.8	2.43	264.2	2.52	264.6	2.54	275.7	2.52	272.8	2.55	273.0	2.58
	243	264.9	2.23	261.8	2.32	262.3	2.33	273.4	2.31	270.2	2.34	270.5	2.36
	238	263.1	2.03	259.5	2.11	260.0	2.11	271.0	2.09	267.6	2.12	268.0	2.14
	233	261.3	1.83	257.2	1.90	257.7	1.90	268.7	1.88	265.0	1.91	265.5	1.93

**Thermodynamic analysis results**

Various pairs of refrigerant such as R134a/CO<sub>2</sub>, R152a/CO<sub>2</sub>, and NH<sub>3</sub>/CO<sub>2</sub> are investigated in Case 1. Similarly, R134a/R404A, R152a/R404A, and NH<sub>3</sub>/R404A are examined in Case 2. The cases were investigated due to the variations in T<sub>E</sub> and T<sub>C</sub>. The other operating parameters were kept constant such as ΔT<sub>CAS</sub>, the subcooling and superheat degrees were assumed as 6 K, 5 K and 7 K respectively.

**The Effect of T<sub>E</sub> on COP<sub>max</sub>**

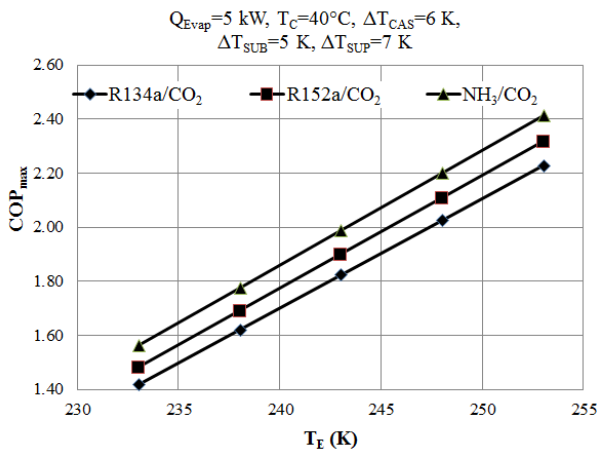


**Figure 2a:** Influence of T<sub>E</sub> on COP<sub>max</sub>(Case 1)

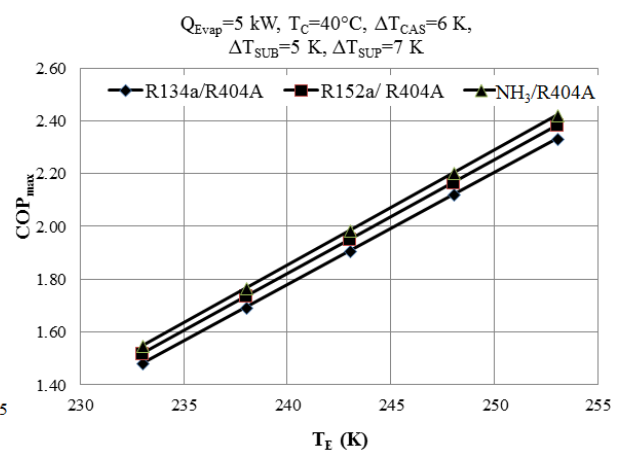


**Figure 2b:** Influence of T<sub>E</sub> on COP<sub>max</sub>(Case 2)

**Effect of T<sub>C</sub> on COP<sub>max</sub>**

The effect of T<sub>C</sub> on COP<sub>max</sub> was investigated. The T<sub>E</sub> was kept constant at -35 °C. The COP<sub>max</sub> values are demonstrated in Figures 3a and 3b for variable T<sub>C</sub> values such as; 45 °C, 40 °C, 35 °C, 30 °C. For all the systems

in Case 1 and Case 2, it is observed that, while the T<sub>C</sub> values increase the COP<sub>max</sub> values decrease. The NH<sub>3</sub>/CO<sub>2</sub> system and the NH<sub>3</sub>/R404A system appear to have minor advantages over the other refrigerant pairs on both cases.

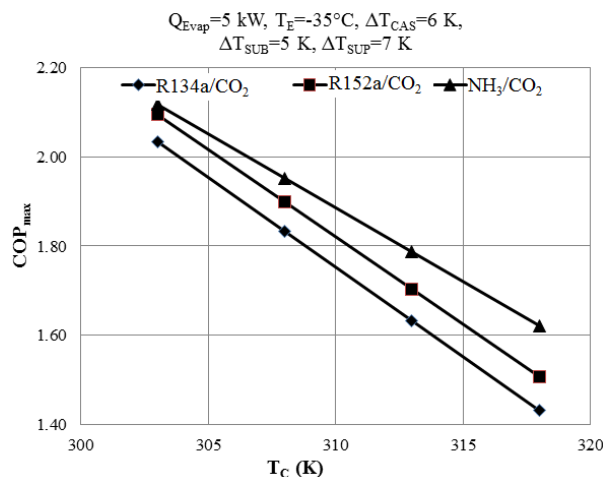


**Figure 3a:** Effect of T<sub>C</sub> on COP<sub>max</sub> (Case 1)

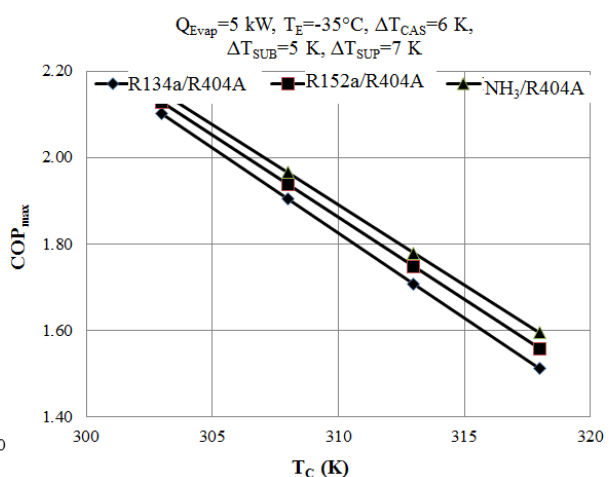


**Figure 3b:** Effect of T<sub>C</sub> on COP<sub>max</sub> (Case 2)

**Effect of T<sub>E</sub> on T<sub>OPT,CAS,E</sub>**

T<sub>OPT,CAS,E</sub> values were calculated for various evaporation temperatures (T<sub>E</sub>). While the T<sub>C</sub> was kept constant at 40 °C, T<sub>E</sub> values were

varied between -40 °C and -20 °C. The variations of T<sub>OPT,CAS,E</sub> values are depicted in Figures 4a and 4b. In Case 1, relatively higher T<sub>OPT,CAS,E</sub> values are calculated for

R134a/CO<sub>2</sub> than the other refrigerant pairs. Similarly, in Case 2, relatively higher T<sub>OPT,CAS,E</sub> values are observed for

R134a/R404A system. The other refrigerant pairs demonstrate similar behavior in both cases.

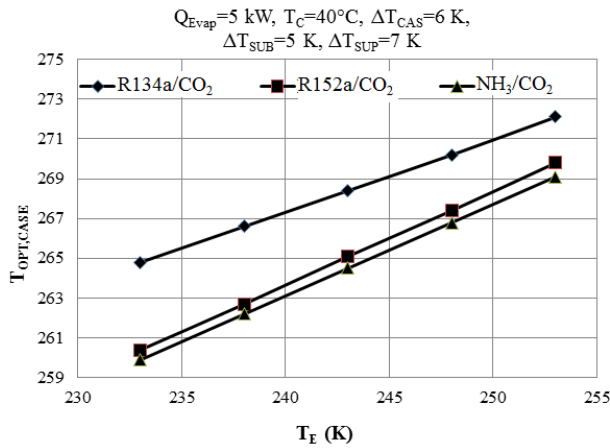


Figure 4a: Effect of T<sub>E</sub> on T<sub>OPT,CASE</sub> (Case 1)

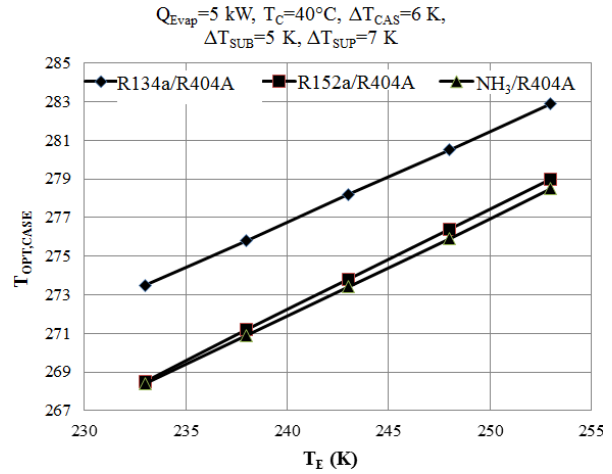


Figure 4b: Effect of T<sub>E</sub> on the T<sub>OPT,CASE</sub> (Case 2)

**Effect of T<sub>C</sub> on T<sub>OPT,CAS,E</sub>**

The T<sub>OPT,CAS,E</sub> values are evaluated for variable T<sub>C</sub> values between 45 °C and 30 °C while T<sub>E</sub> kept constant at -35 °C. Relatively higher T<sub>OPT,CAS,E</sub> values for R134a/CO<sub>2</sub> and

R134a/R404A systems are demonstrated in Figures 5a and 5b. On the other hand, systems with R152a/CO<sub>2</sub> and NH<sub>3</sub>/CO<sub>2</sub> pairs share common T<sub>C</sub> values in each case.

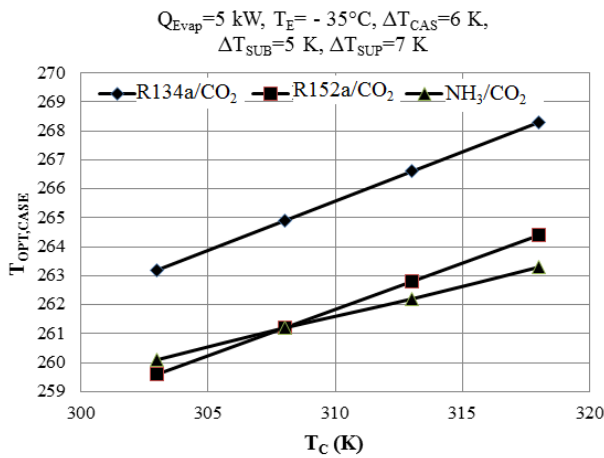


Figure 5a: Effect of T<sub>C</sub> on T<sub>CAS,E</sub> (Case 1).

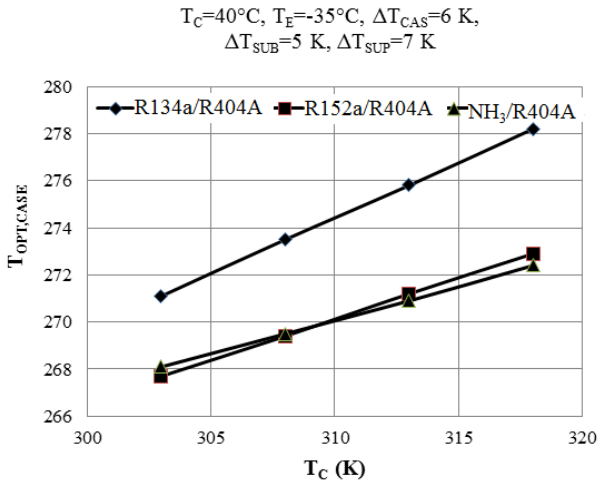


Figure 5b: Effect of T<sub>C</sub> on T<sub>CAS,E</sub> (Case 2).

**Effect of Q<sub>Evap</sub> on mass flow rate of LTC and HTC refrigerants**

Required mass flow rates of refrigerant pairs for different refrigeration capacities are demonstrated in Table 4. It is observed that increasing the refrigeration capacities from 4 kW to 9 kW causes an increase in the mass flow rates of cascade refrigerant pairs. It is found that the mass flow rates of CO<sub>2</sub> are

lower compared to the mass flow rates of R404A. Additionally, for the chosen capacity of 5 kW, the use of CO<sub>2</sub> requires the lowest mass flow rate (0.022 kg/s) whereas using R404A requires the highest mass flow rate (0.038 kg/s) in LTC. The mass flow rates of HTC refrigerants are calculated and the same values are founded in two cases.

**Table 4:** Required mass flow rates of refrigerant pairs for different refrigeration capacities.

$Q_{Evap}$ (kW)	Case 1			Case 2		
	R134a/CO <sub>2</sub> (kg/s)	R152a/CO <sub>2</sub> (kg/s)	NH <sub>3</sub> /CO <sub>2</sub> (kg/s)	R134a/R404A (kg/s)	R152a/R404A (kg/s)	NH <sub>3</sub> /R404A (kg/s)
4	0.039/0.018	0.023/0.018	0.0050/0.018	0.039/0.030	0.023/0.030	0.0050/0.030
<b>5</b>	<b>0.048/0.021</b>	<b>0.028/0.021</b>	<b>0.006/0.021</b>	<b>0.048/0.038</b>	<b>0.028/0.038</b>	<b>0.006/0.038</b>
6	0.057/0.026	0.034/0.026	0.007/0.026	0.057/ 0.045	0.034/0.045	0.007/0.045
7	0.067/0.030	0.039/0.030	0.008/0.030	0.067/ 0.052	0.039/0.052	0.008/0.052
8	0.076/0.034	0.044/0.034	0.009/0.034	0.076/ 0.059	0.044/0.059	0.009/0.059
9	0.085/0.038	0.050/0.038	0.010/0.038	0.085/ 0.066	0.050/0.066	0.010/0.066

In Figure 6, it is observed that the use of R134a requires the highest mass flow rate whereas using NH<sub>3</sub> requires the lowest mass flow rate, due to its high latent heat of vaporization as HTC refrigerants. Mass flow rate values of R152a are between the values of R134a and NH<sub>3</sub> systems for the  $Q_{Evap}$  from 4 kW to 9 kW.

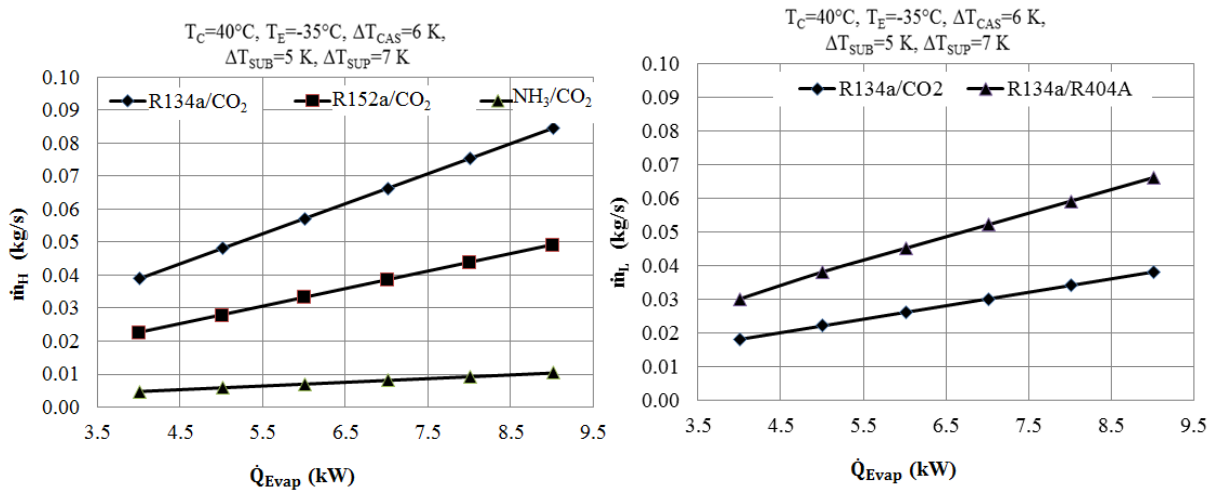


**Figure 6:** Mass flow rates of LTC and HTC refrigerants versus  $Q_{Evap}$ .

**TEWI comparison of the cascade refrigerant pairs**

In order to calculate TEWI values for Cases 1 and 2, model assumptions of the cascade system are determined. The  $T_E$ ,  $T_C$  and  $\Delta T_{CAS}$  values are taken as -35 °C, 40 °C and 6 K respectively. The refrigeration capacity is chosen as 5 kW. According to these assumptions, mass flow rates of HTC refrigerants are calculated as 0.048 kg/s for R134a, 0.028 for R152a and 0.006 kg/s for NH<sub>3</sub>. On the other hand, the mass flow rates of LTC refrigerants are founded as 0.022 kg/s for CO<sub>2</sub> and 0.038 kg/s for R404A. The

calculation of each refrigerant charge is done by using the estimation of  $\dot{m}_{Ref}x(240s)$ . This estimated value is used to size the liquid refrigerant receiver in refrigeration systems. The receiver’s volume is determined by the amount of charged refrigerant of the system (13). In addition, the power consumption of compressors is only taken into account in order to calculate the system energy consumption (Table 4). The power consumption of fans is not taken into account. The TEWI analysis assumptions are summarized in Table 5.

**Table 5:** TEWI analysis assumptions (11).

Parameter	$m_{Ref}^*$ (kg)	$L_{annual}$ (%)	N (years)	$\alpha$ (%)	$\beta^{**}$ (kg.CO <sub>2</sub> /kWh)	System operation (h/year)	$GWP_{Ref}$
Assumed values	$\dot{m}_{Ref}x(240s)$	12.5	15	0.7	$\beta = 0.65$	6570	$GWP_{CO2} = 1$ $GWP_{NH3} = 0$ $GWP_{R134a} = 1370$ $GWP_{R152a} = 140$ $GWP_{R404A} = 3922$

\* Unal (13), \*\*Horton (14)

The GWP values are relatively high for alternative refrigerant pairs in Cases 1 and 2. Therefore, TEWI analysis plays an important role in the selection of the system’s

refrigerant pairs effectively. For comparison between the Cases 1 and 2, the TEWI numbers are calculated from Eq.(1) and

presented in Table 6. Moreover, calculated  $COP_{max}$  values can be seen in Table 6.

**Table 6.** Comparison of TEWI and  $COP_{max}$  values for cascade system in Cases 1 and 2

	Case 1						Case 2					
	NH <sub>3</sub> /CO <sub>2</sub>		R152a/CO <sub>2</sub>		R134a/CO <sub>2</sub>		NH <sub>3</sub> /R404A		R152a/R404A		R134a/R404A	
Refrigerant charge (kg)	1.44	5.04	6.72	5.04	11.52	5.04	1.44	9.12	6.72	9.12	11.52	9.12
Refrigerant Leakage rate (% /year)	0.125		0.125		0.125		0.125		0.125		0.125	
Service life (years)	15		15		15		15		15		15	
Recycling factor	0.7		0.7		0.7		0.7		0.7		0.7	
GWP	1	0	1	140	1	1370	0	3922	140	3922	1370	3922
Direct CO <sub>2</sub> refrigerant's emission (kg CO <sub>2</sub> )	10.96	0	10.96	2,05	10.96	34,328	0	77,797	2,05	77,797	34,328	77,797
<b>Direct CO<sub>2</sub> emission equivalent (kg CO<sub>2</sub>)</b>	<b>10.96</b>		<b>2,057</b>		<b>34,338</b>		<b>77,797</b>		<b>79,843</b>		<b>112,124</b>	
Power consumption (kW)	<b>2.80</b>		<b>2.92</b>		<b>3.06</b>		<b>2.82</b>		<b>2.87</b>		<b>2.94</b>	
Service life (years)	15		15		15		15		15		15	
Operation (h/year)	6570		6570		6570		6570		6570		6570	
CO <sub>2</sub> emission factor	0.65		0.65		0.65		0.65		0.65		0.65	
<b>Indirect CO<sub>2</sub> emission equivalent (kg CO<sub>2</sub>)</b>	<b>179,361</b>		<b>187,048</b>		<b>196,016</b>		<b>180,642</b>		<b>183,845</b>		<b>183,205</b>	
<b>TEWI equivalent CO<sub>2</sub> emission (kg)</b>	<b>179,372</b>		<b>189,105</b>		<b>230,354</b>		<b>258,439</b>		<b>263,688</b>		<b>295,328</b>	
<b>COP<sub>max</sub></b>	<b>1.78</b>		<b>1.72</b>		<b>1.63</b>		<b>1.77</b>		<b>1.74</b>		<b>1.70</b>	

The results of the TEWI analysis are presented in Figure 7. A system with a synthetic refrigerant pair emits considerably higher amounts of greenhouse gases than a system with natural refrigerant pairs during their lifetime (7). Obviously, the direct

(leakage) of high GWP synthetic refrigerants is the reason for such an important difference. Additionally, the indirect part of TEWI might be improved with the low CO<sub>2</sub> emission electricity production.

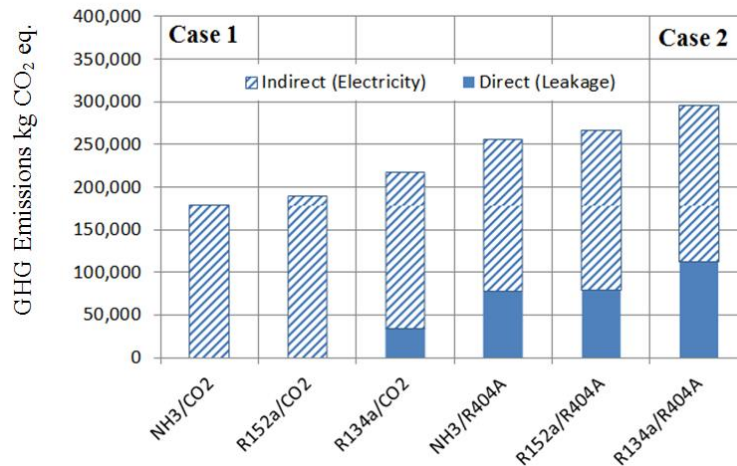


**Figure 7:** TEWI values comparison of systems in Cases 1 and 2

## CONCLUSIONS

A theoretical model is proposed to analyze and determine an energy efficient and environment-friendly cascade system for various refrigerant pairs. Two case studies are proposed. Case 1 has R134a/CO<sub>2</sub>, R152a/CO<sub>2</sub>, and NH<sub>3</sub>/CO<sub>2</sub> systems while Case 2 has R134a/R404A, R152a/R404A and NH<sub>3</sub>/R404A systems. The model is used to optimize the cascade evaporation temperature at given  $T_E$  and  $T_C$  values. After the optimization,  $COP_{max}$  values are calculated for all refrigerant pairs. While these systems are parametrically analyzed, the  $T_E$ ,  $T_C$  and  $Q_{Evap}$  values are taken as -35 °C, 40 °C and 5 kW respectively.

From the results obtained, it is presented that:

- For all the refrigerant pairs, increasing the  $T_E$  of LTC rises to  $COP_{max}$  values. However, increasing the  $T_C$  of HTC reduces to  $COP_{max}$  values for all studied systems.
- For all refrigerant pairs, increasing  $T_E$  and  $T_C$  rises the  $T_{OPT,CAS,E}$ . The  $T_{OPT,CAS,E}$  values of R134a/CO<sub>2</sub> are higher than the other refrigerants pairs in Case 1. Similarly, relatively higher  $T_{OPT,CAS,E}$  values are also observed for R134a/R404A system in Case 2.
- The mass flow rates of the system's refrigerant pairs have been examined in terms of various refrigeration capacities (from 4kW to 9 kW). In LTC, the use of CO<sub>2</sub> requires the lowest mass flow rate (0.022 kg/s), whereas using R404A requires the highest mass flow rate (0.038 kg/s). In HTC, it is also determined that the mass flow rate of NH<sub>3</sub> (0.006 kg/s) is lower to other

refrigerants (R134a and R152a). Therefore, it is concluded that the necessary total refrigerant amount is found less for natural ones.

- In Case 1, R134a/CO<sub>2</sub> pair is found to be the worst option due to resulting in the lowest  $COP_{max}$  (1.63) whereas the NH<sub>3</sub>/CO<sub>2</sub> is found to be the best option due to resulting in the highest  $COP_{max}$  (1.78). In addition, in Case 2, R134a/R404A is found to be the worst option due to resulting in the lowest  $COP_{max}$  (1.70) whereas the NH<sub>3</sub>/R404A is found to be the best option due to resulting in the highest  $COP_{max}$  (1.77).
- The TEWI results suggest that the environmental impact caused by system will decrease by having an efficient system rather than one that employs a refrigerant with a low GWP. According to the TEWI values, R134a/CO<sub>2</sub> and R134a/R404A systems have the highest contribution to CO<sub>2</sub> emission equivalent of indirect effect. These systems also have the lowest COP values. On the other hand, NH<sub>3</sub>/CO<sub>2</sub> and NH<sub>3</sub>/R404A systems have the lowest contribution to CO<sub>2</sub> emission equivalent of indirect effect. In addition, the  $COP_{max}$  values of the systems are calculated as the highest.

## NOMENCLATURE

### Abbreviations

COP	coefficient of performance (-)
GHG	greenhouse gases
GWP	global warming potential
EES	Engineering Equation Solver
HP	high pressure
LP	low pressure
ODP	ozone depletion potential
TEWI	total equivalent warming impact

Greek Letters

$\alpha$	recycling factor (%)
$\beta$	electricity regional conversion factor (kg.CO <sub>2</sub> /kWh)

Latin Letters

$h$	specific enthalpy (kJ/kg)
L	refrigerant leakage rate (% /year)
m	refrigerant charge (kg)
$\dot{m}$	mass flow rate (kg/s)
N	system lifetime (years)
$\dot{Q}$	heat transfer rate (kW)
s	specific entropy (kJ/kg.K)
T	temperature (°C or K)
$\Delta T$	temperature difference (K)
$\dot{W}$	power (kW)

Subscripts

C	condensation
CAS	cascade
Cond	condenser
Comp	compressor
E	evaporation
EV	expansion valve
Evap	evaporator
HTC	high temperature cycle
LTC	low temperature cycle
max	maximum
OPT	optimum
Ref	refrigerant
Sub	subcooling
Sup	superheating

**ACKNOWLEDGMENTS**

This article was presented in UKMK 2018 with presentation number S18 (ID 7263).

**REFERENCES**

- Llopis, R., Torrella, E., Cabello, R., and Sanchez, D., Performance evaluation of R404A and R507A refrigerant mixtures in an experimental double-stage vapour compression plant, *Appl. Energy*, 87(5), 2010, 1546-53.
- Kilicarslan A., Hosoz M., Energy and irreversibility analysis of a cascade refrigeration system for various refrigerant couples, *Energ. Convers. Manage.*, 51, 2010, 2947-54.
- Cabello R., Sanchez D., Llopis R., Catalan J., Nebot-Andres L., Torella E., Energy evaluation of R152a as drop in replacement for R134a in cascade refrigeration plants, *Appl. Therm. Eng.*, 110, 2017, 972-84.
- Oruc V., Devencioglu A.G., Ender S., Improvement of energy parameters using R442A and R453A in a refrigeration system operating with R404A, *Appl. Therm. Eng.*, 129, 2018, 243-49.
- Baakeem S.S., Orfi J., Alabdulkarem A., Optimization of a multistage vapor-compression refrigeration system for various refrigerants, *Appl. Therm. Eng.*, 136, 2018, 84-96.
- Vaghela J.K., Comparative evaluation of an automobile air-conditioning system using R134a and its alternative refrigerants, *Energy Procedia*, 109, 2017, 153-60.
- Karampour, M., Sawalla, S., State-of-the-art integrated CO<sub>2</sub> refrigeration system for supermarkets: A comparative analysis, *Int. J. Refrig.*, 86, 2018, 239-57.
- Cengel, Y.A., Boles, M.A., *Thermodynamics: An engineering Approach*, McGraw-Hill, Singapore, 2007.
- Pearson, A., Carbon dioxide-new uses for an old refrigerant. *Int. J. Refrig.*, 28, 2005, 1140-48.
- IPCC. *Climate Change 2013: The Physical Science Basis*, Cambridge University Press, Cambridge, United Kingdom and New York, USA, 2013.
- AIRAH, *Methods of Calculating Total Equivalent Warming Impact (TEWI) 2012, Best Practice Guidelines*. The Australian Institute of Refrigeration, Air Conditioning and Heating
- EES., 2017, *Engineering Equation Solver*, Academic Commercial, V10.326, fChart Software Inc.
- Sinar, U., Numerical analysis of a cascade refrigeration system operating at ultra-low temperatures, Marmara University, Master's Thesis, 2018.
- Horton, W.T., *Modelling of secondary loop refrigeration systems in supermarket applications*, Purdue University, PhD thesis, 2002.





## SYNTHESIS AND CHARACTERIZATION OF GRAPHENE QUANTUM DOTS FROM DRIED PINE LEAVES

Yunus ÖNAL<sup>1\*</sup>, Şifa KIR<sup>2</sup>, İlyas DEHRİ<sup>3</sup>, Ramazan ESEN<sup>4</sup>

<sup>1</sup>Inonu University, Faculty of Engineering, Department of Chemical Engineering, Malatya, Turkey

<sup>2,3</sup>Cukurova University, Faculty of Science & Letters, Department of Chemistry, Adana, Turkey

<sup>4</sup>Cukurova University, Faculty of Science & Letters, Department of Physics, Adana, Turkey

**Abstract:** In this study, it was aimed to obtain graphene quantum dots (GQDs) from dried pine leaf (DPL) (peanut pine (*Cedrus libani*, *Pinus nigra*)). Decomposition temperatures of the dried pine leaf were determined by DTA-TGA analyses in nitrogen atmosphere. DPL was subjected to carbonization in an ash furnace for 6 hours in air, at temperatures of 250, 300, 350 °C. The materials obtained from the thermal process are characterized using FT-IR, XRD, SEM-EDAX, UV-Vis, and Fluorescence spectrophotometry. When dissolved in deionized water, these materials emit blue fluorescence under UV-A and UV-C excitation. The emission and excitation peaks are very sharp, indicating a homogeneous particle distribution of GQDs in water. When the analysis results were examined, it was observed that the substance was obtained as a result of the carbonization process at 350 °C for 6 hours and it was compatible with GQDs data in the literature.

**Keywords:** Graphene Quantum Dots, Pine Leaf, Carbonization.

**Submitted:** November 08, 2018. **Accepted:** September 20, 2019.

**Cite this:** Önal Y, Kir Ş, Dehri İ, Esen R. SYNTHESIS AND CHARACTERIZATION OF GRAPHENE QUANTUM DOTS FROM DRIED PINE LEAVES. JOTCSB. 2019;2(2):109-20.

**\*Corresponding author. E-mail:** [yunus.onal@inonu.edu.tr](mailto:yunus.onal@inonu.edu.tr).

### INTRODUCTION

The exploration of the steam engine, the turning point of the Industry Revolution (1), increased the work of the researchers in the field of carbon in parallel with the increasing demand for coal. Carbon and its allotropes (diamond, graphite, fullerene, buckyball (C<sub>60</sub>), graphene and carbon nanotube) have become wide spread in the recent material science and applications. Nowadays, nanotechnology-related research has gained speed and new nanomaterials with unique properties such as carbon nanotubes, graphene quantum dots, carbon dots, fluorescent carbon nanotubes, graphene oxides, polymer dots, and nanodiamonds have been included in the literature. Due to the properties of carbon

nanomaterials, the uses are increasing day by day; with its unique optical properties, it is gaining importance in the biological applications (5) and oncology (6). As the source for carbon nanomaterials, chitin (7), activated carbon (8), graphite (9), citric acid (10), aspartic acid (11), turmeric (12), glucose (13), lemon peel (14), *Mangifera indica* leaves (15), broccoli (16) etc. raw materials from chemical or natural sources are used. Plants are the perfect source of carbon for the production and biosynthesis of carbon nanomaterial. Carbon nanomaterials can be obtained from the whole parts of the plants, from roots to flowers, from fruits to leaves (17, 18). GQDs which is carbon nanomaterials from the plants are clean, environmentally friendly, and relatively non-toxic. It is possible to obtain

single, double, and multi-layered structures with lateral size graphene layers thinner than 100 nm with diameters ranging within 3-20 nm (19). The GQDs offer unique properties, high transparency, and high surface area, it provides advantages in energy applications (capacitors, lithium ion batteries, and solar cells, etc.)(20). The applications of GQDs in ophthalmic devices, optoelectronics (photodetection, photovoltaics, light-emitting diodes (LEDs), and plasmonics...etc.) are increasing in many fields (21).

GQDs are new materials that have been used in various fields of technology, especially medicine. It can be obtained from every organic structure as well as live and dried leaves of plants. The reason why leaves are preferred is that they carry all the elements of the same chemical structure from nano to macromolecule in the growth stage. When the growth stops, all these structures are present in the leaf and as a result of heat treatment a structural arrangement occurs and they become GQDs structures.

The purpose of this study is to obtain GQDs from dried pine leaf and to determine the properties of the GQDs obtained. For this purpose, the leaves of the peanut pine used, were collected from the Garden of Inonu University in Malatya/Turkey. The connection part of the leaf to the tree trunk was removed by mechanical cleaning. Carbonization method was used for GQDs. The characterization of the obtained GQDs was determined by in situ methods.

## MATERIALS AND METHODS

### Synthesis of GQDs and Characterization

DTA-TGA analysis was performed in nitrogen atmosphere for dried pine leaf (DPL). In the carbonization process following the decomposition temperature, 250, 300, 350 °C temperatures were preferred. 100 grams of dried pine leaves were carbonized in air using the ash furnace at the temperatures of 250 °C (P1); 300 °C (P2) and 350 °C (P3). Characterization of all samples from the heat treatment was made by FT-IR (Thermo Scientific Nicolet iS10), XRD (Rigaku Miniflex II), Fluorescence spectrophotometer (Perkin Elmer LS 55), CHNS analysis (Thermo Scientific Flash 2000), and SEM (FEI Quanta 650 Model) techniques. UV / VIS (Perkin Elmer Lambda 25) and photoluminescence spectrophotometer (Perkin Elmer LS 55) were used to determine the maximum excitation and emission values of the material and the excitation-related emission activities. Camag UV cabin was used to observe the colors of fluorescence under UV-A and UV-C lamp. Thermal analysis was performed by DTA-TG Mettler Toledo Brand TGA / DSC 3+ system.

## RESULTS AND DISCUSSION

DTA-TGA analysis was performed in nitrogen atmosphere of dried pine leaf. The decay temperature was found to be between 130 °C – 370 °C (Figure 1).

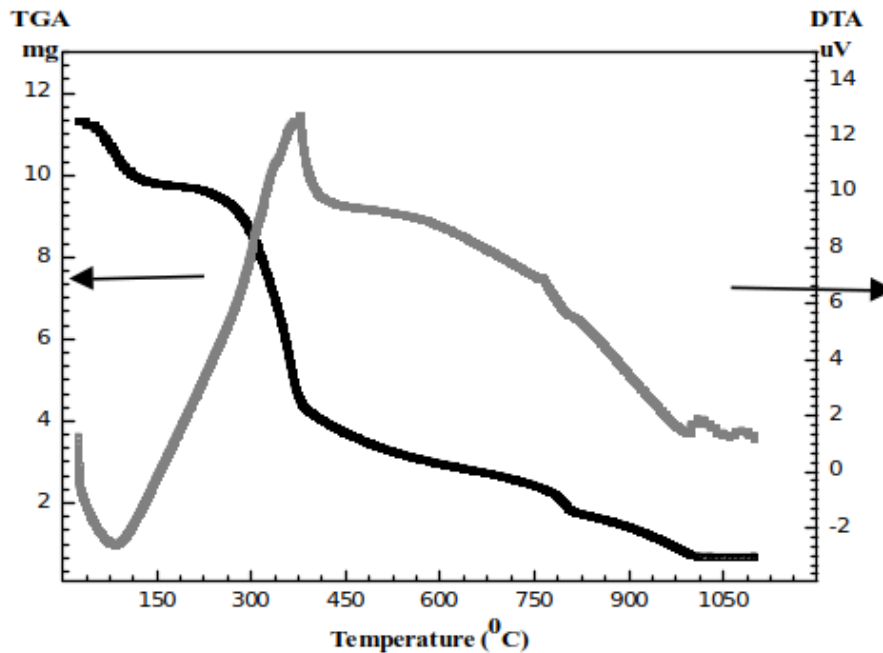


**Figure.1.** TGA-DTA graph of dried pine leaves (DPL).

When the mass loss-temperature graph was examined, it was observed that for the DPLs which were carbonized for 6 hours at different temperatures, the mass losses increase with the increase of carbonization temperature. There is a

mass loss of 44%; 60%; and 90% as a result of the carbonization process at a temperature of 250, 300, and 350 °C respectively (Figure 2.).

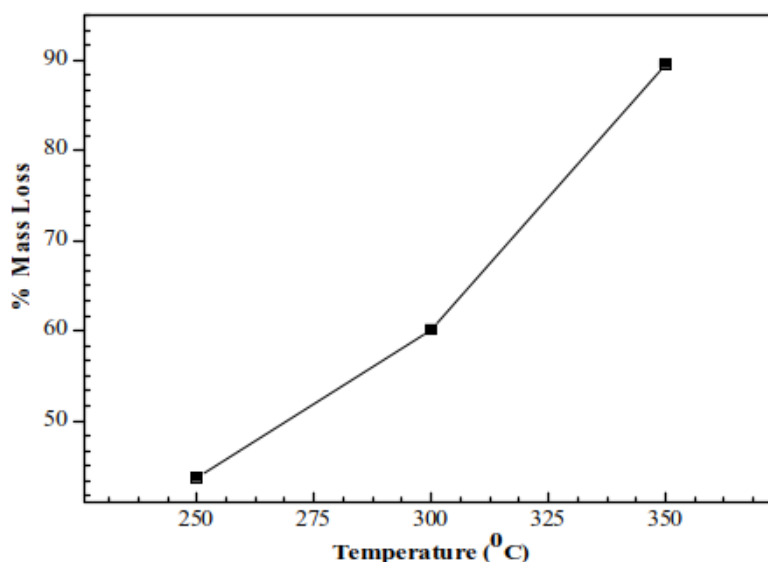


**Figure 2.** Mass Loss -Temperature Graph.

As a result of the ash determination of DPL, P1, P2, and P3 samples, ash ratio was calculated as 2.93%, 6.08%, 7.84%, and 26.67%, respectively. The results of the original elemental analysis of the substances formed as a result of

heat treatment and raw material are given in Table 1. When the results of the elemental analysis calculated by the dry ash free-based method are given in Table 1 in parentheses. When Table 1 is examined, it is seen that the rate of H% in the structure of P1 and P2

decreased; N% and S% increased slightly, while N% and S% increase in the structure of P3; the ratio of C% decreased to 300 °C and decreased at 350 °C, parallel to C%, O% decreases to 300

°C and increases to 350 °C with the effect of heat treatment . This indicates that a new substance was formed at 350 °C. In fact, XRD and FT-IR results support this situation.

**Table 1.** Original elemental analysis results of samples, the values calculated by the dry ashless free-based method are given in parenthesis. (% w/w)

	C%	H%	N%	S%	O% (by difference)
<b>DPL</b>	50.71 (52.24)	6.69 (6.89)	1.58 (1.63)	0.10 (0.10)	40.92 (39.14)
<b>P1</b>	59.98 (63.86)	4.36 (4.64)	2.23 (2.37)	0.10 (0.11)	33.33 (29.01)
<b>P2</b>	61.64 (66.88)	3.46 (3.75)	2.74 (2.97)	0.12 (0.13)	32.04 (26.26)
<b>P3</b>	38.87 (53.01)	1.82 (2.48)	5.08 (6.93)	0.54 (0.74)	53.69 (36.85)

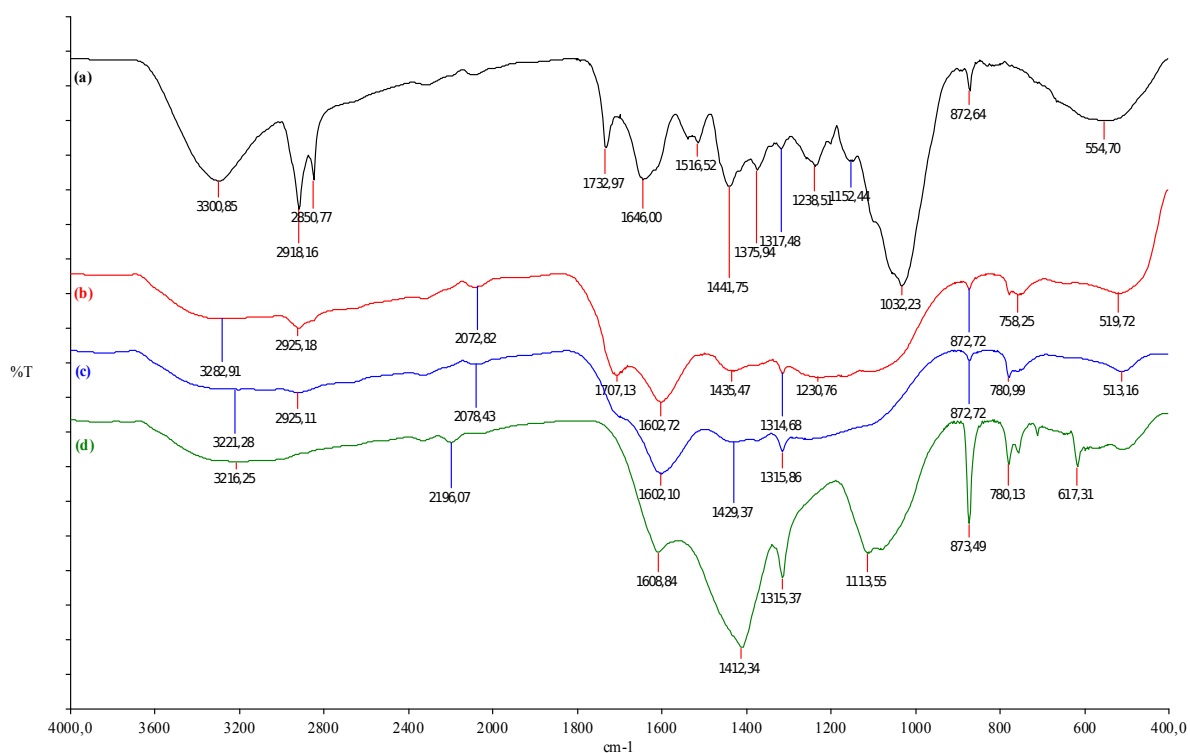


**Figure 3.** FT-IR spectra of DPL (a), P1 (b), P2 (c), P3 (d).

When FT-IR graphs are examined (Figure 3), it is seen that the DPL is a material with many organic functional groups (Figure 3a). After the carbonization process, aliphatic C-H groups and cellulosic hydroxyl groups leave the matrix. The stretching between 3000-3200  $\text{cm}^{-1}$  is clearly seen in the spectrum of dried pine leaf (Figure 3a). The double band at 2850 and 2918  $\text{cm}^{-1}$  belongs to the aliphatic C-H stress. The carbonyl band in 1732  $\text{cm}^{-1}$  belongs to (-C=O) while the band

at 1646  $\text{cm}^{-1}$  belongs to the structure C=C. The wide and sharp band of 1032  $\text{cm}^{-1}$  belongs to M-O-M structures. As the temperature increases, the hydroxyl band disappears due to the structural rearrangement. Similarly, structures with aliphatic C-H bonds appear to be reorganized. The heat treatment results a spectrum, which is similar to the FT-IR spectrum of GQDs structure (Figure 3d) compatible with the literature (15, 23, 24, 27).

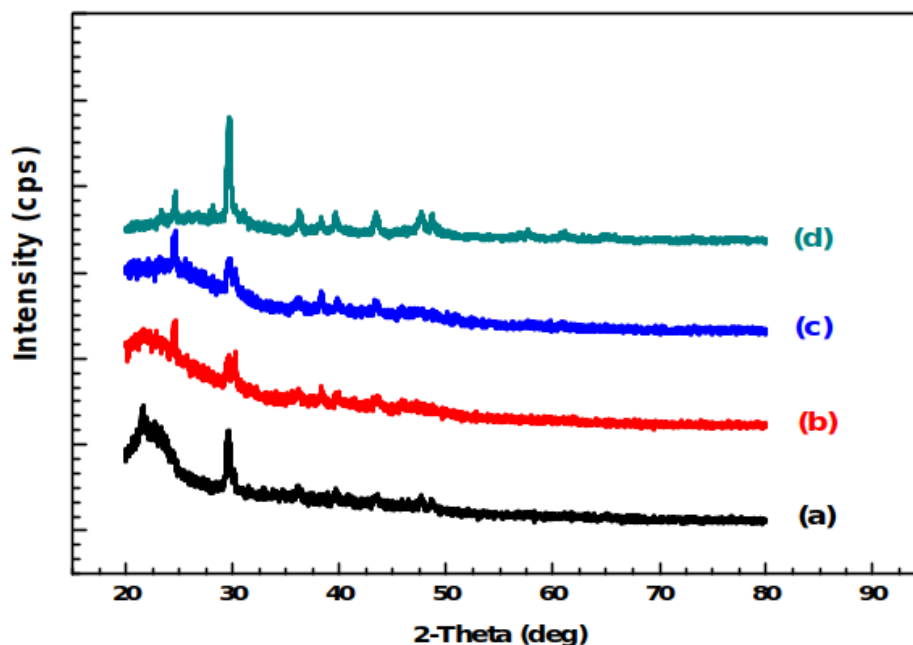


**Figure 4.** XRD spectrum of DPL (a), P1 (b), P2 (c) P3 (d).

When the XRD results are examined, it is seen that DPL, P1, and P2 materials contain amorphous and crystalline structured regions. The starting DPL contains more amorphous material. After carbonization, the crystalline part increases the reorganization of the system matrix by heating. The sharp peak at  $2\theta = 24.53$  degrees of P3 indicates the presence of graphene particles with a diameter of  $3.63 \text{ \AA}$  (Figure 4). As the temperature increases, the transition from amorphous to polycrystalline structure is observed. As a result of the structure regulation at  $350 \text{ }^\circ\text{C}$ , the peaks become sharper and symmetrical which indicates pure and better oriented crystallites. In the sample subjected to carbonization at  $350 \text{ }^\circ\text{C}$ , the diffraction values

which were previously at the noise level are noticed at  $2\theta = 36.13, 38.28, 39.65, 43.38, 47.66, 48.66, 57.51, \text{ and } 65.20$ . XRD diffraction data summary is given in Table 2. If the crystallization is continued for longer periods, these peaks may also be assigned. In the literature, most similar organic origin materials also synthesized similar matrices show amorphous structure. In this study, it was observed that the P3 obtained from the DPL, is the crystallites in the sample matrix (25). After carbonization at  $350 \text{ }^\circ\text{C}$  6 hours  $\text{CaCO}_3$  grains with sharp peak at  $2\theta = 29.58$  forms along a graphene phase with  $478 \text{ \AA}$  size and  $2\theta = 24.53$  (26).

**Table 2.** X-ray diffraction data summary.

<b>Sample</b>	<b>Main Peaks (2θ)</b>	<b>d(A)</b>	<b>Size(A)</b>	<b>FWHM (deg)</b>	<b>Remarks</b>	<b>Assignment</b>
<b>P3</b>	24.53	3.63	478	0.18	Sharp	Graphene
	29.59	3.01	268	0.320	Sharp	CaCO <sub>3</sub>

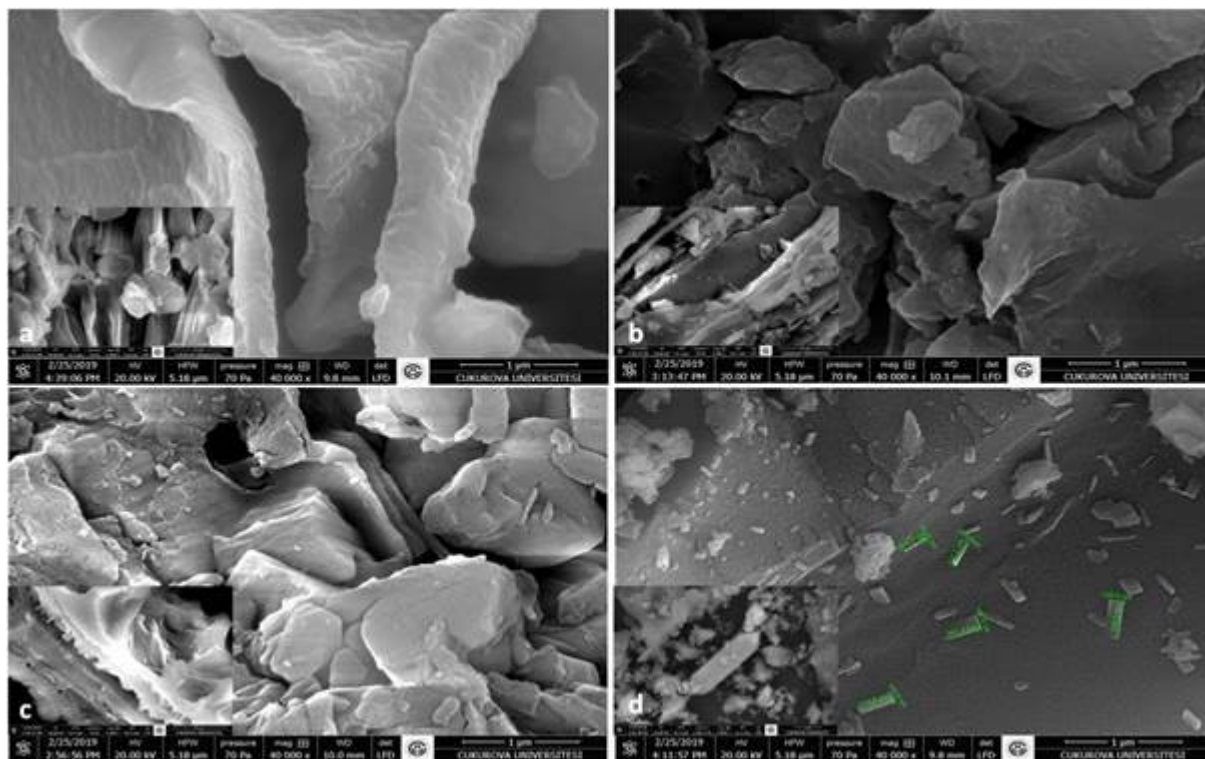


**Figure 5.** SEM image of DPL (a), P1 (b), P2 (c) P3 (d).

SEM photographs of all samples (a-d) are given in Figure 5. When the SEM image of the DPL is examined, (Figure 5a) it appears to have homogeneous and planar components. It is seen that as a result of heat treatment, cavities form in the structure (Figure 5b), by increasing the temperature, the planar layers begin to form in the structure (Figure 5c). When the SEM graph of P3 is examined, it is seen that a new hexagonal structure appears which is different from P1 and P2 (Figure 5d). When the image of dried pine leaf (Figure 5a) is examined, it is seen that it has a homogeneous structure with small channels. As a result of the heat treatment, it is seen that the channels where the macromolecular structure of

the pine leaf is disappeared and new structures are formed due to the structural arrangement as the temperature rises. In fact, mass loss as a result of heat treatment supports this result. Other structures are reorganized from nano to macromolecular structures while small groups of molecules are transitioned to the gas phase. Because of the temperature is not too high, the structural arrangement remains in the crystalline phase (28, 29, 30). The graphene quantum dots are embedded in the carbonized matrixe they cannot be seen in SEM studies but they are seen clearly in XRD data. When dissolved in water these GQDs appears in PL (photoluminescence) data which is given in the related section below.

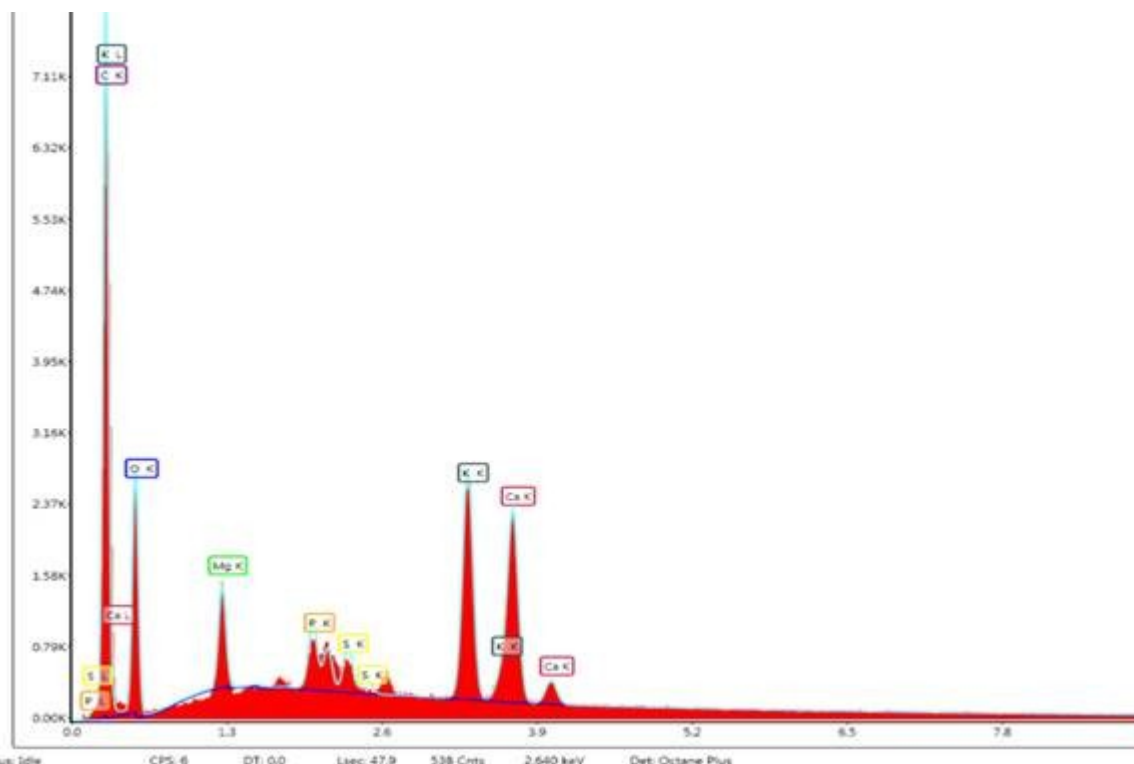


**Figure 6.** The EDAX graph of P3.

When the EDAX analysis result of the P3 is examined, it is seen that the sample matrix contains mostly C and O elements, along with the other elements Mg, P, S, K, and Ca. When this result is evaluated together with the result of FT-IR, the main structure is organic; the elements of Mg, P, S, K, and Ca may be related to organic functional groups (Figure 6).

For absorbance studies,  $1.10^{-3}$ ,  $1.10^{-2}$ ,  $1.10^{-1}$ , and 1 g of P3 material and 100 mL of pure water was added to the solution prepared and it was filtered, and it was used for 1 day. The solutions were analyzed using UV-Vis and fluorescence spectrophotometers under UV-A and UV-C lamp illumination. In addition, the results are depicted in Figure 7. In the figure, a very low value of 0.00998 absorbance was observed for the  $10^{-3}$

g / 100 mL sample. For the concentration of  $1.10^{-2}$  g / 100 mL, 3.6 absorbance value is observed at 333.69 nm wavelength and the absorption peak is narrow and sharp. This indicates that the components that make the fluorescence at this concentration are pure.

A similar result was obtained at a concentration of  $1.10^{-1}$  g / 100 mL. At a concentration of 1 g / 100 mL, the absorbance peak shifted to 340.62 nm and the peak expanded. This can be explained by the amount of water-soluble part of the specimen increased, these components give new absorbance values at different wavelengths. The fluorescence value has decreased significantly. Increased concentration combined with the presence of other components shielded the fluorescence of the UV emitting component.

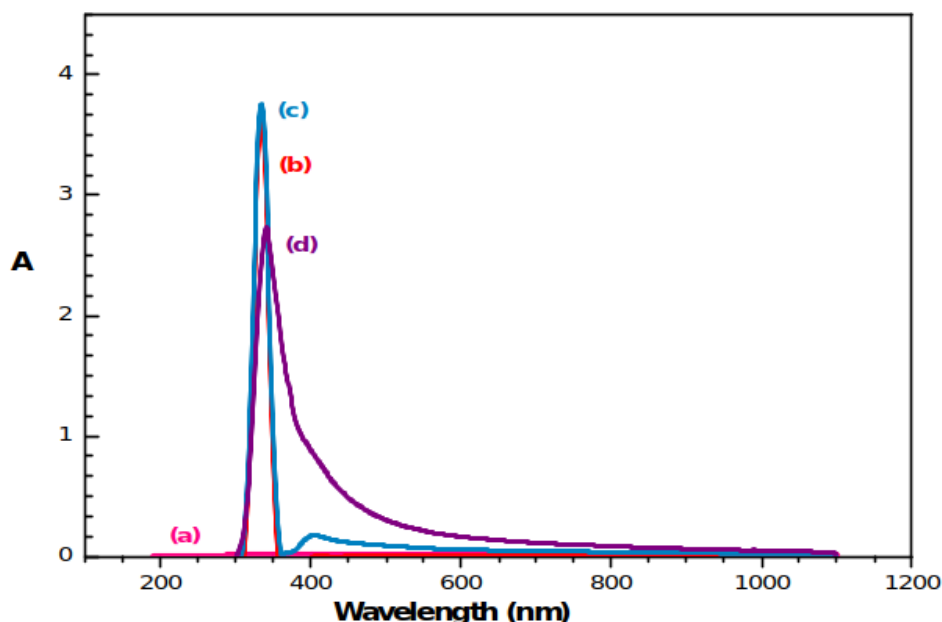


**Figure 7.** UV-Vis graph of  $1.10^{-3}$  g/100 mL (a),  $1.10^{-2}$  g/100 mL (b),  $1.10^{-1}$  g/100 mL (c), 1 g/100 mL solutions (d).

When the solutions under UV-A and UV-C light were photographed, it was observed that the sample containing  $1.10^{-3}$  g / 100 mL P3 material did not give any fluorescence; other solutions

give blue-colored fluorescence, increasing the concentration of solutions increased the fluorescence intensity (Fig. 8).



**Figure 8.** Left to right, distilled water ( $1.10^{-3}$  g,  $1.10^{-2}$  g,  $1.10^{-1}$  g and 1 g of P3 in 100 mL of distilled water) pictured under visible illumination (a), UV-A lamp (360 nm) (b); UV-C lamp (254 nm) (c).

It has been observed that the optical absorption properties of P3 obtained from the carbonization of dried pine leaves have very different properties than the total matrix of material (Figure 7-9). When Table 3 is examined,  $1.10^{-2}$ ;  $1.10^{-1}$  and 1 g of P3 solutions gave similar maximum excitation and emission values; the solution of  $1.10^{-3}$  g of P3 was found to be

different from the remaining samples. Taking into consideration that the emission and absorption peaks are very sharp, it can be said that they show same absorption wavelength with a measurement error of  $\pm 1$  nm. This property attributed to the homogeneity of the samples dissolved in water.

**Table 3.** Maximum excitation and emission values of prepared solutions.

	Maximum Excitation	Maximum Emission
<b><math>1.10^{-3}</math> g/100 mL</b>	220.1	297.5
<b><math>1.10^{-2}</math> g/100 mL</b>	537.9	536.6
<b><math>1.10^{-1}</math> g/100 mL</b>	536.3	534.7
<b>1 g/100 mL</b>	541.9	541.0

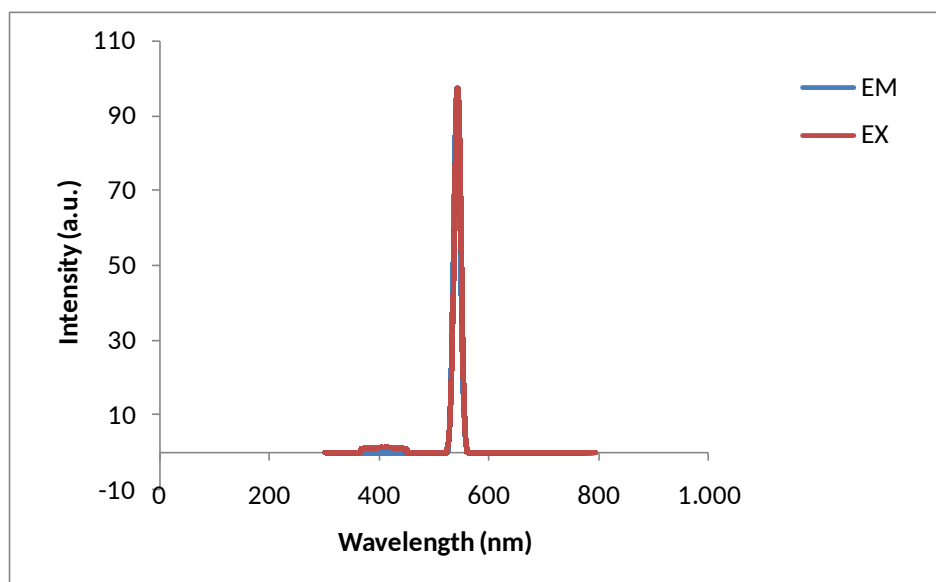


**Figure 9.** Emission and excitation graph of 1 g / 100 mL of P3 solution. The emission and excitation curves match perfectly so that one obstructs the other in the graph.

When the fluorescence analysis results were examined, it was seen that the solution with a concentration of  $1 \cdot 10^{-3}$  g / 100 mL did not give fluorescence. The emissions of the solutions with  $1 \cdot 10^{-2}$  g,  $1 \cdot 10^{-1}$  g, and 1 g of P3 substances show increased fluorescence with the concentration (536.5; 534.5; 541 nm maximum emission values 5.11; 27.91; 97.51 respectively). The graphene quantum dots obtained from dried pine leaves show sharper fluorescence peaks compared to other similar GQDs. This shows that the dimensions of the water-soluble particles have a sharp distribution ( $1 \cdot 10^{-3}$ ,  $1 \cdot 10^{-2}$ ,  $1 \cdot 10^{-1}$ , and 1 g/100 mL distilled water 0.6, 1.3, 1.3, and 1.3 nm). This shows that carbon nanostructures have the same size (homogeneous) distribution in distilled water. The optical PL data is very sharp indicating that structures contain very small number of molecules so widening effects due the size distribution is not observed.

## CONCLUSIONS

According to the SEM-EDAX result of raw pine leaf, it was determined that it contains mostly carbon, hydrogen, and oxygen. It is seen that as the temperature increases the mass loss increases as well. However, the elemental analysis show that a high ratio of organic component remains in the environment. As a result of heat treatment, it expected the organic components should decrease in our samples structural reorganization takes place. The FT-IR data also show that many organic components connected to the inorganic components still exist (like  $\text{CaCO}_3$ ). After the heat treatment, the P3

sample gave the emission in the UV-A region; it shows that the GQDs in the structure are well crystallized as a crystal structure in nanostructure. When carbonization temperature reaches to  $350^\circ\text{C}$  a sharp XRD pattern observed at  $2\theta=29.58$  indicating a  $\text{CaCO}_3$  grain formation with a size of  $268 \text{ \AA}$ . The graphene peak at  $2\theta=24.53$  also observed with  $478 \text{ \AA}$  grain size but with a smaller XRD peak. With this method it is clearly indicated that it can be used as a production method of GQDs.

## ACKNOWLEDGEMENT

This study was supported by the unit of Scientific Researches of Çukurova University in Adana, Turkey; Project no: FDK-2016-6191

## REFERENCES

1. Külcü R. Sanayi Devriminden 1700 Yıl Önce Yapılmış Erken Bir Keşif: Heron'un Buhar Türbini (Aerolipie). *Academia Journal of Social Sciences*. 2016;1(2):32-9.
2. Pryzhkova M. V. Concise Review: Carbon Nanotechnology: Perspectives in Stem Cell Research. *Stem Cells Translational Medicine*. 2013;2:376-83.
3. Jariwala D, Sangwan V. K, Lauhon L. J, Marks T. J, Hersam M. C. et al. Carbon nanomaterials for electronics,

- optoelectronics, photovoltaics, and sensing. [Chem Soc Rev.](#) 2013;42(7):2824-60.
4. Zhai W, Srikanth N, Kong L. B, Zhou K. et al. Carbon nanomaterials in tribology. *Carbon*. 2017;119:150-171.
  5. Wen J, Xu Y, Li H, Lu A, Sun S. et al. Recent applications of carbon nanomaterials in fluorescence biosensing and bioimaging. *Chemical Communications*. 2015;51(57):11331-524
  6. Mehra N. K, Jain A. K, Nahar M. et al. Carbon nanomaterials in oncology: an expanding horizon. *Drug Discovery Today*. 2018;23(5):1016-25.
  7. Shchipunov Y. A, Khlebnikov O. N, Silant'ev V. E. et al. Carbon Quantum Dots Hydrothermally Synthesized from Chitin. *Polymer Science, Ser. B*, 2015;57(1):16-22.
  8. Qian Z, Chai L, Tang C, Huang Y, Chen J, Feng H. A fluorometric assay for acetylcholinesterase activity and inhibitor screening with carbon quantum dots. *Sensors and Actuators B*. 2016;222:879-86.
  9. Muthurasu A, Ganesh V. et al. Horseradish Peroxidase Enzyme Immobilized Graphene Quantum Dots as Electrochemical Biosensors. *Appl Biochem Biotechnol*. 2014;174:945-59.
  10. Roushani M, Mavaei M, Rajabi H. R. et al. Graphene quantum dots as novel and green nano-materials for the visible-light-driven photocatalytic degradation of cationic dye. *Journal of Molecular Catalysis A: Chemical*. 2015;409:102-9.
  11. Zhang C, Cui Y, Song L, Liu X, Hu Z. et al. Microwave assisted one-pot synthesis of graphene quantum dots as highly sensitive fluorescent probes for detection of iron ions and pH value. *Talanta*. 2016;150:54-60.
  12. Ahmadian-Fard-Fini S, Salavati-Niasari M, Safardoust-Hojaghan H. et al. Hydrothermal green synthesis and photocatalytic activity of magnetic CoFe<sub>2</sub>O<sub>4</sub>-carbon quantum dots nanocomposite by turmeric precursor. *J Mater Sci: Mater Electron*. 2017;28:16205-14.
  13. Hallaj T, Amjadi M, Manzoori J. L, Shokri R. et al. Chemiluminescence reaction of glucose-derived graphene quantum dots with hypochlorite, and its application to the determination of free chlorine. *Microchim Acta*. 2015;182:789-96.
  14. Chatzimitakos T, Kasouni A, Sygellou L, Avgeropoulos A, Troganis A, Stalikas C. et al. Two of a kind but different: Luminescent carbon quantum dots from Citrus peels for iron and tartrazine sensing and cell imaging. *Talanta*. 2017;175:305-12.
  15. Kumawat M. K, Thakur M, Gurung R. B, Srivastava R. et al. Graphene Quantum Dots from *Mangifera indica*: Application in Near-Infrared Bioimaging and Intracellular Nanothermometry. *ACS Sustainable Chem. Eng.* 2017, 5, 1382-91.
  16. Arumugam N, Kim J. et al. Synthesis of carbon quantum dots from Broccoli and their ability to detect silver ions. *Materials Letters*. 2018; 219:37-40.
  17. Das R, Bandyopadhyay R, Pramanik P. et al. Carbon quantum dots from natural resource: A review. *Materials Today Chemistry*. 2018;8:96-109.
  18. Zaytseva O, Neumann G. et al. Carbon nanomaterials: production, impact on plant development, agricultural and environmental applications. *Chem. Biol. Technol. Agric.* 2016;3:17.
  19. Benítez-Martínez S, Valcárcel M. et al. Graphene quantum dots as sensor for phenols in olive oil. *Sensors and Actuators B*. 2014;197:350-7.
  20. Bak S, Kim D, Lee H. et al. Graphene quantum dots and their possible energy applications: A review. *Current Applied Physics*. 2016;16:1192-201.
  21. Jin Z, Owour P, Lei S, Ge L. et al. Graphene, graphene quantum dots and their applications in optoelectronics. *Current Opinion in Colloid & Interface Science*. 2015;20:439-53.
  22. Amjadi M, Shokri R, Hallaj T. A new turn-off fluorescence probe based on graphene quantum dots for detection of Au(III) ion. *Spectrochimica Acta Part A: Molecular*

- and Biomolecular Spectroscopy. 2016; 153: 619–24.
- 23.** Habiba K, Makarov V. I, Avalos J, Guinel M. J. F, Weiner B. R, Morell G. et al. Luminescent graphene quantum dots fabricated by pulsed laser synthesis. Carbon. 2013;64:341 –50.
- 24.** Teymourinia H, Salavati-Niasari M, Amiri O, Safardoust-Hojaghan H. et al. Synthesis of graphene quantum dots from corn powder and their application in reduce charge recombination and increase free charge carriers. Journal of Molecular Liquids. 2017; 242: 447–55.
- 25.** Ettefaghi E, Ghobadian B, Rashidi A, Najafi G, Khoshtaghaza M. H, Pourhashem S. et al. Preparation and investigation of the heat transfer properties of a novel nanofluid based on graphene quantum dots. Energy Conversion and Management. 2017;153:215–23.
- 26.** Sekkal W, Zaoui A. et al. Nanoscale analysis of the morphology and surface stability of calcium carbonate polymorphs. Scientific Reports. 2013; 3 : 1587.
- 27.** Das T, Saikia B. K, Dekaboruaha H. P, Bordoloia M. et al. Blue-fluorescent and biocompatible carbon dots derived from abundant low quality coals. Journal of Photochemistry & Photobiology, B: Biology. 2019; 195: 1–11.
- 28.** Bedeloğlu A, Taş M, Grafen ve Grafen Üretim Yöntemleri. AKU J. Sci. Eng. 16 2016; 031203: 544-54.
- 29.** Liu X, Yang R, Xu M, et al. Hydrothermal Synthesis of Cellulose Nanocrystal-Grafted-Acrylic Acid Aerogels with Superabsorbent Properties. Polymers. 2018; 10, 1168.
- 30.** Tiyek İ, Dönmez U, Yıldırım B, et. al. Kimyasal yöntem ile indirgenmiş grafen oksit sentezi ve karakterizasyonu. SAÜ Fen Bil Der. 2016; 20. Cilt, 2. Sayı: s. 349-57.





## Removal of Lead and Cadmium Ions from Aqueous Solutions by Olive Pomace as a Low-Cost Biosorbent

Onur Uzunkavak , Günseli Özdemir\* 

Ege University, Faculty of Engineering, Chemical Engineering Department, Izmir, Turkey

**Abstract:** In this study, the adsorptive performance of olive pomace on lead and cadmium removal from aqueous solutions was investigated. Process parameters such as particle size, solution pH, contact time, initial ion concentration, and incubation temperature were evaluated using batch experiments. It was found that lead and cadmium adsorptions followed a pseudo second order kinetics. Sorption amount for lead and cadmium ions at 25 °C was obtained 33 and 8 mg/g, respectively, with 1 g/L olive pomace loading at pH 5.5 and 6. Adsorption isotherms were best fitted with the Redlich-Peterson and Langmuir-Freundlich models for lead and cadmium adsorptions, respectively. Thermodynamic calculations revealed that the adsorption process is feasible and spontaneous in nature. Adsorbent characterization was accomplished using ATR-FTIR, SEM, and BET analyses, whereas the surface charge was determined measuring the point of zero charge ( $pH_{PZC}$ ).

**Keywords:** Wastewater treatment, biosorption, olive pomace, lead, cadmium.

**Submitted:** November 09, 2018. **Accepted:** April 16, 2019.

**Cite this:** Uzunkavak O, Özdemir G. Removal of Lead and Cadmium Ions from Aqueous Solutions by Olive Pomace as a Low-Cost Biosorbent. JOTCSB. 2019;2(2):121-32.

**\*Corresponding author.** E-mail: [gunseli.ozdemir@ege.edu.tr](mailto:gunseli.ozdemir@ege.edu.tr).

### INTRODUCTION

Environmental pollution problems have been a rising concern of modern engineering. Heavy metal pollution is one of the most serious problems and the removal of heavy metals from the environment is of particular importance since they are persistent and non-biodegradable (1,2). The most widely used methods developed for heavy metal removal include chemical or electrochemical precipitation, membrane filtration, ion exchange, evaporation, air stripping, steam stripping, and adsorption onto activated carbon (3,4). However, conventional methods are expensive and fail in heavy metal removal at low concentrations (5,6).

Biosorption is an attractive method which is advantageous over conventional techniques with the utilization of abundant and low-cost biomasses, namely biosorbents. It is also favored since it demonstrates superior metal binding capacities even at a low heavy metal ion concentration range of 1-100 ppm.

Lead and cadmium ions are not only non-essential to human body but also dangerous for human health. Lead poisoning causes neurodevelopmental problems in children, affects the membrane permeability of organs and haemoglobin synthesis. Lead is also a probable carcinogen because of its enzyme inhibitory effects (7). The presence of cadmium in humans may lead to osteoporosis and causes damages in kidneys (8). Lead-acid

batteries, ammunitions, paints, and ceramic products are major industrial applications of lead, whereas cadmium is mainly profited by the production of alloys, pigments, and batteries (9).

Olive pomace is an abundant agro-industrial waste of olive oil production in the Mediterranean region. There is no industrial use developed for olive pomace and it is normally incinerated or dumped without control. However, it is a promising biomaterial in wastewater treatment as a biosorbent. The utilization of olive pomace in biosorption of lead and cadmium ions is an effective, low-cost and environment-friendly activity adding value to this unrecognized waste (10,11).

The aim of this study was to present olive pomace as a proper biosorbent in lead and cadmium removal and show that it is applicable at its raw form implementing a greener operation without any further process in which chemicals are employed. Batch experiments were conducted and the optimum conditions for biosorption were identified evaluating the process parameters including particle size, solution pH, contact time, initial ion concentration, and incubation temperature. A kinetic modeling was performed in order to explain the adsorption mechanism. Adsorption isotherms were modeled to describe the equilibrium data and a thermodynamic study was carried out in order to have a better understanding of the adsorption characteristics of olive pomace at different temperatures. The surface properties of olive pomace was characterized using ATR-FTIR, SEM, and BET analyses, whereas the surface charge was determined measuring the point of zero charge ( $pH_{pzc}$ ).

## MATERIALS AND METHODS

All the chemicals and reagents used were of analytical grade. Deionized water was used for the preparation of solutions. The stock solutions of 100 ppm  $Pb^{2+}$  and 100 ppm  $Cd^{2+}$  were prepared from  $Pb(NO_3)_2$  (Merck), and  $Cd(NO_3)_2 \cdot 4H_2O$  (Acros Organics), respectively. Their 10, 20, 40, 60, and 80 ppm solutions were prepared using serial dilution. HCl and NaOH used in pH adjustment were purchased from Merck. Olive pomace obtained from an olive oil plant was used in the biosorption experiments as a biosorbent.

### Preparation of olive pomace

Olive pomace was thoroughly washed with tap, and deionized water and then dried at 50°C for 24 h. It was then milled and sieved using a Groschopp & Co mill and Tyler standard sieves. It was finally stored in airtight containers according to two size fraction ranges of 100-500  $\mu m$  and 500-1000  $\mu m$  for the further use.

### Characterization of olive pomace

The attenuated total reflection-Fourier-transform infrared (ATR-FTIR) spectra of pristine, and loaded olive pomace (initial  $Pb^{2+}$  and  $Cd^{2+}$  of 100 ppm) were obtained in transition mode using a Perkin Elmer (Spectrum 100) spectrometer in the region 4000-400  $cm^{-1}$ . The morphological features of olive pomace were observed using a Carl Zeiss (300VP) scanning electron microscope (SEM). The specific surface area of olive pomace was determined from the adsorption data of  $N_2$  at 77 K using a BET analyzer (Micromeritics 3 Flex).  $Pb^{2+}$  and  $Cd^{2+}$  concentrations were specified using atomic absorption spectrometer (AAS) (Perkin Elmer AAnalyst 800).

Batch equilibrium method was applied to determine the point of zero charge ( $pH_{pzc}$ ). Samples of 0.1 g of olive pomace were shaken in closed conical flasks with the addition of 50 mL of 0.01 M NaCl solution at 30°C. The pH was adjusted to a value between 2 and 12 with 0.1 M HCl or NaOH solutions using a pH meter (Hanna Instruments 221). The final pH was measured after 48 h of agitation. Then, the  $pH_{pzc}$  was determined at the point where the curve  $pH_{final}$  versus  $pH_{initial}$  crosses the line  $pH_{initial} = pH_{final}$  (12).

### Adsorption experiments

Experiments were performed in 50 mL PP tubes with 0.025 g of olive pomace and 25 mL of  $Pb^{2+}$  or  $Cd^{2+}$  solutions of desired concentrations. Effect of particle size was investigated comparing the two size fraction ranges of 100-500  $\mu m$  and 500-1000  $\mu m$  in 24 h  $Pb^{2+}$  adsorption experiments with the initial  $Pb^{2+}$  concentrations of 10 to 100 ppm. Effect of solution pH was studied through 24 h of  $Pb^{2+}$  and  $Cd^{2+}$  adsorption experiments with the initial ion concentrations of 100 ppm and the pH variation of 2 to 10. Effect of contact time was observed in  $Pb^{2+}$  and  $Cd^{2+}$  adsorption experiments with the initial ion concentrations of 100 ppm at the optimum pH values varying the agitation time from 0.5 to 24 h. The effect of initial ion concentration was examined with the equilibrium adsorption experiments of  $Pb^{2+}$  and  $Cd^{2+}$  at the optimum pH values in the

initial ion concentration range of 10 to 100 ppm. Effect of incubation temperature on Pb<sup>2+</sup> and Cd<sup>2+</sup> adsorption was investigated at the optimum pH values in the initial ion concentration range of 10 to 100 ppm at 25, 35 and 45°C. All experiments were performed in duplicate. The supernatant liquids were filtered and analyzed using AAS to specify the resulting ion concentrations. The amount of Pb<sup>2+</sup> and Cd<sup>2+</sup> adsorbed was calculated as follows:

$$q_{eq} = \frac{(C_o - C_{eq})V}{m} \quad (\text{Eq. 1})$$

where  $q_{eq}$  is the equilibrium sorption (mg/g),  $C_o$  and  $C_{eq}$  are the initial and equilibrium ion concentrations (mg/L),  $V$  is the volume of solution (L),  $m$  is the amount of olive pomace (g).

### Kinetic models

Kinetic models of "pseudo first order" (13), "pseudo second order" (14), "Weber-Morris intraparticle diffusion" (15), "Elovich" (16), "Bangham pore diffusion" (17), and "Boyd film diffusion" (18) were applied to explain the adsorption mechanism. The respective equations are expressed below:

$$\log(q_{eq} - q_t) = \log q_{eq} - K_1 t \quad (\text{Eq. 2})$$

$$\frac{t}{q_t} = \frac{1}{K_2 q_{eq}^2} + \frac{t}{q_{eq}} \quad (\text{Eq. 3})$$

$$q_t = K_{diff} t^{0.5} + I \quad (\text{Eq. 4})$$

$$q_t = \frac{1}{\beta} \ln(\alpha\beta) + \frac{1}{\beta} \ln(t) \quad (\text{Eq. 5})$$

$$\log\left(\frac{C_o}{C_o - q_t m}\right) = \log\left(\frac{k_o m}{2.303 V}\right) + \alpha \log(t) \quad (\text{Eq. 6})$$

$$\ln\left(1 - \frac{q_t}{q_{eq}}\right) = R^1 t \quad (\text{Eq. 7})$$

where  $q_{eq}$  and  $q_t$  are the amount of Pb<sup>2+</sup> and Cd<sup>2+</sup> adsorbed at equilibrium and at time  $t$  onto olive pomace (mg/g), respectively,  $K_1$  is the rate constant of the pseudo first order model (L/min),  $K_2$  is the rate constant of pseudo second order model (g/(mg.min)),  $K_{diff}$  is the intraparticle diffusion rate constant (mg/

(g.h<sup>0.5</sup>)), the value of  $I$  is the boundary layer thickness (mg/g),  $\alpha$  is the initial adsorption rate (mg/(g.min)),  $\beta$  is the adsorption constant (g/mg),  $C_o$  is the initial ion concentration (mg/L),  $V$  is the volume of solution (mL),  $m$  is the amount of olive pomace (g/L),  $k_o$  is equilibrium constant, and  $R^1$  is liquid film diffusion constant (1/min).

### Isotherm models

Three 2-parameter isotherm models of "Langmuir", "Freundlich" and "Dubinin-Radushkevich", and three 3-parameter isotherm models of "Langmuir-Freundlich", "Radke-Prausnitz" and "Redlich-Peterson" were applied to describe the equilibrium data (19). The respective equations are expressed below:

$$q_{eq} = \frac{q_m K_L C_{eq}}{1 + K_L C_{eq}} \quad (\text{Eq. 8})$$

$$q_{eq} = K_F C_{eq}^{1/n} \quad (\text{Eq. 9})$$

$$q_{eq} = (q_m) \exp(-K_{D-R} \epsilon^2) \quad (\text{Eq. 10})$$

$$q_{eq} = \frac{q_m (K_{L-F} C_{eq})^{m_{L-F}}}{1 + (K_{L-F} C_{eq})^{m_{L-F}}} \quad (\text{Eq. 11})$$

$$q_{eq} = \frac{q_m K_{R-Pr} C_{eq}}{(1 + K_{R-Pr} C_{eq})^{m_{R-Pr}}} \quad (\text{Eq. 12})$$

$$q_{eq} = \frac{K_{R-Pe} C_{eq}}{1 + \alpha_{R-Pe} (C_{eq})^{\beta_{R-Pe}}} \quad (\text{Eq. 13})$$

where  $q_m$  is the monolayer capacity of olive pomace covered with Pb<sup>2+</sup> and Cd<sup>2+</sup> (mg/g),  $K_L$  is the Langmuir constant (L/mg) related to the energy of adsorption,  $K_F$  is the Freundlich constant which predicts the ion amount per gram olive pomace at equilibrium concentration (mg<sup>(1-1/n)</sup>.L<sup>1/n</sup>/g),  $n$  is a strength measure of the process and related to surface heterogeneity. Dubinin-Radushkevich (D-R) model has  $K_{D-R}$  as D-R isotherm constant (mol<sup>2</sup>/kJ<sup>2</sup>) and  $\epsilon = RT \ln\left(1 + \frac{1}{C_{eq}}\right)$ , where  $R =$

8.314 (J/mol.K) and  $T$  in Kelvin. The Langmuir-Freundlich constant,  $K_{L-F}$ , is related to the energy of adsorption and  $m_{L-F}$  values close to zero indicate heterogeneous sorbent, while values closer to unity indicate relatively homogeneous distribution of binding sites. The isotherm constants of Radke-Prausnitz ( $K_{R-Pr}$ )

and Redlich-Peterson ( $K_{R-Pe}$  and  $a_{R-Pe}$ ), as well as  $m_{R-Pe}$  and  $\beta_{R-Pe}$  have similar meanings as explained for Langmuir-Freundlich model (20,21).

Non-linear regression analyses of average relative error (ARE) and root mean square error (RMSE) for the isotherm models were applied using the respective equations below:

$$ARE = \frac{1}{n} \sum_{i=1}^n \left| \frac{q_{exp} - q_{calc}}{q_{exp}} \right| 100 \quad (\text{Eq. 14})$$

$$RMSE = \sqrt{\frac{\sum_{i=1}^n (q_{exp} - q_{calc})^2}{n}} \quad (\text{Eq. 15})$$

where  $n$  is the number of experimental data and  $q_{exp}$  and  $q_{calc}$  stand for the experimental and calculated sorption values (22). A smaller value of ARE and RMSE implies a better modeling.

### Thermodynamic calculations

Thermodynamic parameters were calculated to reveal the thermal properties of olive pomace combining the equations below (23):

$$\Delta G^0 = -RT \ln K_D \quad (\text{Eq. 16})$$

$$K_D = 1000 K_F \quad (\text{Eq. 17})$$

$$\Delta G^0 = \Delta H^0 - T \Delta S^0 \quad (\text{Eq. 18})$$

where  $\Delta G^0$  is the standard free energy change,  $R$  is the universal gas constant,  $T$  is the absolute temperature in Kelvin,  $K_D$  is the distribution coefficient derived from  $K_F$  value of Freundlich isotherm model,  $\Delta H^0$  is the enthalpy change, and  $\Delta S^0$  is the entropy change. Van't Hoff equation finally yields as:

$$\ln K_D = -\frac{\Delta G^0}{RT} = -\frac{\Delta H^0}{RT} + \frac{\Delta S^0}{R} \quad (\text{Eq. 19})$$

## RESULTS AND DISCUSSION

### Characterization of olive pomace

The point of zero charge ( $pH_{PZC}$ ) measurement (Figure 1) revealed that the surface of olive pomace is neutral at  $pH$  6.2, acidic (positively charged) below and basic (negatively charged) above this value which is capable of  $Pb^{2+}$  and  $Cd^{2+}$  adsorption. This property determines how easily heavy metal ions are captured on the surface of a biosorbent depending on the  $pH$  of the environment and the charge of the ions.

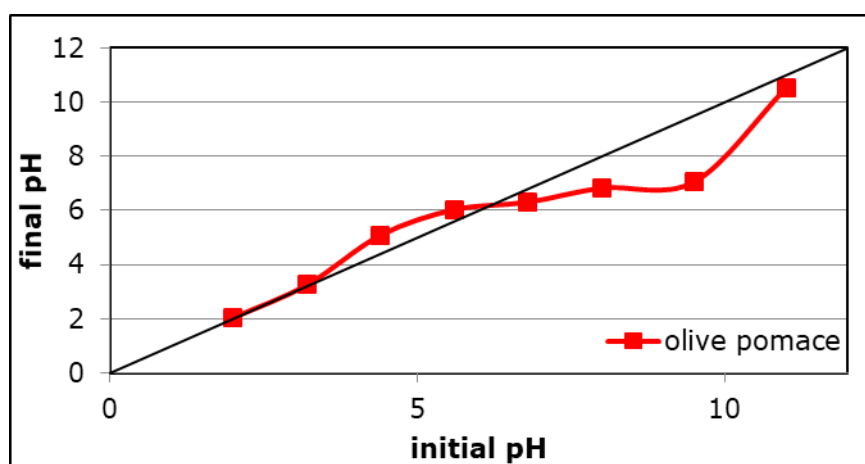


**Figure 1.** Plot of final pH vs. initial pH for point of zero charge measurement.

The BET surface area of olive pomace was determined as around  $0.15 \text{ m}^2/\text{g}$  using the BET analyzer. The small surface area indicated that the surface has a non-porous character. SEM analysis (Figure 2) also confirmed this non-

porous structure illustrated with a magnification of  $500\times$ . Despite not having a large surface area, olive pomace was capable of  $Pb^{2+}$  and  $Cd^{2+}$  uptake.

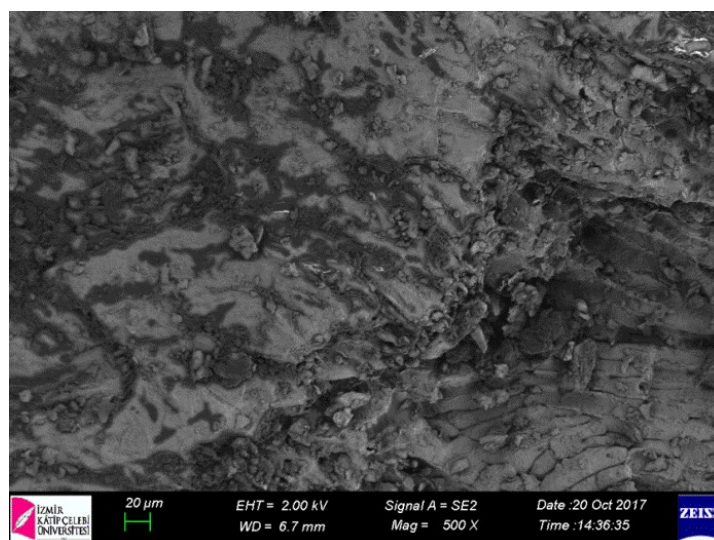


**Figure 2.** SEM micrograph of olive pomace with a magnification of 500x.

Surface functional groups of the pristine and  $\text{Pb}^{2+}/\text{Cd}^{2+}$  adsorbed olive pomace were analyzed using ATR-FTIR spectroscopy (Figure 3) to understand the nature of the surface functional groups and their interactions with  $\text{Pb}^{2+}$  and  $\text{Cd}^{2+}$  ions. The strong broad band at  $3334\text{ cm}^{-1}$  is the characteristic peak ascribed to the -OH stretching vibrations. The peaks at  $2923$  and  $2855\text{ cm}^{-1}$  are due to the C-H stretching vibrations of CH,  $\text{CH}_2$  and  $\text{CH}_3$  groups (10). The peak around  $1724\text{ cm}^{-1}$  shows the carbonyl (C=O) stretching vibration of the carboxyl groups and the peak at  $1655\text{ cm}^{-1}$  are initiated by the asymmetric stretching vibrations of the carboxylic groups (24). The peaks in the range of  $1000$  to  $1300\text{ cm}^{-1}$  are generally ascribed to the C-O stretching vibrations in carboxylic acids and alcohols

(25). The shifts on the peak locations from  $3334, 1724\text{ cm}^{-1}$  to  $3328, 1730\text{ cm}^{-1}$  after  $\text{Pb}^{2+}$  adsorption and to  $3313, 1718\text{ cm}^{-1}$  after  $\text{Cd}^{2+}$  adsorption indicate the interactions with the related surface functional groups. It can be concluded from these results that the main groups (-OH and -COO) are promoting the  $\text{Pb}^{2+}$  and  $\text{Cd}^{2+}$  adsorption. Besides, the peak shifts from  $2993$  and  $2855\text{ cm}^{-1}$  to the single peak at  $2877\text{ cm}^{-1}$  after  $\text{Cd}^{2+}$  adsorption point out coordinative interaction of  $\text{Cd}^{2+}$  ions with the CH groups of the olive pomace surface. The largest peak shift identified for C-H stretching and the minor signal attenuation corresponding to  $\text{CH}_2$  wagging was attributed to steric strain introduced by accommodation of the  $\text{Cd}^{2+}$  ions in coordination complex formation (26).

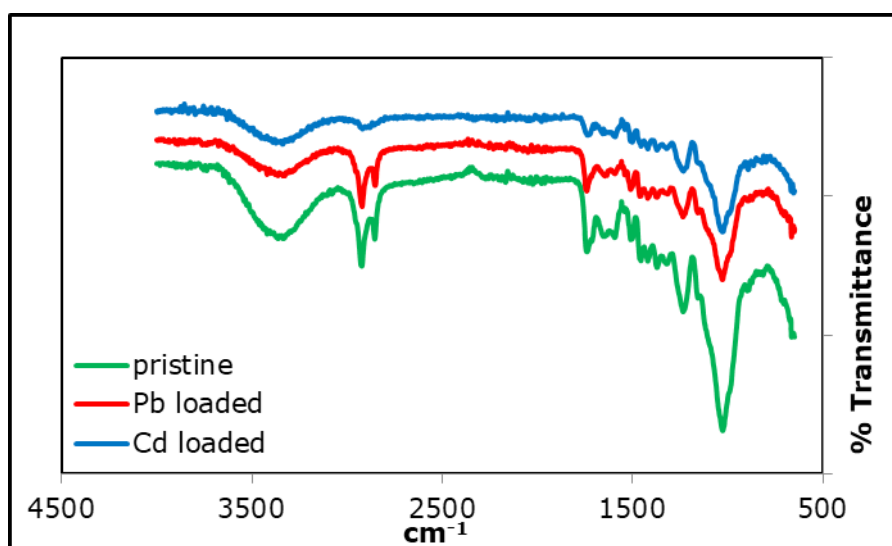


**Figure 3.** ATR-FTIR spectra of pristine, and  $Pb^{2+}/Cd^{2+}$  loaded olive pomace.

#### Effect of particle size

Effect of particle size was studied to choose a particle size with a higher uptake capacity. The results (Figure 4) revealed the insignificant difference between sorption capacities of the two size fraction ranges. Taking into account

of the inevitable pressure drop created by finer solids in continuously operated systems, olive pomace fraction in the range of 500-1000  $\mu m$  was utilized throughout the study to exhibit its ease of use in such potential technologies.

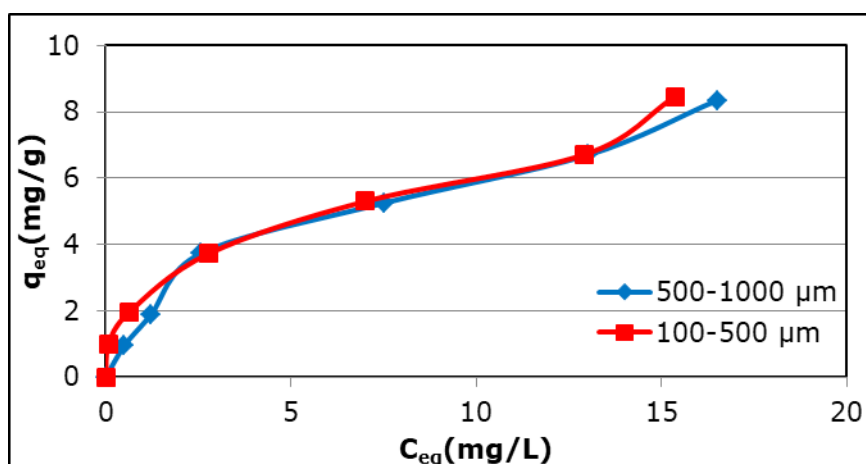


**Figure 4.** Plot of  $q_{eq}$  vs.  $C_{eq}$  for  $Pb^{2+}$  adsorption with different size fraction ranges.

#### Effect of solution pH

To study the pH dependency of the adsorption process, experiments were carried out at the pH range of 2-10. Solution pH affects not only the surface charge of the olive pomace but also the hydrolysis accompanying the precipitation of metal hydroxides. Metal hydroxides are amphoteric, that is, they are increasingly soluble at both low and high pH values, and the point of minimum solubility

(optimum pH for precipitation) emerges at a pH different for each metal ion. According to Figure 5, the true adsorption of  $Pb^{2+}$  occurs until pH 6 and that of  $Cd^{2+}$  occurs until pH 7, whereas the formation of  $Pb(OH)^+$  and  $Cd(OH)^+$  ions begins at a pH higher than 6 and 7 for  $Pb^{2+}$  and  $Cd^{2+}$ , respectively. The figure further shows that no adsorption occurs due to the reduced attraction by the less negative surface charge and competing  $H^+$  ions at a pH

lower than 2 for  $Pb^{2+}$  and 3 for  $Cd^{2+}$  (27). Therefore, the optimum pH values were selected as 5.5 and 6 for  $Pb^{2+}$  and  $Cd^{2+}$ , respectively.

At the optimum pH conditions lower than the  $pH_{PZC}$  of 6.2, the adsorption is expected to take place by means of the ion exchange of  $Pb^{2+}$  and  $Cd^{2+}$  with  $H^+$ , as well as with  $Na^+$  ions present on the surface.

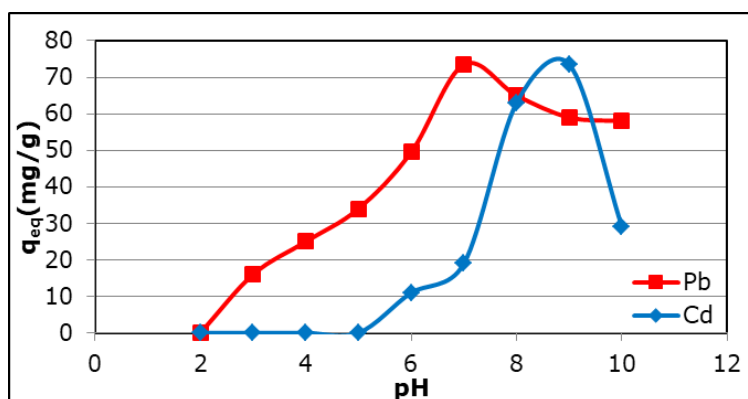


**Figure 5.** Plot of  $q_{eq}$  vs. pH for  $Pb^{2+}$  and  $Cd^{2+}$  adsorption.

#### Effect of contact time

Effect of contact time on  $Pb^{2+}$  and  $Cd^{2+}$  adsorption was studied to verify the sorption equilibrium. As seen in Figure 6, both  $Pb^{2+}$  and

$Cd^{2+}$  adsorption onto olive pomace are fast during the first four hours and then the equilibrium is attained slowly.

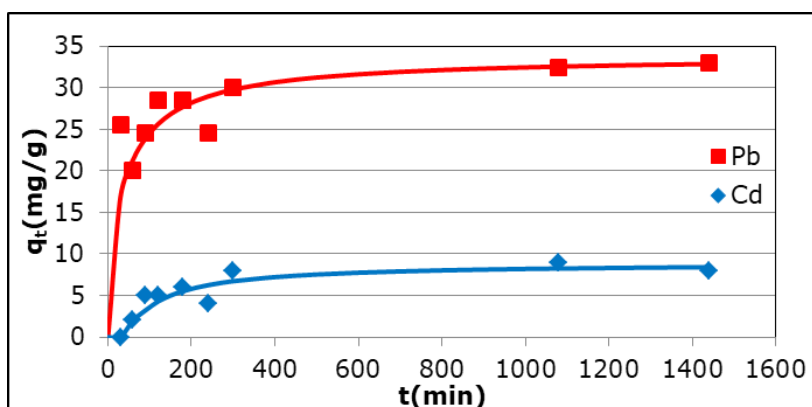


**Figure 6.** Plot of  $q_t$  vs. time with the pseudo second order model fitting for  $Pb^{2+}$  and  $Cd^{2+}$  adsorption.

#### Effect of initial ion concentration

Maximum sorption for  $Pb^{2+}$  and  $Cd^{2+}$  was obtained in the effect of initial ion concentration experiments at 25°C as 33 and 8 mg/g, respectively. The supremacy acquired by  $Pb^{2+}$  proves that the affinity of olive pomace towards  $Pb^{2+}$  is greater than that towards  $Cd^{2+}$ . Hence, a selective removal might be carried out from a bimetallic mixture of these ions.

#### Effect of incubation temperature

A direct proportion between the sorption capacity and incubation temperature for both  $Pb^{2+}$  and  $Cd^{2+}$  was indicated by the effect of incubation temperature experiments. This behavior is exhibited in Figure 7 with the best fitting isotherm models which are the Redlich-Peterson and Langmuir-Freundlich models for  $Pb^{2+}$  and  $Cd^{2+}$  adsorption, respectively. The modeling study is discussed further in the isotherm modeling section.

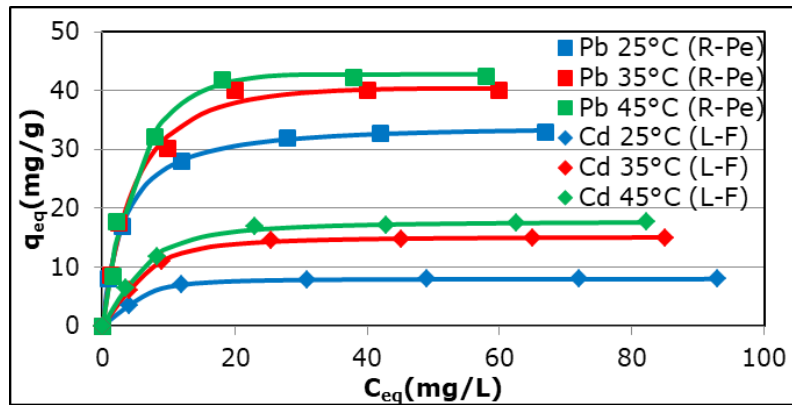


Figure 7. Plot of  $q_{eq}$  vs.  $C_{eq}$  for  $Pb^{2+}$  and  $Cd^{2+}$  adsorption at different temperatures.

**Kinetic modeling**

Linear plots of the pseudo first order (P-F-O), pseudo second order (P-S-O), Weber-Morris intraparticle diffusion, Elovich, Bangham pore diffusion, and Boyd film diffusion models were applied and compared. Based on the coefficient of determination ( $R^2$ ) values close to unity given in Table 1 and the graphical harmony seen in Figure 8, pseudo second order model is the most suitable kinetic model for both  $Pb^{2+}$  and  $Cd^{2+}$  adsorption. Since pseudo second order model originates from

chemical reaction kinetics, the three consecutive steps of adsorption, namely bulk diffusion, film diffusion and pore diffusion are not addressed in the rate-limiting step determination. In this regard, Weber-Morris intraparticle diffusion model is useful to find out the rate-limiting step. As seen in Figure 8c, there are two linear portions: The first controlled by surface diffusion process, and the latter by pore diffusion, indicating that external diffusion is the rate-limiting step (17,18).

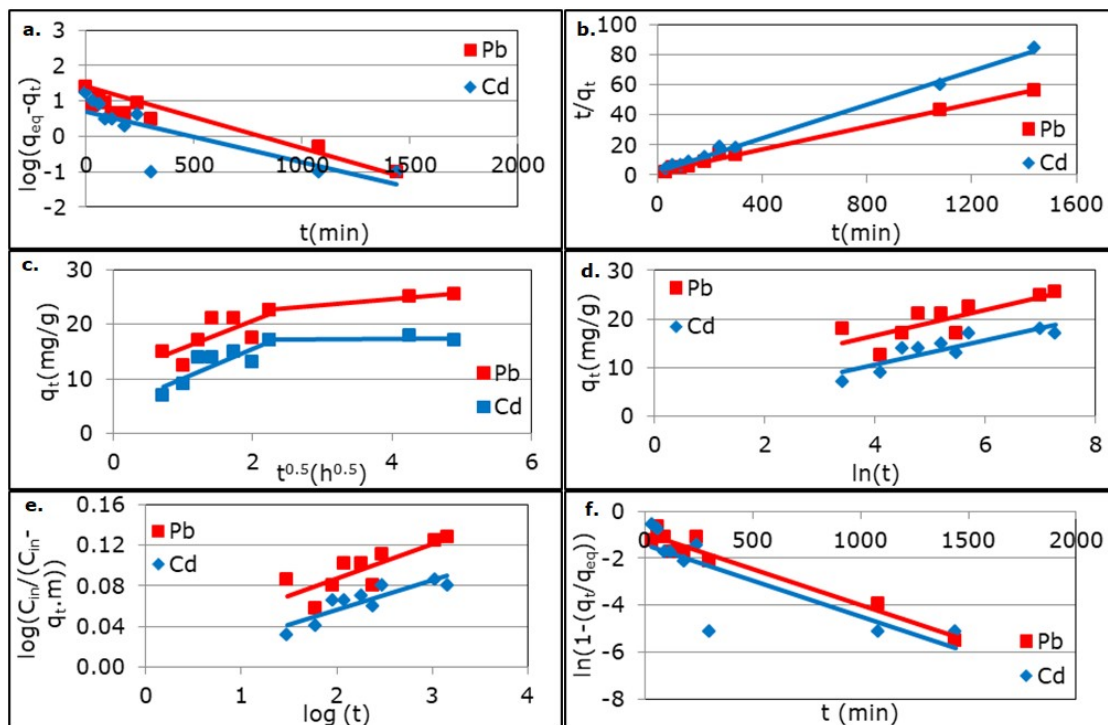


Figure 8. Kinetic models of a) P-F-O, b) P-S-O, c) Weber-Morris, d) Elovich, e) Bangham, and f) Boyd.

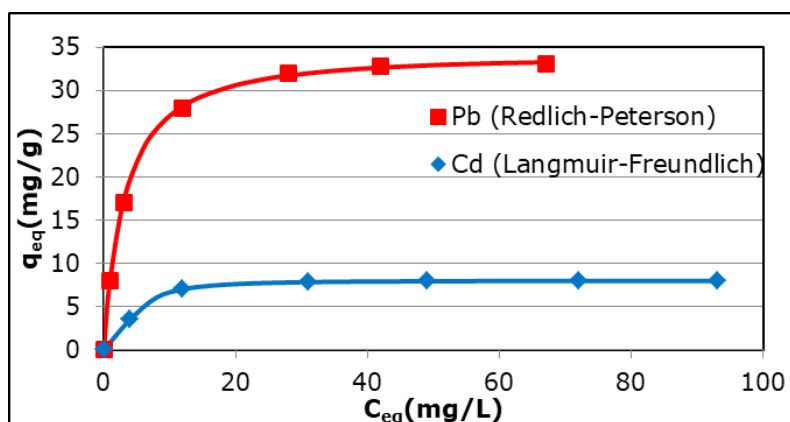
**Table 1.** Kinetic parameters for Pb<sup>2+</sup> and Cd<sup>2+</sup> adsorption.

Kinetic model	parameter	Pb <sup>2+</sup>	Cd <sup>2+</sup>
P-F-O	K <sub>1</sub> (L/min)	0.0017	0.002
	q <sub>eq</sub> (mg/g)	25.119	16.596
	R <sup>2</sup>	0.774	0.412
P-S-O	K <sub>2</sub> (g/(mg.min))	0.0007	0.0013
	q <sub>eq</sub> (mg/g)	26.316	17.921
	R <sup>2</sup>	0.996	0.996
Weber-Morris	K <sub>diff</sub> (mg/(g.h <sup>0.5</sup> ))	1.155	5.410
	I (mg/g)	19.954	4.743
	R <sup>2</sup>	0.993	0.718
Elovich	α (mg/g.min)	24.441	2.929
	β (g/mg)	0.375	0.392
	R <sup>2</sup>	0.646	0.764
Bangham	A	0.033	0.029
	k <sub>o</sub>	60.344	57.271
	R <sup>2</sup>	0.661	0.771
Boyd	R <sup>1</sup> (min <sup>-1</sup> )	0.003	0.003
	R <sup>2</sup>	0.949	0.643

**Isotherm modeling**

Parameters of the isotherm models as well as their corresponding average relative errors (ARE) and root mean square errors (RMSE) were estimated using solver add-in function of

Microsoft Excel. The best simulation was selected considering the graphical harmony of the equilibrium data with the models and also the lowest values of ARE and RMSE.

**Figure 9.** Isotherm modeling for Pb<sup>2+</sup> and Cd<sup>2+</sup> adsorption at room temperature.

Redlich-Peterson and Langmuir-Freundlich models were the best resulting models for Pb<sup>2+</sup> and Cd<sup>2+</sup> adsorption, respectively, as shown in Figure 9, and the parameters of these models are presented in Table 2 (see also Figure 7).

The Redlich-Peterson model approximates the Henry's law at low Pb<sup>2+</sup> concentrations, and at high concentrations it predicts a monolayer adsorption capacity characteristic of the Langmuir isotherm. On the other hand, the

Langmuir-Freundlich model reduces to the Freundlich isotherm at low  $\text{Cd}^{2+}$  concentrations, while it behaves like the Langmuir isotherm at high concentrations. The  $m$  and  $\beta$  parameters are often regarded as the heterogeneity factors and the calculated values (Table 2) greater than unity confirms the heterogeneous nature of the olive pomace. (19,20,21). The steep slope observed for  $\text{Pb}^{2+}$  adsorption proves that olive pomace is very

effective in the removal of this ion at low concentrations, whereas  $\text{Cd}^{2+}$  adsorption appears to be less favorable. This behavior is in line with the best fitting models to the equilibrium data of  $\text{Pb}^{2+}$  and  $\text{Cd}^{2+}$  adsorption at low concentrations corresponding to the steep and linear portion for Henry's isotherm and the less steep portion for Freundlich isotherm, respectively.

**Table 2.** Isotherm parameters for  $\text{Pb}^{2+}$  and  $\text{Cd}^{2+}$  adsorption at different temperatures.

heavy metal ion	T (K)	isotherm model	$q_m$	K	m	$\alpha$	$\beta$	ARE	RMSE
$\text{Pb}^{2+}$	298	Redlich-Peterson		10.69		0.28	1.02	0.46	0.24
	308			8.64		0.13	1.10	0.65	1.47
	318			8.00		0.08	1.19	1.68	1.88
$\text{Cd}^{2+}$	298	Langmuir-Freundlich	8.00	0.22	2.00			0.17	0.03
	308		15.00	0.20	1.76			0.04	0.09
	318		17.80	0.20	1.62			0.73	0.36

### Thermodynamic parameters

Thermodynamic behavior of olive pomace was evaluated with the calculated thermodynamic parameters. The slope and intercept of the plot

$\ln K_D$  vs.  $1/T$  given in Figure 10 were used in the calculation of the enthalpy and entropy changes in Van't Hoff equation.

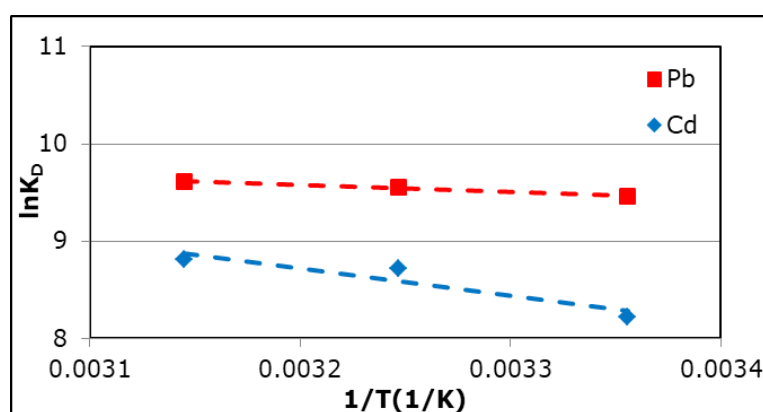


**Figure 10.** Plot of  $\ln K_D$  vs.  $1/T$  for  $\text{Pb}^{2+}$  and  $\text{Cd}^{2+}$  adsorption at different temperatures.

The negative values of  $\Delta G^\circ$  state that the adsorption phenomenon is feasible and spontaneous. The positive values of  $\Delta H^\circ$  denote an endothermic process, indicating the increased amount of metal ions adsorbed with the increase in temperature. The magnitude of  $\Delta H^\circ$  also gives an idea about the type of adsorption suggesting that  $\text{Pb}^{2+}$  and  $\text{Cd}^{2+}$

adsorption can be attributed to a physical adsorption process. Besides, the positive values of  $\Delta S^\circ$  indicates an increased disorder at the solid-solution interface reflecting the affinity of olive pomace towards  $\text{Pb}^{2+}$  and  $\text{Cd}^{2+}$ , and the adsorption mechanism based on the ion exchange (28).

**Table 3.** Thermodynamic parameters for Pb<sup>2+</sup> and Cd<sup>2+</sup> adsorption at different temperatures.

heavy metal ion	T (K)	K <sub>D</sub>	lnK <sub>D</sub>	ΔG° (kJ/mol)	ΔH° (kJ/mol)	ΔS° (J/mol.K)
Pb <sup>2+</sup>	298	12876.91	9.46	-23.446	6.018	98.896
	308	14058.42	9.55	-24.457		
	318	14999.36	9.62	-25.423		
Cd <sup>2+</sup>	298	3721.43	8.22	-20.370	23.253	146.913
	308	6124.18	8.72	-22.329		
	318	6686.97	8.81	-23.287		

## CONCLUSION

This study introduced olive pomace as a proper biosorbent in the removal of lead and cadmium ions from aqueous solutions. Its application at its raw form offers an economical practice. The feasible and spontaneous behavior of the process was verified by the thermodynamic calculations. The endothermic process indicated the increased metal uptake with an increase in temperature. The adsorption kinetics was well explained with the pseudo second order model. The Redlich-Peterson and Langmuir-Freundlich isotherms were the best fitting models for Pb<sup>2+</sup> and Cd<sup>2+</sup> adsorption, respectively. The Pb<sup>2+</sup> amount adsorbed was four times higher than that of Cd<sup>2+</sup>. The supremacy acquired by Pb<sup>2+</sup> proves that the affinity of olive pomace towards Pb<sup>2+</sup> is greater than that towards Cd<sup>2+</sup>. Hence, a selective removal might also be carried out from a bimetallic mixture of these ions.

## ACKNOWLEDGEMENTS

The authors are grateful to Ege University Research Fund for the financial support under Project No 14-MUH-052 and Van Yüzüncü Yıl University for holding the 13th National Chemical Engineering Congress (September 3-6, 2018) where this study was orally presented.

## REFERENCES

1. Yakub A, Mughal MS, Mukhtar H, Spirogyra as an efficient biosorbent of cadmium: A mechanistic approach. *Pakistan Journal of Botany*. 2016; 48(6): 2563-70.
2. Lawal OS, Ayanda OS, Rabiou OO, Adebowale KO, Application of black walnut (*Juglannigra*) husk for the removal of lead (II) ion from aqueous solution. *IWA Publishing*. 2017; 1-10.
3. Verma A, Kumar S, Kumar S, Biosorption of lead ions from the aqueous solution by *Sargassumfilipendula*: Equilibrium and kinetic studies. *Journal of Environmental Chemical Engineering*. 2016; 4: 4587-99.
4. Husein DZ, Aazam E, Battia M, Adsorption of cadmium (II) onto watermelon rind under microwave radiation and application into surface water from Jeddah, Saudi Arabia. *Arabian Journal for Science and Engineering*. 2017; 42: 2403-15.
5. Mohammed A, Biosorption of lead, cadmium, and zinc onto sunflower shell: Equilibrium, kinetic, and thermodynamic studies. *Iraqi Journal of Chemical and Petroleum Engineering*. 2015; 16(1); 91-105.
6. Liu X, Chen ZQ, Han B, Su CL, Han Q, Chen, WZ, Biosorption of copper ions from aqueous solution using rape straw powders: Optimization, equilibrium and kinetic studies. *Ecotoxicology and Environmental Safety*. 2018; 150: 251-9.
7. Morosanu I, Teodosiu C, Paduraru C, Ibanescu D, Tofan, L, Biosorption of lead ions from aqueous effluents by rapeseed biomass. *New Biotechnology*. 2017; 39: 110-24.
8. Nishikawa E, da Silva MGC, Vieira MGA, Cadmium biosorption by alginate extraction waste and process overview in life cycle assessment context. *Journal of Cleaner Production*. 2018; 178: 166-75.
9. Tchounwou PB, Yedjou CG, Patlolla AK, Sutton DJ, Heavy Metals Toxicity and the Environment. *EXS*. 2012; 101: 133-64.
10. Martin-Lara MA, Pagnanelli F, Mainelli S, Calero M, Toro L, Chemical treatment of olive pomace: Effect on acid-basic properties and metal

- biosorption capacity. *Journal of Hazardous Materials*. 2008; 156(1-3): 448-57.
11. Martin-Lara MA, Blazquez G, Ronda A, Perez A, Calero M, Development and characterization of biosorbents to remove heavy metals from aqueous solutions by chemical treatment of olive stone. *Industrial & Engineering Chemistry Research*. 2013; 52: 10809-19.
  12. Shouman MA, Fathy NA, Khedr SA, Attia AA, Comparative biosorption studies of hexavalent chromium ion onto raw and modified palm branches. *Advances in Physical Chemistry*. 2013; 1-9.
  13. Lagergren S, About the Theory of so Called Adsorption of Soluble Substances. *Kungliga Svenska Vetenskapsakademiens Handlingar*. 1898; 24: 1-39.
  14. Febrianto J, Kosasih AN, Sunarso J, Ju YH, Indraswati N, Ismadji S, Equilibrium and kinetic studies in adsorption of heavy metals using biosorbent: A summary of recent studies. *Journal of Hazardous Materials*. 2009; 162: 616-45.
  15. Weber JW, Morris JC, Kinetics of adsorption on carbon from solution. *Journal of the Sanitary Engineering Division*. 1963; 89: 31-60.
  16. Hashem A, Adam E, Hussein HA, Sanousy MA, Ayoub A, Bioadsorption of Cd (II) from contaminated water on treated sawdust: Adsorption mechanism and optimization. *Journal of Water Resource and Protection*. 2013; 5: 82-90.
  17. Chakrapani C, Babu CS, Vani KNK, Rao KS, Adsorption kinetics for the removal of fluoride from aqueous solution by activated carbon adsorbents derived from the peels of selected citrus fruits. *E-Journal of Chemistry*. 2010; 7(1): 419-27.
  18. Qiu H, Pan B-C, Zhang Q-J, Zhang W-M, Zhang Q-X, Critical review in adsorption kinetic models. *Journal of Zhejiang University SCIENCE A*. 2009; 10(5): 716-24.
  19. Foo KY, Hameed BH, Insights into the modeling of adsorption isotherm systems. *Chemical Engineering Journal*. 2010; 156: 2-10.
  20. Montazer-Rahmati MM, Rabbani P, Abdolali A, Keshtkar AR, Kinetics and equilibrium studies on biosorption of cadmium, lead, and nickel ions from aqueous solutions by intact and chemically modified brown algae. *Journal of Hazardous Materials*. 2011; 185: 401-407.
  21. Saadi R, Saadi Z, Fazaeli R, Fard NE, Monolayer and multilayer adsorption isotherm models for sorption from aqueous media. *Korean Journal of Chemical Engineering*. 2015; 32(5): 787-799.
  22. Ghaffari HR, Pasalari H, Tajvar A, Dindarloo K, Goudarzi B, Alipour V, Ghanbarnejad A, Linear and nonlinear two-parameter adsorption isotherm modeling: A case-study. *The International Journal of Engineering and Science*. 2017; 6(9): 1-11.
  23. Tran HN, You SJ, Hosseini-Bandegharaei A, Chao HP, Mistakes and inconsistencies regarding adsorption of contaminants from aqueous solutions: A critical review. *Water Research*. 2017; 120: 88-116.
  24. Almasi A, Omidi M, Khodadadian M, Khamutian R, Gholivand MB, Lead(II) and cadmium(II) removal from aqueous solution using processed walnut shell: Kinetic and equilibrium study. *Toxicological & Environmental Chemistry*. 2012; 94(4): 660-671.
  25. Feng N, Guo X, Liang S, Adsorption study of copper (II) by chemically modified orange peel. *Journal of Hazardous Materials*. 2009; 164(2-3): 1286-1292.
  26. Moyo M, Pakade VE, Modise SJ, Biosorption of lead(II) by chemically modified *Mangifera indica* seed shells: Adsorbent preparation, characterization and performance assessment. *Process Safety and Environmental Protection*. 2017; 111: 40-51.
  27. Pehlivan E, Yanik BH, Ahmetli G, Pehlivan M, Equilibrium isotherm studies for the uptake of cadmium and lead ions onto sugar beet pulp. *Bioresource Technology*. 2008; 99(9): 3520-3527.
  28. Tadashi M, editor. *Thermodynamics. Chapter 16: Insight Into Adsorption Thermodynamics*, InTech; 2011.



## EFFECT OF MoS<sub>2</sub>-DOPED CONDUCTING POLYMERS TO THE CORROSION OF MILD STEEL

Gülden Asan<sup>a</sup> , Abdurrahman Asan<sup>b\*</sup> 

<sup>a</sup> Hittite University, Technical Sciences Vocational School, Corum, 19030

<sup>b</sup> Hittite University, Faculty of Engineering, Corum, 19030

**Abstract:** One of the most common ways of protecting metals from corrosion is to form a film on metal surfaces or to coat them with suitable materials. Thus, metals are protected from corrosive components in their environment. However, in the case of openings at the micro level that may occur in the formation of the coating or in case of scratches and similar openings that may occur after the coating, water and air will reach the metal surface and initiate corrosion. In this study, the effect of polypyrrole (PPy), polyaniline (PANI) and MoS<sub>2</sub>-doped PPy and PANI coatings on the corrosion rate of steel were investigated. Corrosion resistances of these coatings were determined by measuring corrosion rates by Tafel Polarization method in 0.1 M NaCl medium. Because of the experiments, it was determined that these homogeneous and adhering coatings were effective against corrosion. The best protection against corrosion was found as 96.7%, 89.0%, 69.5% and 45.2% for PPy + MoS<sub>2</sub>, PPy, PANI + MoS<sub>2</sub> and PANI coatings, respectively. MoS<sub>2</sub> additive yielded positive results for both coatings. Better protection of PPy than PANI can be explained by the fact that the oxidation potential of pyrrole (0.6 V) is lower than that of the oxidation potential of aniline.

**Keywords:** Corrosion, conducting polymers, MoS<sub>2</sub>, Tafel polarization, mild steel.

**Submitted:** May 31, 2019. **Accepted:** September 23, 2019.

**Cite this:** Asan G, Asan A. EFFECT OF MoS<sub>2</sub>-DOPED CONDUCTING POLYMERS TO THE CORROSION OF MILD STEEL. JOTCSB. 2019;2(2):133-6.

**\*Corresponding author. E-mail:** [asanabdurrahman@hotmail.com](mailto:asanabdurrahman@hotmail.com).

### INTRODUCTION

Corrosion affects our life in many ways. Everything that is made of metal is affected by corrosion and as a result, corrosion affects our economy directly or indirectly. A large part of the steel produced is lost or becomes unavailable every year due to corrosion (1, 2). Metal lost because of corrosion causes economic losses much higher than its own cost. Because, besides the raw materials, production costs should be considered as losses (3). In addition, depending on the state of the substance released into the environment, it has a negative effect on the life of living things. Various measures are taken to protect metals from corrosion (4).

One of the effective methods to prevent corrosion is to prevent the metal from interacting with the environment (5). The most common way is to create a film on the metal or to coat it. In conductive polymer coatings on the metal surface, generally electrochemical methods are preferred to improve the film thickness by altering the current density, monomer concentration, electrolyte solution quality and pH. Besides the type of metal to be protected, one of the metallic or organic coatings can be made considering the condition of the environment (6, 7).

Organic coatings provide long-term protection from corrosion. However, due to scratches and imperfections in the coating, the metal surface is exposed and the protection deteriorates. For the

first time in 1985, De Berry covered steel with PANI and showed corrosion protection in the sulfuric acid medium and accelerated the studies about corrosion protection with conductive polymers (8). With the discovery of the properties of conductive polymers repairing the defects in the coating itself, studies on this subject have intensified (9-11). Due to their redox properties, conductive polymers repair the coating by closing these openings and provide excellent protection (12-16).

The aim of this study was to investigate the effects of MoS<sub>2</sub>-doped PPy, PANI coatings in addition to PPy, and PANI coatings on the corrosion protection of mild steel. In this study, protection behavior of conductive polymers, mainly; PPy and PANI on mild steel surface are examined. In addition, the protective effect of the two layer coating system PPy + MoS<sub>2</sub> and PANI + MoS<sub>2</sub> on mild steel is first investigated in NaCl. The Tafel polarization method is used to illustrate the influence of these films on the protection of mild steel in sodium chloride media.

## EXPERIMENTAL

In this study, a 3-necked 500 mL reaction flask was used as the corrosion cell. The working electrode was submerged into the middle neck. The reference electrode was placed in one of the neck and the counter electrode was placed in the other. A platinum plate was used as the counter electrode and Saturated Calomel Electrode (SCE) was used as the reference electrode. Prior to each test, the working electrode was sanded with 2000 sandpaper, then cleaned by distilled water, and immersed into ethyl alcohol to accelerate drying. The percentage coating efficiency was calculated according to the following equation. Coatings were obtained on the surface of the mild steel by cyclic voltammetry in 0.1 M H<sub>2</sub>C<sub>2</sub>O<sub>4</sub>. CVs and Tafel Polarization curves were obtained at 100 mV / s and at 2 mV / s scan rate respectively (9).

$$\text{Coating Efficiency \%} = \frac{CR(\text{uncoated}) - CR(\text{coated})}{CR(\text{uncoated})} \quad (\text{Eq. 1})$$

## RESULTS AND DISCUSSION

PPy and MoS<sub>2</sub>-doped PPy coating on the mild steel surface was formed with 10 cycles between

0.0 V and 1.0 V in 0.1 M H<sub>2</sub>C<sub>2</sub>O<sub>4</sub> medium. The resulting voltammograms are given in Figure 1. PPy formation can be understood from the increase in current at 0.6 V.

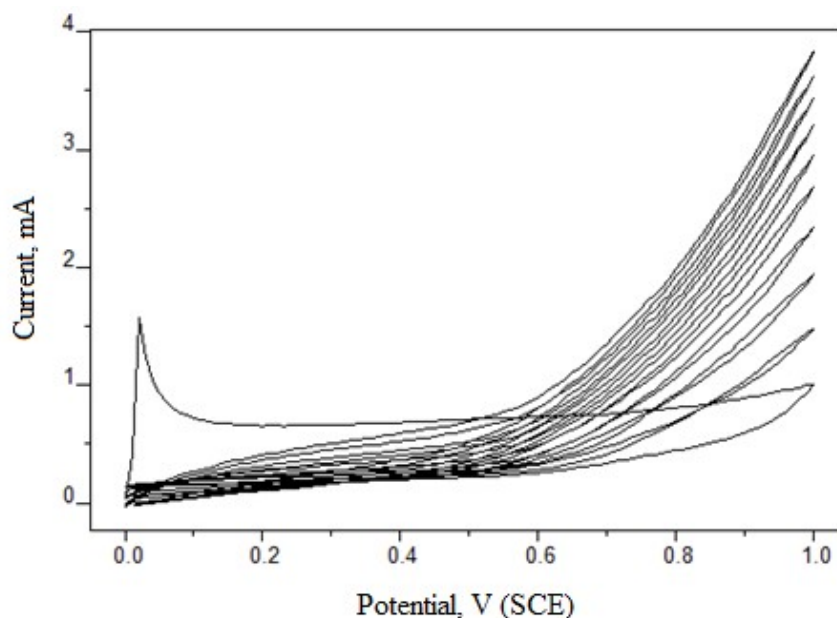


**Figure 1.** PPy coating curves obtained on Mild Steel surface.

PANI coating curves obtained at scan rate 100 mV / s in the range of 0.0 V to 1.2 V. It can be seen in Figure 2. It shows the aniline oxidation

potential is higher than that of pyrrole. After about 1.0 V a big increase in potential has occurred.

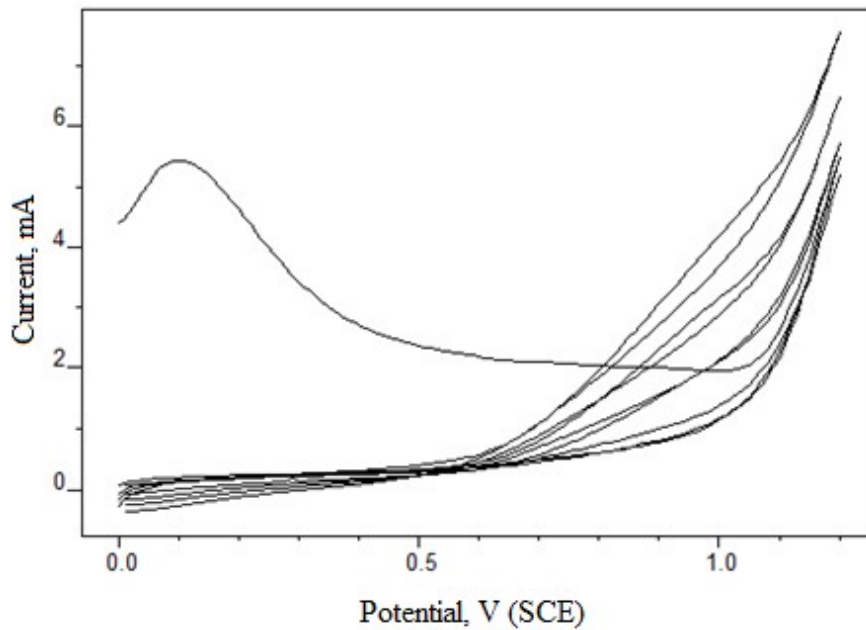


**Figure 2.** PANI coating obtained curves on the surface of steel.

In Figure 3, Tafel polarization coating curves obtained are given collectively to see the effect of the coating on mild steel corrosion. All of the coatings on the steel surface have increased the

corrosion potential of the steel to more positive potentials and reduced the corrosion current density.

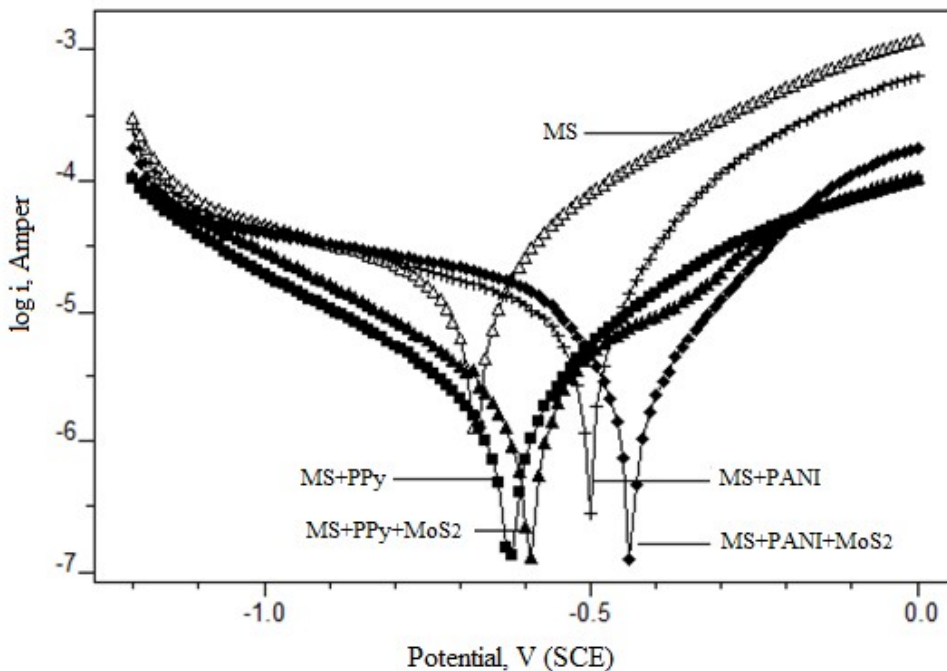


**Figure 3.** Tafel Polarization curves for all coatings on the mild steel surface.

PPy coatings have shifted their corrosion potential to positive values, approximately 100 mV, while PANI coatings shifted to more than 200 mV. The doped MoS<sub>2</sub> positively affected the corrosion potential for both coatings. This

contribution of MoS<sub>2</sub> can be explained by closing gaps in the micro level that can occur in the coating and forming a more stable impermeable layer. It is seen that PANI coatings decreased the cathodic reaction rate more than PPy coatings.

The lower corrosion current density of the PPy coating compared to the PANI coating showed that the PPy coating is more effective on the

anodic reaction. MoS<sub>2</sub> added a positive contribution to the decrease of anodic current in both coatings.

**Table 1.** Corrosion Parameters.

	<b>Ecor (mV)</b>	<b>Rp (ohm)</b>	<b>Corrosion Rate(mm/year)</b>	<b>Coating Efficiency %</b>
Mild Steel (MS)	-685	9289	0.210	-
MS+PANI	-497	11525	0.115	45.2
MS+PANI+MoS <sub>2</sub>	-432	12047	0.064	69.5
MS+PPy	-637	12825	0.023	89.0
MS+PPy+MoS <sub>2</sub>	-591	13267	0.007	96.7

Corrosion potentials, polarization resistance, and corrosion rate calculated from corrosion current density, and coating efficiency are given in Table 1. Polarization resistance results for mild steel and MoS<sub>2</sub> doped PPy / PANI coatings are compatible with corrosion rates. The coating efficiency was determined for PANI, PANI+MoS<sub>2</sub>, PPy, and PPy+MoS<sub>2</sub> 45.2, 69.5, 89.0 and 96.7 respectively.

#### ACKNOWLEDGMENTS

This article was submitted as an oral presentation to the 13th National Chemical Engineering Congress.

#### REFERENCES

1. Cost of corrosion in the USA. *Anti-Corros Method M.* 2000;47(3):141-.
2. Biezma MV, San Cristobal JR. Methodology to study cost of corrosion. *Corros Eng Sci Techn.* 2005;40(4):344-52.
3. Bhaskaran R, Palaniswamy N, Rengaswamy NS, Jayachandran M. A review of differing approaches used to estimate the cost of corrosion (and their relevance in the development of modern corrosion prevention and control strategies). *Anti-Corros Method M.* 2005;52(1):29-41.
4. Abed KM, Pynn CR. Effect of Volatile Corrosion Inhibitors on Cathodic Protection. *Mater Performance.* 2018;57(12):24-9.
5. Al-Amiery AA, Ahmed MHO, Abdullah TA, Gaaz TS, Kadhum AAH. Electrochemical studies of novel corrosion inhibitor for mild steel in 1 M hydrochloric acid. *Results Phys.* 2018;9:978-81.
6. Bandeira MCE, Prochnow FD, Costa I, Franco CV. Corrosion resistance of Nd-Fe-B magnets coated with polypyrrole films. *Mater Sci Forum.* 2006;530-531:111-+.
7. Riviere JP, Delafond J, Misaelides P, Noli F. Corrosion protection of an AISI 321 stainless steel by SIC coatings. *Surf Coat Tech.* 1998;100(1-3):243-6.
8. DeBerry DW. Modification of the electrochemical and corrosion behavior of stainless steels with an electroactive coating. *J Electrochem Soc.* 1985;132(5):1022-6.
9. Fenelon AM, Breslin CB. The electrochemical synthesis of polypyrrole at a copper electrode: corrosion protection properties. *Electrochim Acta.* 2002;47(28):4467-76.
10. Asan A, Kabasakaloglu M. Electrochemical and corrosion behaviors of mild steel coated with polypyrrole. *Mater Sci.* 2003;39(5):643-51.
11. Attarzadeh N, Raeissi K, Golozar MA. Effect of saccharin addition on the corrosion resistance of polypyrrole coatings. *Prog Org Coat.* 2008;63(2):167-74.
12. Armelin E, Meneguzzi A, Ferreira CA, Aleman C. Polyaniline, polypyrrole and poly(3,4-ethylenedioxythiophene) as additives of organic coatings to prevent corrosion. *Surf Coat Tech.* 2009;203(24):3763-9.
13. Anicai L, Florea A, Buda M, Visan T. Polypyrrole Films Doped with Phosphomolybdate Anions on Al Surfaces - Formation and Corrosion Protection Characterisation. *Z Phys Chem.* 2013;227(8):1121-41.
14. Aravindan N, Sangaranarayanan MV. Influence of solvent composition on the anti-corrosion performance of copper-polypyrrole (Cu-PPy) coated 304 stainless steel. *Prog Org Coat.* 2016;95:38-45.
15. Arabzadeh H, Shahidi M, Foroughi MM. Electrodeposited polypyrrole coatings on mild steel: Modeling the EIS data with a new equivalent circuit and the influence of scan rate and cycle number on the corrosion protection. *J Electroanal Chem.* 2017;807:162-73.
16. Balaskas AC, Kartsonakis IA, Kordas G, Cabral AM, Morais PJ. Influence of the doping agent on the corrosion protection properties of polypyrrole grown on aluminium alloy 2024-T3. *Prog Org Coat.* 2011;71(2):181-7.



## EFFECT OF 5-NITRO-2-FURALDEHYDE ON CORROSION OF CARBON STEEL

Abdurrahman Asan\*  

Hittite University, Faculty of Engineering, Corum, 19030, Turkey.

**Abstract:** Evaluation of corrosion inhibitors for carbon steel in chlorinated environments is very important for some industrial plants. For this purpose, the inhibitory effect of 5-nitro-2-furaldehyde on the corrosion of carbon steel in aqueous solutions of 0.1 M NaCl and 0.1 M HCl was investigated. Cyclic voltammograms were taken to determine the electrochemical behavior of carbon steel in non-inhibitory and inhibitory environments. The corrosion rates of carbon steel in the presence of 5-nitro-2-furaldehyde in different concentrations (10, 20, 50 and 100 ppm) were measured by the Tafel Polarization method. As the inhibitor concentration increased, no significant change was detected in the 0.1 M HCl medium. In the 0.1 M NaCl environment, the corrosion potential has shifted to values that are more positive and the corrosion current has been reduced. This indicates that the inhibitors form a film on the surface of metal in this environment and create resistance to corrosion. The best inhibitory activity was achieved with an inhibitor concentration of 100 ppm in 0.1 M NaCl medium.

**Keywords:** Corrosion, Inhibitor, Tafel Polarization, Carbon Steel.

**Submitted:** May 31, 2019. **Accepted:** August 27, 2019.

**Cite this:** Asan A. EFFECT OF 5-NITRO-2-FURALDEHYDE ON CORROSION OF CARBON STEEL. JOTCSB. 2019; 2(2): 137-42.

\*Corresponding author. E-mail: [asanabdurrahman@hotmail.com](mailto:asanabdurrahman@hotmail.com).

### INTRODUCTION

Corrosion of metals and alloys can lead to pollution of the environment and loss of economy (1-3). Carbon steel is a widely used construction material in many industrial areas due to its low cost and excellent mechanical properties (4, 5). Carbon steel is used in exchangers, boilers, reactors, storage tanks, gas and oil transportation industry, etc. However, carbon steel is particularly vulnerable to corrosion in oil and gas production systems (6, 7). Although inhibitors are highly effective in corrosion and oil and gas production systems, the selection and application of inhibitors due to variable corrosive environments is complex (6, 8-10).

However, in the event of corrosion of the steel in corrosive environments; studies to increase the corrosion resistance of the environment by applying inhibitor cataracts, cathodic protection, adding coating element, alloying element or changing corrosive environment. This method does not require change in the system and can be easily controlled (11-14). Corrosion inhibitors are mixtures used to protect metallic materials against corrosion, which can be applied to closed systems and generally prepared in certain formulas. The active ingredients are selected according to the conditions in the mixtures. The formula of the mixture is mostly patented. What is important, however, is the type and concentration of the active substance in the

mixture. The researchers carry out the selection of active substances. Many investigators have found that compounds with have a non-paired electron such as sulfur, nitrogen, and oxygen have a very good inhibitory candidates (15-18).

The inhibitor property of the 5-nitro-2-furaldehyde compound, whose structure was given in Figure 1, is firstly investigated by this study.

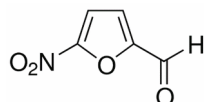


**Figure 1.** Structural formula of 5-nitro-2-furaldehyde.

## EXPERIMENTAL

In the experiments, a 250 mL three-necked corrosion cell was used. Chemical composition

of carbon steel given in Table 2 was placed in the middle neck of the cell as the working electrode. The working electrode is prepared by embedding it in a polyester resin with an open area of 1.0 cm<sup>2</sup>. Before each test, the working electrode surface was polished with 2000-inch sandpaper under water. The electrode was washed with distilled water and placed in the experimental apparatus after treatment with ethyl alcohol. For measurement of the electrode potential, saturated calomel electrode (SCE) was used as the reference electrode. A platinum plate with 1.0 cm<sup>2</sup> surface area was used as the counter electrode for current measurement. In order to allow time for interaction between the working electrode and the inhibitor, working electrode was kept for 30 minutes in inhibitor contained solution before each electrochemical polarization. Tafel Polarization curves and cyclic voltammograms were obtained by using Ivium Technologies De Regent 178 5611 HW Eindhoven Ivium Compact Stat.

**Table 1.** Chemical Composition of Carbon Steel.

C	Mn	P	Si	Cr	Al	Cu	Fe
0.08	0.17	0.01	0.05	0.05	0.04	0.20	Rest

Inhibition Efficiency was calculated according to the following equation.

$$\text{Inhibition Efficiency \%} = \frac{CR(\text{without inhibitor}) - CR(\text{with inhibitor})}{CR(\text{without inhibitor})} \times 100$$

## RESULTS AND DISCUSSION

The CV voltammogram of carbon steel obtained in 0.1 M NaCl medium is given in Figure 2. In anodic polarization with a scanning speed of 100 mV / s in the range of -1.5 V to 0.0 V, the anodic current passes in -1.2 V and ends at very low current at about -0.3 V. Carbon steel is passive until this potential. However, after this potential, the current is rapidly increasing and passivation occurs. The anodic current at 0.0 V is approximately 12 mA.

Tafel polarization method was used to determine the corrosion rate of carbon steel in 0.1 M NaCl medium containing 5-nitro-2-furaldehyde. Tafel Polarization curves were obtained with a scan rate 2 mV/s in the range of -1.5 V to 0.0 V. Tafel Polarization curves obtained in 0.1 M NaCl medium containing 10, 20, 50 and 100 ppm inhibitor and without inhibitor were overlapped and given in Figure 3.

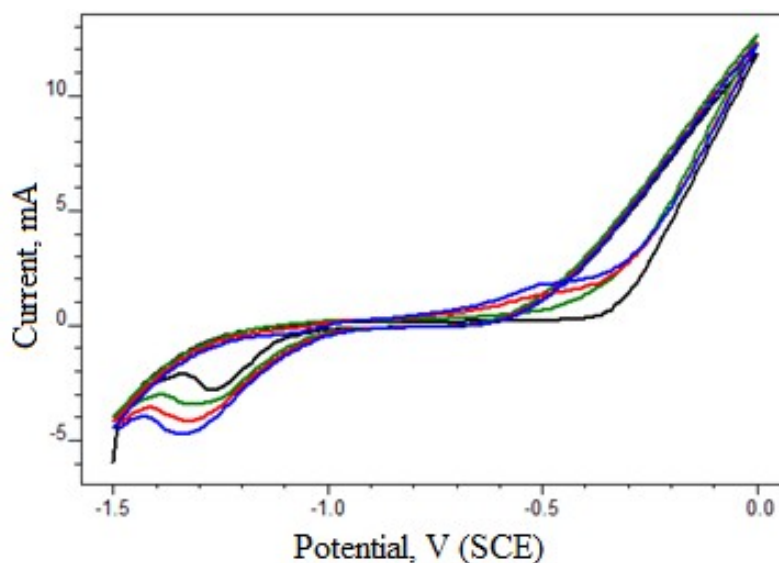


**Figure 2.** Cyclic voltammogram of Carbon Steel in 0.1 M NaCl.

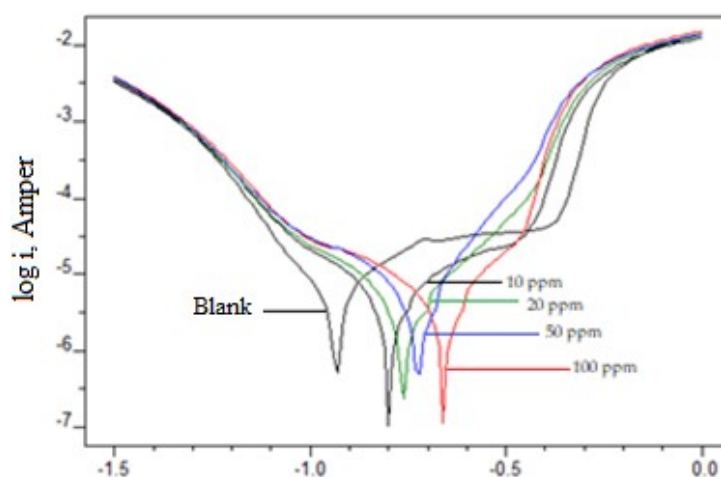


**Figure 3.** Tafel Polarization Curves of carbon steel in 0.1 M NaCl solution with and without inhibitor in different concentrations.

In all inhibitor concentrations, the corrosion potential of the steel was increased while the corrosion potential of the steel increased compared to the medium without inhibitor. As the inhibitor concentration increases, the corrosion potential of the corrosion potential is further reduced. This shows that the inhibitor slows down both the anodic reaction and the cathodic reaction. It was understood that 5-

nitro-2-furaldehyde behaves as a mixed inhibitor for carbon steel in this medium.

The polarization curves of the carbon steel obtained in 0.1 M HCl solution were given in Figure 4. The anodic current occurs at about -0.7 V. There was a large increase in the anodic current after a very small increase of about 100-200 mV. It is understood that there is no passivity on the surface.

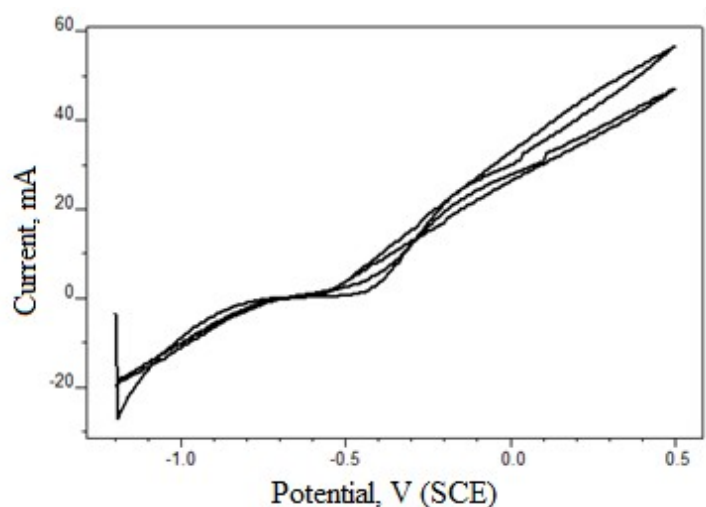


**Figure 4.** Cyclic voltammogram of Carbon Steel in 0.1 M HCl.

Tafel polarization curves obtained in 0.1 M HCl medium without inhibitor and containing inhibitor at different concentrations were overlapped and given in Figure 5. The curves in the hydrochloric acid medium without inhibitor and containing 10, 20, 50 ppm inhibitors are almost coincident. The curve obtained in the solution containing only 100

ppm inhibitor has a small increase in steel potential and a decrease in current.

In both corrosive environments, the corrosion parameters obtained by extrapolation of Tafel Polarization curves and the calculated inhibitor activity results were summarized in Table 2.

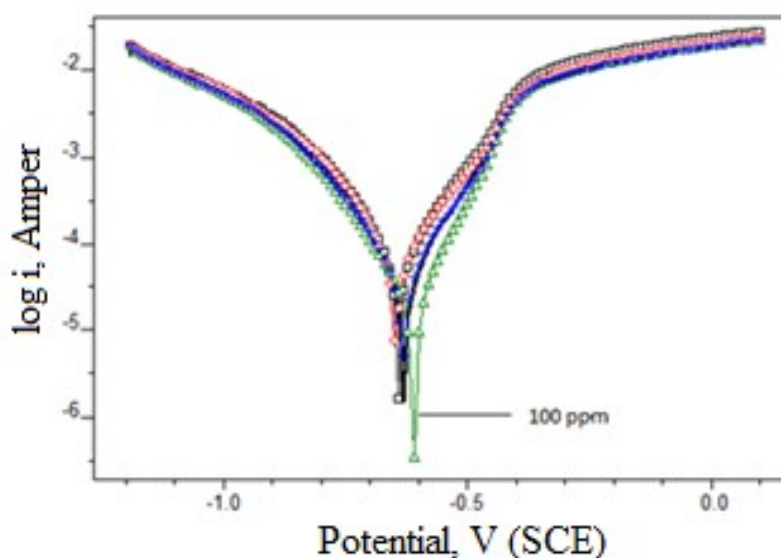


**Figure 5.** Tafel Polarization Curves of carbon steel in 0.1 M HCl solution with and without inhibitor in different concentrations.

**Table 2.** Carbon steel corrosion parameters in corrosive environments.

	Concentration (ppm)	Ecor (mV)	Rp (ohm)	Corrosion Rate (mm/y)	Inhibition Efficiency%
<b>0,1 M NaCl</b>	without	-950	9088	0.071	-
	10	-811	12050	0.032	54.9
	20	-774	12180	0.014	80.3
	50	-742	12750	0.011	84.5
	100	-683	13124	0.010	85.9
<b>0,1 M HCl</b>	without	-665	643	0.5023	-
	10	-661	647	0.5009	0.3
	20	-658	648	0.5010	0.3
	50	-657	651	0.4995	0.5
	100	-619	687	0.4321	7.0

As a result, while 5-nitro-2-furaldehyde did not provide significant inhibition efficiency in acidic medium, which is a corrosive environment, it has provided significant activity in the saline environment. The best inhibition efficiency was found to be 85.9% in 0.1 M NaCl medium containing 100 ppm inhibitor.

#### ACKNOWLEDGMENTS

This article was submitted as an oral presentation to the 13rd National Chemical Engineering Congress.

#### REFERENCES

1. Cost of corrosion in the USA. *Anti-Corros Method M.* 2000;47(3):141-.
2. Calculating the cost of corrosion. *Mater World.* 1999;7(3):130-.
3. De Baere K, Verstraelen H, Rigo P, Van Passel S, Lenaerts S, Potters G. Reducing the cost of ballast tank corrosion: an economic modeling approach. *Mar Struct.* 2013;32:136-52.
4. Agi A, Junin R, Rasol M, Gbadamosi A, Gunaji R. Treated *Rhizophora mucronata* tannin as a corrosion inhibitor in chloride solution. *Plos One.* 2018;13(8).
5. LaBrosse M, Erickson D. The Pursuit of a Green Carbon Steel Corrosion Inhibitor-Part 2. *Mater Performance.* 2014;53(9):48-52.
6. Askari M, Aliofkhaezrai M, Ghaffari S, Hajizadeh A. Film former corrosion inhibitors for oil and gas pipelines - A technical review. *J Nat Gas Sci Eng.* 2018;58:92-114.
7. de Souza ADN, Rossi CGFT, Dantas TND, de Souza MAF, de Lima DF, Menezes FG, et al. Efficiency of the Heterocycle Isatin Loaded in Microemulsions as Corrosion Inhibitor for Mild Steel in Saline Medium. *Quim Nova.* 2017;40(7):760-8.
8. Adewuyi A, Oderinde RA. Synthesis of hydroxylated fatty amide from underutilized seed oil of *Khaya senegalensis*: a potential green inhibitor of corrosion in aluminum. *J Anal Sci Technol.* 2018;9.
9. Mohamed S, Meliani MH, Khaled E, Fares C, Benghalia MA. Corrosion Effects and Green Scale Inhibitors in the Fracture Mechanics Properties of Gas Pipelines. *Struct Integr Life.* 2017;17(1):25-31.
10. Olajire AA. Corrosion inhibition of offshore oil and gas production facilities using organic compound inhibitors - A review. *J Mol Liq.* 2017;248:775-808.
11. Abdallah M, Altass HM, AL Jahdaly BA, Salem MM. Some natural aqueous extracts of plants as green inhibitor for carbon steel corrosion in 0.5 M sulfuric acid. *Green Chem Lett Rev.* 2018;11(3):189-96.
12. Abdallah M, Hegazy MA, Alfakeer M, Ahmed H. Adsorption and inhibition performance of the novel cationic Gemini surfactant as a safe corrosion inhibitor for carbon steel in hydrochloric acid. *Green Chem Lett Rev.* 2018;11(4):457-68.

13. Afia L, Benali O, Salghi R, Ebenso EE, Jodeh S, Zougagh M, et al. Steel Corrosion Inhibition by Acid Garlic Essential Oil as a Green Corrosion Inhibitor and Sorption Behavior. *Int J Electrochem Sc.* 2014;9(12):8392-406.
14. Abiola OK, Otaigbe JOE, Kio OJ. *Gossipium hirsutum* L. extracts as green corrosion inhibitor for aluminum in NaOH solution. *Corros Sci.* 2009;51(8):1879-81.
15. Asan A, Kabasakaloglu M, Işıklan M, Kılıç Z. Corrosion inhibition of brass in presence of terdentate ligands in chloride solution. *Corros Sci.* 2005;47(6):1534-44.
16. Branzoi F, Branzoi V. Investigation of Some Nonionic Surfactants as Corrosion Inhibitors for Carbon Steel in Sulfuric Acid Medium. *Int J Electrochem Sc.* 2017;12(8):7638-58.
17. Harvey TJ, Walsh FC, Nahle AH. A review of inhibitors for the corrosion of transition metals in aqueous acids. *J Mol Liq.* 2018;266:160-75.
18. Alvarez PE, Fiori-Bimbi MV, Neske A, Brandan SA, Gervasi CA. *Rollinia occidentalis* extract as green corrosion inhibitor for carbon steel in HCl solution. *J Ind Eng Chem.* 2018;58:92-9.